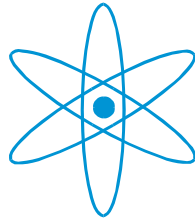# PHYSIK–DEPARTMENT

Entanglement of Higher Dimensional Quantum States

Diploma Thesis
of
Daniel Lampert Richart

Work performed under the guidance of
Prof. Dr. Harald Weinfurter and
Prof. Dr. J. Ignacio Cirac

München, January 2008

TECHNISCHE UNIVERSITÄT
MÜNCHEN

Contents

Chapter 1

Introduction

Since its development driven by Bohr, Heisenberg, Pauli, Schrödinger et al. in the beginning of the 20th century, Quantum Mechanics has suggested a sometimes strange and weird picture about the microcosm not directly accessible to everyday experience: Photons which can have taken both paths of an interferometer at the same time or atomic ensembles acting together as a "superparticle" at very low temperatures are examples, which explained in common language, are completely non-intelligible. Even Schrödinger hinted at the apparent absurdity of an application of the interpretations of the theory to the macroscopic world [1]:

If a cat's state of life or death could be made dependent on the state of a subatomic particle and made inaccessible to the observer, it could exist in the joint superposition of being alive or dead. Surely this is an interpretation which hardly enjoys any correspondence to reality.

Similarly, the predicted possibility that two "entangled" particles remain perfectly correlated over arbitrarily large distances moved Einstein to describe this effect as a "spooky action at a distance". Well evidenced by the extensive correspondence between him and Bohr, one of the mayor proponents of the Copenhagen interpretation of Quantum Mechanics, Einstein repeatedly aimed to prove that its framework couldn't provide a complete description of natural phenomena.

Despite of the fact that these discussions took clear philosophical connotations in their beginnings, they also motivated many of the most important discoveries in physics:

The resource of entanglement proved to be suited for performing tasks which were impossible according to classical mechanics. Indeed, entanglement provided the fundamental key component for the development of quantum information theory, a synthesis between the fields of quantum theory, information theory, informatics and cryptography. Using this framework, the application of entanglement for the manipulation and transmission of information as required by today's information technologies has proven to offer its highest potential.

The transmission of completely secure information over telecommunication distances [2] as well as the teleportation of the quantum state of atoms from one locality to another [3], are only two out of the broad range of achievements which could be realized based on entangled particles. Motivated by advances in the trapping and control of ionic ensembles or other types of qubits, the possibility to carry out computational operations on entangled systems would allow the realization of computers capable of performing several operations at the same time, therefore being much more efficient than a classical computer.

Nevertheless, a full characterization and study of entangled states at a more fundamental level is required before these technologies can be tamed for accessing their full potential.

For example, the wide range of multiple-photon entangled states [4] well suited for implementing multi-party quantum communication protocols has yet not been investigated in its full potential.

In analogue, the possibility of quantum systems to be prepared in a higher dimensional Hilbert space offers interesting improvements with respect to the implementation of quantum key distribution (QKD) protocols. In general, these higher dimensional states can transmit more information, using for example higher alphabets, than two dimensional systems and reduce the noise threshold limiting the security of these protocols [5, 6]. Similarly, it was hinted at the possibility that for these states an increase in the efficiency of Bell state measurements required for quantum teleportation can be achieved [7].

Following these research lines, the study and experimental realization of higher dimensional entanglement will be the main focus of this work.

1.1   Why energy-time and time-bin entanglement?

Long distance implementation   Since the entangled nature of polarization correlated photons could clearly be displayed, a wide range of research focused on the implementation of entangled photons was motivated. Taking advantage of the entangled nature of polarization entangled photons, classically impossible tasks, such as the teleportation of a quantum state [8], or the implementation of quantum communication protocols [9, 10] were possible. First steps could be realized as well with respect to the realization of quantum computation operations [11].

The intrinsically secure transmission of information, as permitted by quantum cryptography, has motivated the interest to investigate the distribution of entangled photons over long distances, as required for telecommunication transmission. Polarization entangled photons could successfully be distributed over free space distances up to 144km

[12], displaying the feasibility of establishing a quantum communication network over satellites, as discussed in [13].

In future scenarios, the distribution of polarization entangled photons over ground based telecommunication channels such as fibres offers a high advantage with respect to a free space channel subject to atmospheric fluctuations. Due to absorption and the low efficiency of detectors suited for telecommunication wavelengths these distances would be limited to a range of 100km [12]. Nevertheless, polarization entangled photons offer the disadvantage that the quality of the entangled state encoded would be affected by polarization mode dispersion: This refers to the temporal delay between two pulses caused by the random change in the polarization state encoded due to the birefringent nature of optical fibres.

At this point, the encoding of the entangled states in the energy-time basis offers significant advantages, as the correlation between the photons isn't reduced by a change in the polarization of the photons. As will be shown in section (2.3), only the arrival time information of the correlated photons is relevant for the encoding of an energy-time or time-bin entangled state.

On the other side, chromatic dispersion dependent upon the bandwidth of the entangled photons limits the maximum implementable length of the fibres before the photon wave packets begin to overlap with each other. Nevertheless, the application of a dispersion cancellation scheme intrinsic to the energy-time entangled nature of these photons (See section (2.6)) yields that the maximum achievable transmission distance in dependency of the bandwidth of the photons is superior for energy-time entangled photons [14].

Indeed, the robustness of energy-time and time-bin entangled states with respect to decoherence over large distances could be shown in several experiments:

The distribution of time-bin entangled photons could be achieved for distances of up to 50km of standard optical fibres [15] while energy-time entangled photons could be transmitted over physical distances of more than 10km [16]. Using the same energy-time entanglement configuration, the implementation of QKD protocols could be shown [2, 17] over distances of up to 8,2km. Similarly, a scheme of probabilistic quantum teleportation of time-bin entangled qubits over 2km of optical fibres could successfully be implemented as well [18, 19].

Higher dimensional entanglement   Specific to polarization entangled states is that the Hilbert space of these states is intrinsically 2 dimensional, as only 2 linearly independent polarization vectors span the Hilbert space of the particle's state.

In contrast, photons can be prepared in energy-time and time-bin entangled systems by making use of interferometers, setting the respective arrival time delays between correlated photon pairs. The dimension of the entangled states is therefore directly dependent upon the transformation introduced by the interferometers and not by an

intrinsic property of a particle such as its polarization.

Therefore, interesting fundamental questions about entangled states, such as their behaviour when being encoded in a higher dimensional Hilbert space ($d \geq 2$), can be exploited with energy-time and time-bin entangled photons.

The emergence of classical properties in the limit of high quantum numbers, as expected due to the complementarity principle, is one of the questions still left open to experimental scrutiny [20]. According to the complementarity principle, coined by Bohr, this property of quantum systems can be attributed to the impossibility to establish clear boundaries between the behaviour of the microscopic systems observed and the measurement devices setting the context under which the properties of these systems will be measured.

Experimental realizations of qutrits, i.e. entangled photons in a three dimensional Hilbert space could be performed [21], showing the violation of a corresponding Bell inequality.

An experimental attempt to create higher dimensional entangled states, was reported in [22] by using mode-locked fs-lasers. The approach was to effectively repeat a 2 dimensional time bin entanglement by SPDC photon pairs emitted by up to 20 different pulses still coherent to each other. A similar approach exists for a Fabry-Perot like interferometer [23]. Nevertheless, for these experiments the analysis of the states was achieved by letting the correlated photons, being created by different pulses, traverse exactly the same one-arm interferometers. Therefore, neither of these two experiments was capable of providing a full analysis of the entangled states, as can be provided by the analysis with a multi-arm interferometer.

1.2   Aim of this work

This work is focused to be the first experimental step to attain the encoding and full analysis of correlated photon pairs in higher dimensional entangled states. With this respect, the scalability of the system used such as to be suited for the preparation of correlated photons in a higher dimensional state will be one of the main purposes.

This work will be subdivided into two main chapters:

The first one will discuss the theoretical framework behind entanglement (section (2.1)) and the source of correlated photons, the spontaneous parametric down-conversion process (SPDC) (section (2.2)), following a detailed description of their preparation and analysis in two dimensional energy-time (section (2.3)) and time-bin (section (2.4)) entangled states. Hinting at future experimental implementations, time bin entangled states in a general higher dimensional Hilbert space will be discussed in the same framework (section (2.4.2)). In order to be able to give experimental evidence of the

entangled nature of the photons, a CHSH inequality suited for energy-time and time-bin entangled photons in the two dimensional Hilbert space is given (section (2.5)). The detrimental effect of dispersion at optical fibres on energy-time entangled states will be discussed in section (section (2.6)).

The second chapter will be focused on the full characterization of the experimental system used to prepare the photons in two dimensional energy-time entangled states, especially with regard to its suitability for preparing and analyzing higher dimensional entangled states (section (3.1)). Finally, the experimental results for two dimensional energy-time entanglement will be presented, displaying the violation of the CHSH inequality (section (4.1)). First experimental efforts for a time-bin entanglement experiment will be discussed as well (section (4.2)).

Chapter 2

Theoretical Background

This chapter covers the theoretical description of energy-time and time-bin entanglement in two dimensions and additionally of time-bin entanglement in a higher dimensional Hilbert space. First, the basic theory behind entanglement will be presented, following a short description of the spontaneous parametric down-conversion (SPDC) photon source, which can be prepared in these entangled states. The entanglement of the prepared state can be tested by applying Bell inequalities for energy-time and time-bin entangled states. From these the experimental parameters required to characterize the entanglement can be extracted. Finally, detrimental effects on the entanglement of the state such as dispersion in optical fibres will be discussed in detail.

2.1 Entanglement and Bell inequalities

2.1.1 Quantum Mechanics and Entanglement

The mathematical framework of Quantum Mechanics allows to give a consistent derivation and description of physical systems. This description evolves based on a set of underlying postulates [24]:

Postulate 1: State Space

> The state space of an isolated physical system is represented by a Hilbert space H. The full information of the system is contained in the pure state $|\Psi\rangle \in H$ with $\langle\Psi|\Psi\rangle = 1$.

Based on this postulate, quantum mechanics predicts that a complete description of a system can be assigned to the state $|\Psi\rangle$ by performing measurements with respect to one of the basis $|k\rangle$. The state can be linearly expanded as $|\Psi\rangle = \sum_k c_k|k\rangle$ with c_k

being the respective eigenvalues of the eigenstates $|k\rangle$.

Nevertheless, a suitable description of a physical system can only be warranted as long as one accounts for the time evolution of the state describing it.

Postulate 2: Temporal Evolution

> The time evolution of a closed system is described by a state $|\Psi\rangle$ holding to the Schrödinger equation
>
> $$i\hbar\frac{d}{dt}|\Psi\rangle = H|\Psi\rangle \tag{2.1}$$
>
> with $\hbar$ being the experimental Planck constant and H being the Hamilton-operator of the system.

Postulate 2 implies that an operator defining the energy of the state $|\Psi\rangle \in H$ and its time evolution is the Hamilton operator $H : H \to H$. Its eigenvalues correspond to the discrete energy levels E_k of the physical system. More importantly, due to the linearity of a general operator transformation $O : H \to H$, postulate 2 implicitly states the **Superposition Principle**:

> Each linear combination $|\Psi\rangle = \sum_l r_l |\Psi\rangle_l$ of physical states $|\Psi\rangle_l$ holding to the Schrödinger equation is a physical state of the system.

Postulate 3: Measurement

> The measurement of a physical observable on a state $|\Psi\rangle$ is described as a family of measurement operators M_k on the state space H holding to the completeness relation $\sum_k M_k^\dagger M_k = I$. The average probability for a measurement result k is defined as
>
> $$p(k) = \langle\Psi|M_k^\dagger M_k|\Psi\rangle. \tag{2.2}$$
>
> After the measurement the state of the system is reduced to
>
> $$|\Psi\rangle_k = \frac{M_k|\Psi\rangle}{\sqrt{\langle\Psi|M_k^\dagger M_k|\Psi\rangle}} = \frac{M_k|\Psi\rangle}{\sqrt{p(k)}} \tag{2.3}$$

Postulate 3 states that classically interpretable measurement results k with respect to a specific measurement basis $|k\rangle$ and with a probability distribution $p(k)$ can be extracted.

Implicit to Eq.(2.3) is the collapse of the wave function, stating that the measurement $\{M_k\}$ with measurement result k projects the state into $|\Psi\rangle_k$. This statement is based upon the assumption that the interaction with the experimental apparatus intrinsically disturbs the measured state, such that the measured observables underlie an intrinsic random distribution.

Applied on the state space $H = H_A \otimes H_B$ of two closed physical systems H_A and H_B, postulates 1, 2 and 3 of Quantum Mechanics allow special properties for the state $|\Psi\rangle$ describing the system, which cannot be understood in terms of classical physics:

Entanglement

A state $|\Psi\rangle$ on the Hilbert space $H = H_A \otimes H_B$ is called *separable* when: $\exists |\Psi\rangle_A \in H_A$ and $|\Psi\rangle_B \in H_B$ such that $|\Psi\rangle = |\Psi\rangle_A \otimes |\Psi\rangle_B$. Otherwise the state is called *entangled*.

Only quantum mechanics allows the existence of entangled states, as the superposition principle, implicitly stated by proposition 2, enables the superposition of two indistinguishable, i.e. orthogonal, states $|i\rangle_A |i\rangle_B$ and $|j\rangle_A |j\rangle_B$ with $\{|i\rangle_A, |j\rangle_A\} \in H_A$ and $\{|i\rangle_B, |j\rangle_B\} \in H_B$ to the entangled state $|\Psi\rangle = \alpha |i\rangle_A |i\rangle_B + \beta |j\rangle_A |j\rangle_B$ with $(i,j) = \{0,1\}$. A maximally entangled state is for example $|\Phi^+\rangle = \frac{1}{\sqrt{2}}(|0\rangle_A |0\rangle_B + |1\rangle_A |1\rangle_B)$.

Under the assumption stated by Postulate 1, $|\Psi\rangle$ provides a complete picture of the physical system.

Nevertheless, entangled states offer characteristics which preclude a consistent description when the physical system measured is described according to a local realistic model.

2.1.2 EPR argument and Bell inequality

In the year 1935, Einstein, Podolski and Rosen formulated a Gedankenexperiment hinting at the inconsistencies of Quantum Theory with the principles of reality [25]:

Aiming to restore "elements of reality" into the theory of quanta, they defined the requirement a complete theory would have to fulfil: Once it is able to determine the measurement outcomes on a system with absolute certainty, the existence of an element of reality corresponding to the measured physical variable has to be inferred.

Based on this requirement, the argument they inferred against Quantum Mechanics can be resumed as follows: As stated in postulate 3, Quantum Mechanics is based on the intrinsic assumption that prior to the measurement the state of the system is undefined. With respect to an entangled state $|\Psi\rangle$, such as for example $|\Psi\rangle = \frac{1}{\sqrt{2}}(|0\rangle_A |0\rangle_B + |1\rangle_A |1\rangle_B)$ with $\{|i\rangle_A\} \in H_A$ and $\{|i\rangle_B\} \in H_B$ with $i = 0, 1$, this means that the measurement on one of the two-state systems H_A instantly determines the

measurement outcome on the system H_B with absolute certainty. Prior to the measurement, no statement can be done about the systems H_A and H_B.

The paradox arises when both systems H_A and H_B have been distributed to two spatially distributed measurement devices:

Assuming that causality should be a basic principle of the theory, the measurement on one system H_A cannot instantly influence the measurement outcome at the other system. Nevertheless, due to the entangled nature of both distributed systems the measurement $\{M_A\}$ on the system H_A instantly reduces the state wavefunction to $|1\rangle_A |1\rangle_B$ or $|0\rangle_A |0\rangle_B$ from which the outcome of a possible measurement $\{M_B\}$ on H_B can be determined.

This fact would certainly be in contradiction to Proposition 3, as this would require that the state of the system H_B is already defined prior to its measurement.

According to the requirement given in the EPR paper[25] for a complete theory, quantum mechanics cannot be considered as complete, as long as it is assumed that the outcomes of the measurements performed on the systems H_A and H_B don't correspond to an "element of physical reality".

The merit for solving this apparent paradox without resorting to philosophical arguments can be attributed to Bell [26], 29 years later.

The main purpose of this paper is to derive experimentally accessible constraints which a theory based on the precepts of reality and locality [1] would have to offer when the correlation between measurement results on both systems H_A and H_B sharing the entangled state $|\Psi\rangle$ is analyzed. The expected constraint on the statistical distribution of the measurement results for such a theory clearly differs from the one for an entangled system.

The inconsistency of quantum mechanics with a local and realistic theory describing nature would have to be concluded.

The experimental proposal of Bell [26], limited to correlation measurements of Spin-1/2 particles, could be extended in 1969 [27] by Clauser, Horne, Shimony and Holt such as to be implementable on experimentally more accessible entangled systems. First experiments by Freedman and Clauser [28] were done in 1972, but a direct test of the CHSH Bell inequalities was provided by Aspect et al. in 1982 [29]. These experiments, based on polarization correlated photons, enabled to provide a decisive test that the observed correlations between both photons weren't reproducible by a local realistic theory.

A CHSH inequality applied on energy-time and time-bin entangled states (See section (2.3) and (2.4)) as studied in this work will be derived in greater detail in section (2.5).

---

[1]Such a theory is often referred to as "Local Hidden Variable Theory", with the hidden variables determining the measurement outcomes on the system prior to their measurement

2.2 Source of the entangled photons

This section is focused onto a description of the theoretical background behind the Spontaneous Parametric Down Conversion process. As will be shown later, this source offers ideal characteristics to prepare energy-time or time-bin entangled states. For Type II down-conversion the transversal and longitudinal walk-off between the generated photon pairs has to be discussed, too.

2.2.1 Type II collinear SPDC

The process of spontaneous parametric down-conversion has been proven to be one of the most efficient methods to generate photon pairs. Although being a process which could only be understood in terms of quantum mechanics it has a phenomenological analogy in classical electrodynamics.

When a strong pump wave $\vec{E}_p$ traverses a dielectric crystal, the medium gets macroscopically polarized. For an anisotropic medium, the macroscopic polarization, given by the sum of the induced electrical dipole moments, reads as

$$P^i = \epsilon_0 \left(\sum_j \chi_{ij}^{(1)} E^j + \sum_{jk} \chi_{ijk}^{(2)} E^j E^k + \sum_{jkl} \chi_{ijkl}^{(3)} E^j E^k E^l + ... \right). \qquad (2.4)$$

The first term with the susceptibility tensor of first order, $\chi^{(1)}$, describes the refraction or dispersion characteristics of the pump wave in the crystal's medium, while the creation of SPDC photon pairs can be attributed to the nonlinear coupling term, with $\chi^{(2)}$. $\chi^{(2)}$ and $\chi^{(3)}$ denote the susceptibility tensor of second order and third order respectively.

An illustrative description of this term can be given, when one considers a strong and a weak wave with frequencies ω_p and ω_s traversing the crystal medium. The weak wave can be amplified under the emission of a correlated "idler" photon with the difference frequency $\omega_i = \omega_p - \omega_s$, as conditioned by the conservation of energy, such that $\omega_p > \omega_s, \omega_i$ holds. This nonlinear process is described as the coupling between the pump wave E^p, with frequency ω_p and wave vector $\vec{k}_p$ and two spontaneous light waves E^j and E^k with frequency ω_i and ω_s and wave vectors $\vec{k}_s$ and $\vec{k}_i$ respectively. For the implemented BBO crystals the strength of this nonlinear interaction is in the range of $\chi^{(2)} \approx 10^{-10}$, i.e. ten orders of magnitude smaller than for the linear term $\chi^{(1)} \approx 1$ but still 7 orders of magnitude larger than the coupling term of next order $\chi^{(3)} \approx 10^{-17}$ [30]. Despite of these seemingly low nonlinear coupling efficiencies the initially weak waves E^j and E^k can become strongly amplified if the pump wave offers high intensities. Nevertheless, these pump intensities are low enough in this experiment such that the coupling of higher order between more than three waves can be neglected. However, the classical framework fails to provide a full description of the SPDC pro-

cess. Due to the fact that the process is of spontaneous nature, i.e. it happens without
the coupling to any additional weak field, a consistent description can only be given in
terms of a quantum mechanical framework [31].

The condition $\chi^{(2)} << \chi^{(1)}$ enables to apply perturbation theory on the nonlinear cou-
pling term between the pump and SPDC waves in order to derive the Hamiltonian of
the SPDC biphoton state [30, 32]:

$$H_{Int}(t) = 1/2 \int_V d^3x \vec{P}_{NL}\vec{E}^P = \epsilon_0/2 \int_V d^3x[\chi^{(2)}_{ijk}E_j^-(\vec{x},t)E_k^-(\vec{x},t)E_i^+(\vec{x},t) + h.c.] \quad (2.5)$$

with $E_m^- = -i\sqrt{\frac{\hbar\omega_m}{2\epsilon_0 n_j V_q}} \int d^3k_m A(\vec{k}_j)a_{\vec{k}_m}^\dagger e^{-i(\vec{k}_m\vec{x}-\omega_j t)}\hat{e}_m$ being the signal $(m = s)$ and
idler $(m = i)$ waves as described in the framework of second quantization. Here V_q
denotes the quantization volume and $A(\vec{k}_j)$ is the distribution function of the SPDC
photon modes. In contrast, as the pump field offers high intensities [31], the pump
wave can be described as a classical monochromatic plane wave $E_p^+ = f(\vec{r}_\perp)e^{i(\vec{k}_p x-\omega_p t)}$,
with the transversal amplitude distribution $f(\vec{r}_\perp)$.

The SPDC biphoton state reads as

$$|\Psi_{SPDC}\rangle = e^{-i/\hbar \int_{-\infty}^{\infty} dt H_{int}(t)}|0\rangle \approx \frac{-i}{\hbar} \int_0^{t_{c,P}} dt H_{int}(t)|0\rangle, \quad (2.6)$$

where $|0\rangle$ denotes the vacuum mode. The multimode SPDC photon pairs are coherently
emitted at different emission times as long as the interaction time of the pump wave
with the crystal is shorter than the coherence time of the pump photons. Therefore
the upper and lower integration limit can effectively be substituted by the coherence
time $t_{c,P}$ of the pump photons and 0 respectively.

However, as the detailed calculations are beyond the scope of this work, the reader will
be referred to [30].

Within the same framework of second quantization, the SPDC process can be described
as the decay of a pump photon mode $\hat{a}_{\vec{k}_p}^+$ into a signal and idler photon mode $\hat{a}_{\vec{k}_s}^+$ and
$\hat{a}_{\vec{k}_i}^+$ such that the two photons are emitted simultaneously and such that energy and
momentum conservation holds:

$$\omega_p = \omega_s + \omega_i \quad (2.7)$$

$$\vec{k}_p = \vec{k}_s + \vec{k}_i \quad (2.8)$$

with the condition that $\omega_s, \omega_i < \omega_p$. The conditions (2.7) and (2.8.) are usually referred
to as phase matching conditions. Due to the relatively high mass of the crystal atoms
the momentum and energy the photons transfer on them is negligible, yielding that the
process can be considered as elastic.

It suffices here to point out that an uncertainty $\Delta p_{s,i}$ in the longitudinal and transversal

momentum of the SPDC photons correlated by the phase matching conditions has to be considered. A reason for this is that the phase matching between the pump photon and the corresponding SPDC photons will only be perfect for infinite crystal lengths and ideally planar pump waves. The consequence is that for each down-converted pump photon with vector $\vec{k}_p$ the emission of signal and idler waves with different wave vectors $\vec{k}_s$ and $\vec{k}_i$ satisfying the phase matching conditions are possible. Effectively, for type II down-conversion the bandwidth of the emitted SPDC pairs is increased yielding typical values of $\Delta\lambda_{SPDC} \approx 40nm$, while their coherence length decreases accordingly to $l_c \approx \lambda^2/\Delta\lambda_{SPDC} \approx 30\mu m$ at a wavelength $\lambda = 805nm$.

Due to the optical anisotropy of the BBO crystal, birefringence has to be considered for photons propagating in the crystal medium. Therefore the polarization of the pump and the two SPDC photons with respect to the orientation of the optical axis of the crystal has to be accounted for in the description: The emission direction of an ordinarily and extraordinarily polarized photon will be specified by the angle spanned between the pump photon vector and the optical axis of the crystal. One specifies two types of SPDC processes in relation to the polarization of the involved photons:

- If the pump photon is extraordinarily polarized and the two down converted photons ordinarily, one calls this a Type I down-conversion process.

- If the pump photon is extraordinarily polarized, but one photon ordinarily and the other one extraordinarily polarized then it is a Type II down-conversion process.

Only Type II collinear down-conversion was considered in this work, as it offered a trivial way to deterministically separate the photon pair by their polarization and to work with each photon separately.

To explain the term "collinear" for the considered SPDC process it is necessary to study the conditions (2.7) and (2.8) in more detail:

As the wave vectors $\vec{k}_s$ and $\vec{k}_i$ of the SPDC photons are perfectly correlated, the emission directions of degenerate SPDC signal and idler photons are symmetrically oriented with respect to the propagation direction $\vec{k}_p$ of the pump photon. A well known fact is that for the same wavelength the SPDC photon emission vectors are distributed along cones.

As for a type II SPDC process the down-converted photons are ordinarily and extraordinarily polarized, the optical density of the BBO crystal medium will be different for the two photons and dependent upon the angle spanned between their respective propagation direction and the optical axis of the crystal.

On the other side, this characteristic ensures that by tilting the optical axis of the crystal in relation to $\vec{k}_p$ the emission cones of two momentum correlated down conversion photons can be made to intersect. In this case the term collinear refers to the case when the cones intersect only at one point, such that the emission directions of the

momentum correlated, orthogonally polarized photons are indistinguishable at exactly this point.
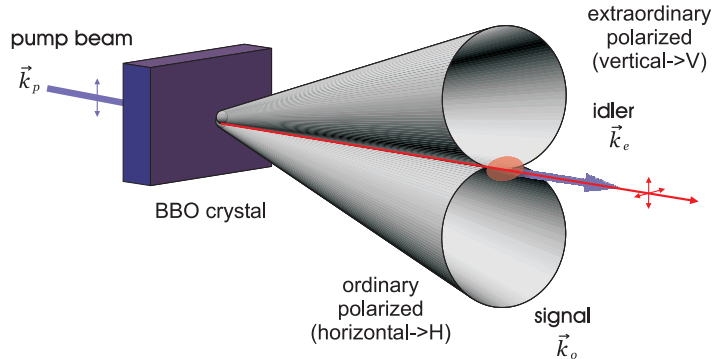
Figure 2.1: *Schematic depiction of the emission cones of the signal and idler photons for a collinear type II down-conversion process. For a vertically polarized photon with respect to the optical axis of the crystal, the signal and idler photons will be horizontally and vertically polarized. The optical axis of the crystal is tilted with respect to the direction $\vec{k}_p$ of the pump photon, such that both emission cones of the SPDC photons intersect at exactly one point.*

At this point one can hint at the possibility of using photon pairs created in the SPDC process as a source for entangled photons. One way to prepare them in an entangled state is to make use of their perfect momentum-position correlation. The detection of the signal SPDC photon emitted at one point of its emission cone will yield that the correlated idler photon will be emitted at exactly the opposed emission direction. An experimental proposal exists in [33].

For the non-collinear Type II SPDC process, analyzing the state of the SPDC photons in the polarization basis yields also perfect correlations, as has already been successfully demonstrated [34]. The photons detected at the overlap regions of the two SPDC emission cones can be made indistinguishable with respect to their polarization and are then prepared in the entangled state

$$|\Psi\rangle = \frac{1}{\sqrt{2}}(|H\rangle|V\rangle + e^{i\phi}|V\rangle|H\rangle) \tag{2.9}$$

However, as the aim of the project is to achieve higher dimensional entanglement, neither entanglement in the polarization nor in the momentum basis is perfectly suited:

A theoretical proposal to prepare impulse-position correlated photons in a higher dimensional Hilbert space exists, consisting in filtering out the spatial modes of correlated SPDC photon pairs along several positions at their emission cones [33]. However, the experimental implementation of such a proposal is difficult.

Instead, following the theoretical proposal of Franson [35], the possibility to entangle the photons in the energy-time basis promises to offer a straightforward way in order to achieve higher dimensional entanglement between both SPDC photons. However

the details about how to prepare the photons in an energy-time entangled state will be presented in the next section (2.4).

2.2.1.1 Compensation of the transversal and longitudinal walk-off

A problem to deal with when handling type II SPDC photons is the transverse and longitudinal walk-off between the ordinarily and extraordinarily polarized photons in the medium of the down-conversion crystal. Both effects are detrimental for achieving a perfect indistinguishability of the SPDC photons, as firstly the transverse walk-off induces a reduced mode overlap, and secondly the longitudinal walk-off reduces the time-indistinguishability between the ordinarily and extraordinarily polarized photons.

- Transverse Walk-Off

  In order to create Type II down-conversion photons, the pump photon has to be extraordinarily polarized with respect to the optical axis of the crystal. The propagation direction of the pump photon energy flux, described by the Pointing vector $\vec{S}_p = \vec{E}_p \otimes \vec{H}_p$ is therefore shifted with respect to the energy flux $\vec{S}_o$ of the ordinarily polarized down conversion photon but is equal to $\vec{S}_e$ for the extraordinarily polarized photon. Therefore, all ordinarily polarized photons spontaneously emitted in the way of the pump photons through the crystal will add up to an elliptic mode, with a shifted center with respect to the mode of the extraordinarily polarized photons, as these are emitted on the direction of the pump photons. This shift can reach values in the range of several tens of μm per mm of crystal length and reduce the overlap between both photon modes. The resulting increase in the spatial distinguishability between both modes leads to a decrease in the entanglement quality to be expected. A way to compensate for this shift exists:

  It consists in rotating the polarization of both SPDC photons by 90° with a $\lambda/2$ waveplate and letting the two shifted modes propagate through a second BBO crystal with half the thickness and the same orientation of the optical axis. Due to the same effect as described above an opposite transversal shift half so large in magnitude of the now extraordinarily polarized photon will ensure that both modes will be centred again spatially (See [30] for more details).

- Longitudinal Walk-Off

  Another disturbing effect based on the birefringence of the crystal is the time delay Δt between the ordinarily and extraordinarily polarized photons after their propagation through the BBO crystal. As photon pairs emitted at different positions of the BBO crystal are coherent with respect to each other, it will suffice to consider SPDC photon pairs produced at symmetrically opposed sides $L - \epsilon$

and ϵ of the crystal with length L. The time delays $\Delta t_\epsilon = \Delta t_{H,\epsilon} - \Delta t_{V,\epsilon}$ and $\Delta t_{L-\epsilon} = \Delta t_{H,L-\epsilon} - \Delta t_{V,L-\epsilon}$ between an ordinarily (H) and extraordinarily (V) polarized photon created at different points ϵ and $L - \epsilon$ of the crystal depends upon the path $L - \epsilon$ and ϵ both photons have traversed in the BBO crystal.

The time delay between the photons of the first photon pair can be characterized as $\Delta t_{L-\epsilon} = (L - \epsilon) \cdot \frac{\Delta n}{c}$ and for the photons of the second as $\Delta t_\epsilon = \epsilon \cdot \frac{\Delta n}{c}$ with Δn denoting the difference in the refraction index of both H and V polarized photons. The magnitude of these time delays can reach values higher than the coherence time of the SPDC photons $t_c \approx 100 fs^2$, such that the indistinguishability between the two-photon states $|H\rangle_{L-\epsilon}|V\rangle_{L-\epsilon}$ and $|V\rangle_\epsilon|H\rangle_\epsilon$ created at different points $L - \epsilon$ and ϵ of the crystal is reduced.

The solution for this problem is given by the same configuration as for compensating the transversal walk-off, with a $\lambda/2$ waveplate and an additional BBO crystal with half the width and the same orientation of the optical axis as for the first crystal.

Due to the $\lambda/2$ waveplate the photons acquire the opposite polarization before traversing the second BBO crystal. Once they propagate in this BBO crystal, the time delay between each photon in the states $|H\rangle|V\rangle_{L-\epsilon}$ and $|V\rangle|H\rangle_\epsilon$ will now be opposite and half so large in magnitude than in the first crystal:

$$\Delta t_2 = -L/2 \cdot \frac{\Delta n}{c}. \tag{2.10}$$

This yields a total time delay of

$$\Delta t_{tot,L-\epsilon} = \Delta t_{L-\epsilon} - \Delta t_2 = \Delta t_{(L/2-\epsilon)} \cdot \frac{\Delta n}{c}$$

$$\Delta t_{tot,\epsilon} = \Delta t_\epsilon - \Delta t_2 = (-L/2 + \epsilon) \cdot \frac{\Delta n}{c} = -\Delta t_{tot,\epsilon} \tag{2.11}$$

for both two-photon states.

This warrants that after the second BBO crystal the time delays between the photons in the states $|H\rangle|V\rangle_{L-\epsilon}$ and $|V\rangle|H\rangle_\epsilon$ created at different points $L-\epsilon$ and ϵ of the BBO crystal are opposite in sign but have exactly the same magnitude for each considered pair of creation points. This holds too for each emission point configuration with general $\epsilon \leq L/2$, such that the two-photon states emitted at different points of the crystal remain indistinguishable with respect to their detection time.

---

[2]SPDC photons filtered out by 5nm filters

2.3 Energy-time entanglement

Based on the theoretical proposal by J.D. Franson [35] to prepare a quantum state in an energy-time entangled state, this section will present the necessary theoretical background.

### 2.3.1 Two dimensional energy-time entanglement

In his original proposal for an experiment on energy time entangled photons, Franson originally devised photon pairs created in an atomic decay process. Considered were three level atoms such that a photon with emission time uncertainty τ_1 is emitted from the excited state Ψ_e into the intermediate state Ψ_i and a photon with emission time uncertainty τ_2 is emitted from the intermediate state Ψ_i to the ground state Ψ_g. A feasible condition for general atomic systems is that the atomic lifetimes fulfil the condition $\tau_2 << \tau_1$, i.e. the uncertainty in the coincidence time between both photons is much smaller than their shared emission time uncertainty.

Once a coincidence time measurement between both photons is carried out, the detection of one of the photons would therefore instantly determine the time of creation of the other photon up to an accuracy τ_2 much smaller than the shared indeterminacy in their emission time τ_1, independently how far away the detectors would be placed: In terms of a quantum theoretical approach, the instant reduction of the photon wave packet of the correlated photon up to a time uncertainty τ_2 would have to be expected. In parallel, the uncertainty ΔE in the photon wave packet energy would have to increase accordingly as specified by the uncertainty relation $\Delta E \cdot \Delta t \geq \hbar/2$. In analogy, the energy $E_{s,i}$ of both photons is uncertain up to the SPDC bandwidth $\Delta\nu$, but the sum of each photon's energy is bound by the phase matching condition (2.7) [3]. The time uncertainty Δt only defines the time interval after which the expectation value $\langle E \rangle$ of a state varies appreciably, i.e. the time interval under which the system described by $|\Psi\rangle$ remains unperturbed.

In this experiment photon pairs created at the SPDC process are used, as it is easy to verify that the conditions accounted for by Franson can very well be fulfilled by these. This has already been successfully demonstrated in [36, 37]. Their uncertainty τ_2 in their coincidence time is zero and therefore well below the resolution of common single photon detectors.

Experimentally, the analysis of the entanglement in two dimensions can be carried out by the implementation of unbalanced interferometers on each of the correlated SPDC photon path (See Fig. (2.2)). The interferometer path length has to be chosen such

---

[3]It is to note that the time variable t defines the evolution of a particle's state $|\Psi\rangle$ but is not an operator, therefore the definition of an energy-time inequality based on the non-commutation relation of a "time" and energy operator requires some precautions.
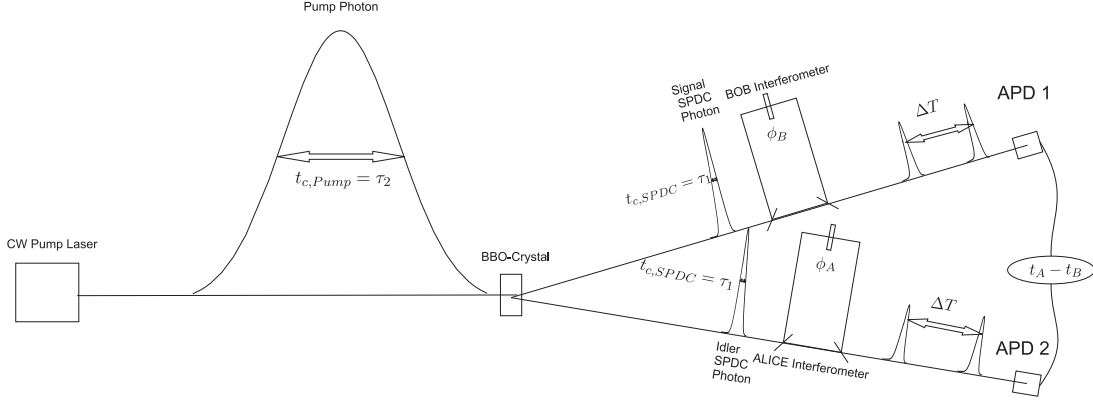
Figure 2.2: *Schematic representation of an experimental realization of energy-time entanglement experiment. A pump photon with the coherence length τ_1 emitted by the CW laser source is down-converted into two correlated photons at a BBO crystal. In order to analyze the energy-time entangled state, each correlated photon is sent through an unbalanced one-arm interferometer respectively, such that photons taking a distinct arm in the interferometers are delayed by ΔT with respect to each other. The coherence length of the pump source τ_1 holds to the condition $\tau_1 >> \Delta T$*

that the implemented time delay ΔT is much higher than their coherence time τ_2 as well as higher than the maximal resolution achievable with common single photon detectors Δt_D. For simplicity, these can be labelled as Alice's and Bob's analysis interferometers introducing a time delay ΔT between photons taking the short and long path respectively. To carry out the analysis of the SPDC biphoton state, Alice and Bob are provided with the independent relative phase adjustments ϕ_A and ϕ_B the photons acquire in the respective interferometers.

The other condition envisioned by Franson, that the indistinguishability in creation time τ_1 of both SPDC photons, i.e. the coherence time of the pump source, is much higher than the time delay ΔT introduced by the interferometers, can easily be implemented experimentally (See section (4.1.1)).

For simplification, the notation $|i\rangle|j\rangle \cong |i \cdot \Delta T\rangle|j \cdot \Delta T\rangle$ has been introduced. Only the correlation between one pair of detectors at one output of each interferometer will be considered for the moment.

After projecting the photon state onto the coincidence time $\Delta t = t_A - t_B$ between both SPDC photons the coincident photons can be detected at three possible detection times $(-\Delta T, 0, \Delta T)$ and can be described as being projected into the biphoton states $|0\rangle_A|1\rangle_B, |0\rangle_A|0\rangle_B, |1\rangle_A|1\rangle_B$ and $|1\rangle_A|0\rangle_B$ (See Fig. 2.3.). In parallel, the two biphoton states $|0\rangle_A|0\rangle_B$ and $|1\rangle_A|1\rangle_B$ remain indistinguishable in their time of detection, as long as the path length difference in both interferometers is kept equal up to the coherence length l_c of the SPDC photons.

Note that only a postselection procedure on the coincidence probabilities with time delay $\Delta t = 0$ will warrant that only the count rates for perfectly indistinguishable

biphoton states are being selected.
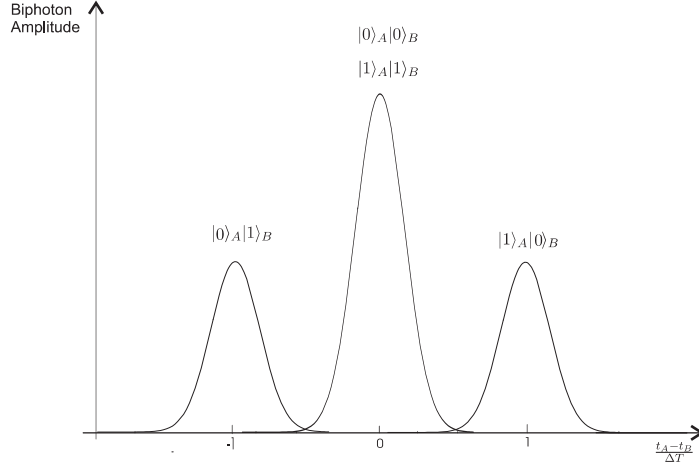
Figure 2.3: *Schematic presentation of the four biphoton state amplitudes in the coincidence time basis. The two biphoton states $|0\rangle_A|0\rangle_B$ and $|1\rangle_A|1\rangle_B$ overlap up to the coherence time of the SPDC photons and under the conditions $\Delta T = \Delta T_A = \Delta T_B \pm \tau_2$ and $\tau_1 >> \Delta T$ superpose to an entangled state $|\Psi\rangle_{AB} = 1/\sqrt{2} \cdot (|0\rangle_A|0\rangle_B + e^{i \cdot (\phi_A + \phi_B)}|1\rangle_A|1\rangle_B)$.*

These postselected biphoton states are $|0\rangle_A|0\rangle_B$ and $|1\rangle_A|1\rangle_B$. Once one correlated SPDC photon pair has been detected in the state $|0\rangle_A|0\rangle_B$ their path through the interferometer still remains indistinguishable with respect to the correlated photon pair's path $|1\rangle_A|1\rangle_B$.

Therefore, the entangled state can be written as the coherent superposition of both biphoton states, as a function of the relative phases ϕ_A and ϕ_B each correlated photon acquires in the respective interferometer arms:

$$|\Psi\rangle_{AB} = 1/\sqrt{2} \cdot (|0\rangle_A|0\rangle_B + e^{i \cdot (\phi_A + \phi_B)}|1\rangle_A|1\rangle_B) \tag{2.12}$$

with $\phi_A = \phi_{l,A} - \phi_{s,A}$ and $\phi_B = \phi_{l,B} - \phi_{s,B}$ being the phase differences between the respective long and short paths in the interferometers.

Having implemented a path length difference $\Delta T \propto 2ns$ much higher than the SPDC photon coherence length $\tau_2 \propto 100fs$ ensures that the probability for single photon interference is negligible: The expected interference pattern can only be explained as two-photon interference between both biphoton states in relation to the accumulated phase $\phi_A + \phi_B$ in both interferometers. The two photon interference pattern has an envelope with a FWHM given by the single photon coherence length $l_{c,SPDC}$.

The evaluation of the coincidence count rate between both photons detected at two detectors separated by space-like distances is not trivial, and is better studied using second order quantized fields. A detailed calculation for two general real valued amplitudes α and β for both two-photon states $|0\rangle_A|0\rangle_B$ and $|1\rangle_A|1\rangle_B$ will be derived in the Appendix.

There it is shown that the coincidence function P_c between two pairs of detectors can be parameterized as

$$
\begin{aligned}
P_c(\phi_A, \phi_B) \;=\; & \\
& 1/2(\alpha^2 + \beta^2 + 2 \cdot \alpha\beta \cdot cos(\phi_A + \phi'_B)) = \\
& 1/2(\alpha + \beta)(1 + 2 \cdot \alpha\beta \cdot /(\alpha^2 + \beta^2) \cdot cos(\phi_A + \phi'_B) = \\
& M \cdot (1 + V \cdot cos(\phi_A + \phi'_B)), \hspace{2cm} (2.13)
\end{aligned}
$$

with the normalization constant $M = (\alpha + \beta)/2$ of both amplitudes and with the two photon visibility $V = 2 \cdot \alpha\beta \cdot /(\alpha^2 + \beta^2)$. In Bob's phase setting $\phi'_B = \phi_B + \frac{\omega_{k_P}\Delta T}{\hbar}$ a constant offset given by the frequency of the pump photon is included.

According to this simple calculation the maximum theoretically achievable visibility V for the coincidence probability is $V = 100\%$ for $\alpha = \beta = 1/2$, i.e. for perfect beamsplitters. A further reduction in the visibility can be expected due to the finite coherence length $l_{c,SPDC}$ of the SPDC photons as a function of the ratio between the path length differences $\Delta L_A - \Delta L_B$ between both interferometers and $l_{c,SPDC}$. For SPDC photons being filtered out by filters with Gaussian frequency transmission, the reduction in the visibility can be parameterized [16] as

$$
V' = V \cdot e^{-((\Delta L_A - \Delta L_B)/l_{c,SPDC})^2} \hspace{2cm} (2.14)
$$

.

As discussed in section (2.6), for interferometers being of the all-fibre configuration, dispersion effects in the silica material of the fibres would introduce an additional mismatch between the time distribution of the biphoton amplitudes. Therefore, the two photon interference would be reduced accordingly.

Following the same arguments as Bell when formulating his famous Bell-inequality for Spin 1/2 particles [26], it is possible to derive a theoretical bound, the Bell parameter S, for which a local hidden variable theory is able to provide a coherent description of the two photon interference correlations observed between photons detected at the different output arms of Alice's and Bob's interferometers. As quantum mechanics is based on assumptions violating this experimental bound, the energy-time entangled nature of the correlated photons can be proven.

At this point it will suffice to point out that a relation between the two photon interference visibility V and the Bell parameter S for an energy-time correlated state can be derived. This will be done in section (2.5.). Here it will suffice to note that a bound of $V \geq 70,7\%$ in the interference visibility is necessary to show the violation of a energy-time Bell inequality.

2.4 Time-bin entanglement

This section describes a slightly different concept of entanglement on the time basis centred on pulsed sources of SPDC photons. A correct designation for this entanglement scheme would be "gated" energy-time entanglement: The entangled photon pairs have well defined emission times instead of being undetermined over a large pump laser coherence time as for energy-time entanglement. The advantages of this implementation of energy-time entangled states with respect to the realization of higher dimensional entanglement will be discussed. Time bin entanglement for two dimensions and for a higher dimension will be presented. The emission of multiple SPDC photon pairs enhanced at higher pump powers and its detrimental effect for the quality of the entanglement will be treated too.

### 2.4.1 Two dimensional time-bin entanglement

The different designation of "time-bin" entanglement with respect to energy-time entanglement is necessary, as the preparation of time-bin entangled Bell states requires some modifications in the theoretical background and the experimental implementation. The first difference is the employment of pulsed sources of SPDC photons, i.e. ps-pulsed diodes or fs-pulsed Ti:sapphire lasers as already have been successfully implemented in diverse experiments [38, 39]. Due to their resonant cavity, fs-lasers are characterized by the fact that the pulse phase can be kept stable over several pulses, while pulses produced by diode lasers aren't coherent to each other, as with each modulation of the bias current, needed for pulsing the diode, the photon's phase will have changed. For the time bin experiment planned in this work pulsed laser diodes are to be implemented.

The first important requirement in order to achieve energy-time entanglement as presented in section (2.3), the supremacy of the pump laser coherence time over the time delay ΔT introduced by the respective analyzer interferometers $\tau_1 >> \Delta T$, therefore cannot be fulfilled.

However, the implementation of an additional stabilized interferometer in the path of the pump beam offers the most straightforward solution (See Fig. (2.4.)), as a pump photon is split up into two pulses $|0\rangle$ and $|1\rangle$ with a fixed phase relation and time delay ΔT, i.e. "time bins" with respect to each other. The pump photon emission time now consists of two well defined creation times 0 and ΔT up to the pulse width of the laser Δt_P. Therefore the initial pump photon state can be defined as

$$|\Psi_P\rangle = 1/\sqrt{2}(|0\rangle + e^{i\cdot\phi_P}|1\rangle) \tag{2.15}$$

where again the notation $|n\rangle \cong |n\cdot\Delta T\rangle$ has been introduced.
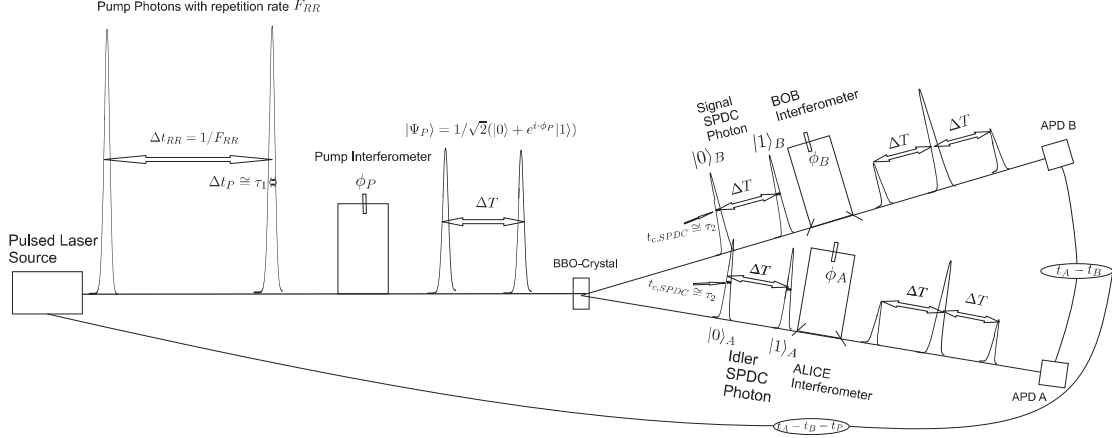
Figure 2.4: *Proposed setup for preparing and analyzing time-bin entangled qubits. Displayed are the biphoton states for a pump photon being emitted by the pulsed laser with a repetition rate F_{RR}. Before undergoing the process of SPDC at the BBO crystal with an efficiency $\propto 10^{-10}$, it is split up into two coherent pump pulses with fixed time delay ΔT and phase ϕ_P, i.e. "time-bins", by an additional pump interferometer. The pump photon state can be written as $\Psi_P = 1/\sqrt{2}(|0\rangle + e^{i\cdot\phi_P}|1\rangle)$. The state after the SPDC process will read as $\Psi_{SPDC} = 1/\sqrt{2}(|0\rangle_A|0\rangle_B + e^{i\cdot\phi_P}|1\rangle_A|1\rangle_B)$. Alice and Bob analyze the entangled state by setting their corresponding relative phases ϕ_A and ϕ_B the photons accumulate when being guided through the respective analyzer interferometers. Nevertheless, only the measurement of the time delays with respect to the emission time t_P of the pump photon and a postselection of the indistinguishable biphoton states will allow the analysis of the entangled state.*

After passing through the BBO crystal SPDC photon pairs can be emitted in any of the two time bins. The SPDC state therefore reads as

$$|\Psi_{SPDC}\rangle = 1/\sqrt{2}(|0\rangle_A|0\rangle_B + e^{i\cdot\phi_P}|1\rangle_A|1\rangle_B), \tag{2.16}$$

which is a Bell state. With this simple configuration only two out of the four Bell entangled states can be prepared by changing the relative phase.

In difference to energy-time correlated states, now there are two possible well defined creation times, i.e. time bins, for the SPDC photon pairs: 0 and ΔT. Their coherence time τ_2 remains still smaller than the pulse length Δt_p. The detection of one photon in one of the two possible time bins will only determine the emission time of the correlated photon in the same time bin up to a much smaller uncertainty τ_2. Nevertheless, a fixed relative phase relation exists between the SPDC biphoton states created in the different time-bins due to the coherent transformation introduced by the pump interferometer.

A straightforward way to analyze this coherent relation between the different time bins consists in using two analyzer interferometers at Bob's and Alice's site introducing the same time delay $\Delta T \pm \tau_2$ as by the pump interferometer. This will warrant that the biphoton states of the SPDC photons created in different time bins can be made to

overlap in time again and to interfere, as long as the conditions which will be described in this section are fulfilled.

For illustrative purposes the biphoton states will be defined by the number of interferometer time delay units ΔT each photon has acquired while traversing the pump and its respective analyzer interferometer. Demonstratively, the photon state of a photon going though the short arm in both interferometers will be denoted as $|0\rangle$ while for a photon travelling through any long arm of both interferometers the state will be denoted as $|1\rangle$ and as $|2\rangle$ for having taken the long path in both interferometers.

Using this notation, the original biphoton state of Eq. (2.16) transforms into

$$
\begin{aligned}
|\Psi\rangle = \frac{1}{2\sqrt{2}}(|0\rangle_A|0\rangle_B &+ e^{i\cdot\phi_A}|1\rangle_A|0\rangle_B + e^{i\cdot(\phi_A+\phi_P)}|2\rangle_A|1\rangle_B \\
&+ e^{i\cdot\phi_B}|0\rangle_A|1\rangle_B + e^{i\cdot(\phi_B+\phi_P)}|1\rangle_A|2\rangle_B \\
+(e^{i\cdot(\phi_A+\phi_B)} + e^{i\cdot\phi_P})&|1\rangle_A|1\rangle_B + e^{i\cdot(\phi_A+\phi_B+\phi_P)}|2\rangle_A|2\rangle_B)
\end{aligned}
\tag{2.17}
$$

A projection onto the detection time differences $t_A - t_B$ between the SPDC photons at Alice's and Bob's detectors will demonstrate that the coincidence times of the photon pairs are distributed over three well defined detection times $-\Delta T$, 0 and ΔT, as depicted in Fig. (2.5).

In difference to the Franson experiment the postselection of coincident biphoton states doesn't warrant their indistinguishability, as each SPDC biphoton state has a well defined creation time Δt_P much smaller than the chosen interferometer time delay ΔT. Once the detection time of a coincidence is triggered to the pulsed laser repetition rate, it would be possible to determine each photon's path through the interferometer. For example the biphoton state $|1\rangle_A|1\rangle_B$ corresponds to a SPDC photon pair having acquired a time delay ΔT, while the biphoton state $|2\rangle_A|2\rangle_B$ is delayed by $2\Delta T$ with respect to the emission time t_P of the SPDC photon.

Therefore, two-photon interference is possible only once the photon arrival times of the photons are triggered to the emission time of the pump laser. Once the measured coincidence count rate is limited to the postselection window 0 the analysis is fixed on the biphoton states $|0\rangle_A|0\rangle_B, |1\rangle_A|1\rangle_B$ and $|2\rangle_A|2\rangle_B$. With respect to the pulse time t_P, the three biphoton states are distributed over three distinct possible discrete times 0, ΔT and $2\Delta T$ as depicted in Fig. (2.6). The amplitude of the central peak is double as high as for the two side peaks, what has to do with the fact that the path of a pump and their corresponding SPDC photons weren't denoted separately in the preceding discussions. Indeed the central peak can be denoted as the indistinguishable superposition of a pump photon having taken the long interferometer path (acquiring a time delay ΔT) and the down-converted photon pairs having taken the short interferometer path (not acquiring any delay) $|1\rangle_P|0\rangle_{A,B}$ and vice versa $|0\rangle_P|1\rangle_{A,B}$.
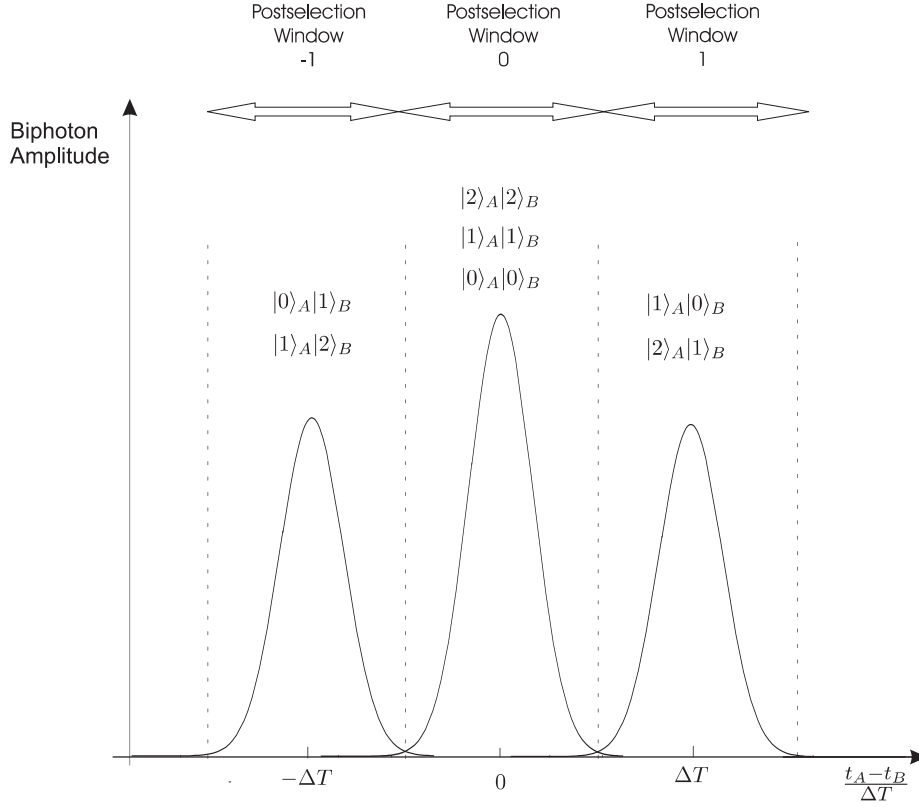
Figure 2.5: *Schematic description of the SPDC biphoton states after passing through the setup described in Fig. (2.4) and with respect to their detection time difference $t_A - t_B$. The different possible postselection windows are displayed. However a two dimensional entangled state can only be extracted by measuring on the Postselection Window (PW) 2.*

For illustrative purposes the notation has to be changed accordingly as used in Fig. (2.6):

$$|0\rangle_A |0\rangle_B \rightarrow |0\rangle_P |0\rangle_{A,B}$$
$$(e^{i\cdot(\phi_A+\phi_B)} + e^{i\cdot\phi_P})|1\rangle_A|1\rangle_B \rightarrow e^{i\cdot(\phi_A+\phi_B)}|0\rangle_P|1\rangle_{A,B} + e^{i\cdot\phi_P}|1\rangle_P|0\rangle_{A,B}$$
$$e^{i\cdot(\phi_A+\phi_B+\phi_P)}|2\rangle_A|2\rangle_B \rightarrow e^{i\cdot(\phi_A+\phi_B+\phi_P)}|1\rangle_P|1\rangle_{A,B}$$

It is possible to extract from Fig. (2.6.) that the postselected biphoton states in the postselection window 1 are SPDC biphoton states actually created in the two distinct time bins $|0\rangle_P$ and $|1\rangle_P$, but coinciding again in their respective detection times due to the additional delay by ΔT in the respective analyzer interferometers. Both biphoton states $|1\rangle_P|0\rangle_{A,B}$ and $|0\rangle_P|1\rangle_{A,B}$ are indistinguishable with respect to each other as long as the time delays introduced in the pump and both analyzer interferometers are equal up to the SPDC photon's coherence time τ_2. Therefore, according to the superposition principle, the state can be written as
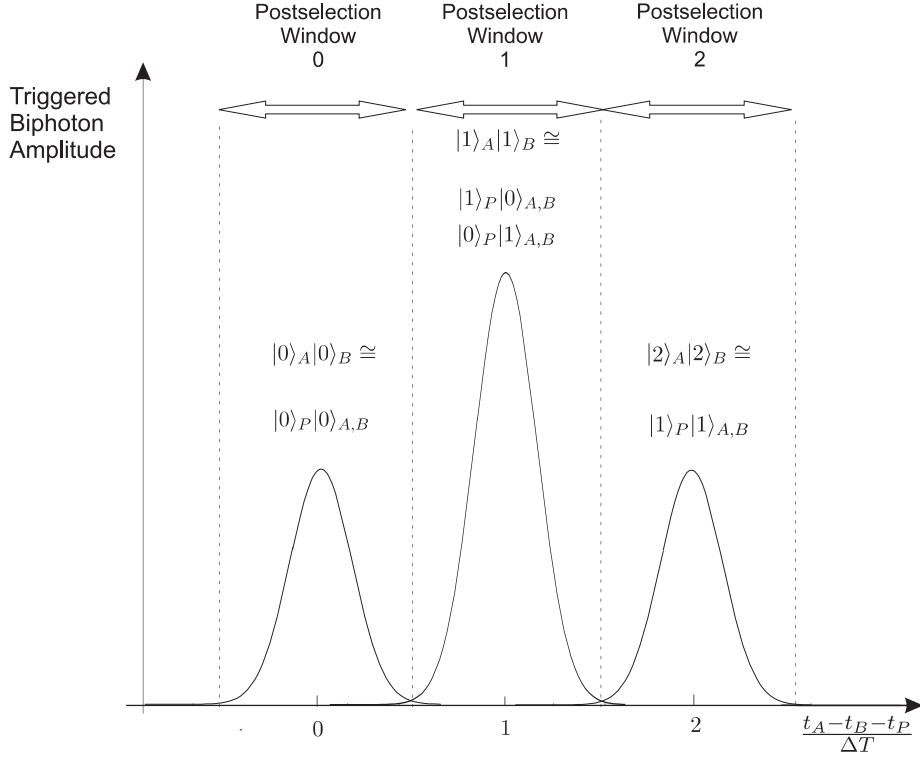
Figure 2.6: *Schematic description of the SPDC biphoton amplitudes after their passing through the setup described in Fig. (2.6) and with respect to the pulsed pump laser trigger time t_p. Setting the time basis at the postselection window 1 will project the photon state onto $\Psi = e^{i \cdot (\phi_A + \phi_B)}|0\rangle_P|1\rangle_{A,B} + e^{i \cdot \phi_P}|1\rangle_P|0\rangle_{A,B}$, a time-bin entangled state.*

$$|\Psi\rangle = e^{i \cdot (\phi_A + \phi_B)}|0\rangle_P|1\rangle_{A,B} + e^{i \cdot \phi_P}|1\rangle_P|0\rangle_{A,B} = (e^{i \cdot (\phi_A + \phi_B)} + e^{i \cdot \phi_P})|1\rangle_A|1\rangle_B \quad (2.18)$$

such that two photon interference can be expected in the coincidence count rates of the photons triggered to the pulse photon emission time and in dependence of the relative phase settings ϕ_A and ϕ_B.

It can be argued, that the interference to be expected in the triggered coincidence count rates is indeed only due to two-photon interference between both postselected biphoton states. The possibility to attribute this effect to interference of first order between photon pairs emitted at the two possible time bins 0 and ΔT is discarded, as the coherence length of both SPDC photon pairs is limited to values lower than the time delay ΔT between the time bins due to the pulsed character of the source. Therefore, both considered SPDC biphoton states aren't coherent to each other, although a fixed phase relation ϕ_P exists between both states.

Again the quality of the entanglement can be quantified by the two photon interference visibility observed while changing any of the phases in the analysis interferometers. This will be discussed in section (2.5.).

2.4.2   Higher dimensional time bin entanglement

Higher dimensional entanglement has motivated the interest of the scientific community since the first publication on entanglement of two qudits, i.e. particles whose state is prepared in a d dimensional Hilbert space, by Peres [20]. The question of interest is, whether for dimensions $d \to \infty$ quantum theory still asymptotically violates a Bell inequality, i.e. whether in the limit of large quantum numbers the emergence of classical properties, being explainable by a Local Hidden Variable Theory (LHVT), could be expected. However, in this paper it could be shown that the Bell Parameter S for an entangled Spin-j biphoton system was still larger than the one predicted by a LHVT in the limit $j \to \infty$: $S_{QM} = 2,481 > 2 = S_{LHVT}$.

Similarly, in [40] it was demonstrated that for dimensions up to $d = 9$ the violation of local realism is maximized. Analogously it was demonstrated that the upper bound for the maximal noise tolerated by maximally entangled systems decreases in a higher dimensional Hilbert space, showing the increasing robustness of higher dimensional entanglement [40]. This fact has also enhanced the interest in implementing qudits in quantum key distribution (QKD) protocols, as the robustness of entanglement with respect to noise is usually the main criteria for quantifying the security of these protocols. Analogously, it is expected that a detector loop-hole free test of entanglement could be easier to be provided for higher dimensional entanglement as for these states the critical quantum efficiency η of the detectors is lowered [40].

However the discussions in [40] and one experimental implementation [33] are centred onto qudits $\Psi(d) = 1/\sqrt{d} \sum_{m=1}^{d} |m\rangle_A |m\rangle_B$ prepared by the selection of correlated spatial modes of SPDC photons and analyzed by coupling each mode $|m\rangle_A$ and $|m\rangle_B$ into the d input ports of separate $d \times e$ multiport beamsplitters. These beamsplitters for which each of the photons coupled into one of its d input ports can be randomly guided into any of the e outputs are provided with appropriate settings of the phase shifts Φ_m^A and Φ_m^B. As presented in [33], the defining characteristic of a symmetric multiport beam splitter is its unitary transition matrix $U_{ij}^d = \langle j|U^d|i\rangle = 1/\sqrt{d}\gamma_d^{(j-1)(i-1)}$ with $\gamma_d = e^{i \cdot 2 \cdot \pi/d}$.

In this work the way chosen to implement higher dimensional entanglement is a natural extension of the time bin scheme with the implementation of additional interferometer arms in series (see Fig. (2.7)) and only two detectors placed at the two outputs of the multiple-path interferometer configuration. It is to note that each interferometer arm has to be chosen to implement the double time delay as the previous one. Instead of the multiport scheme, requiring d interferometer arms for preparing and analyzing the state in the d dimensional Hilbert space, this scheme requires only $log_2 d$ arms, as for each interferometer arm m, $2^m = d$ different paths can be taken by the photons for $m \in 0, 1, 2, ...$. Therefore the experimental effort is reduced.
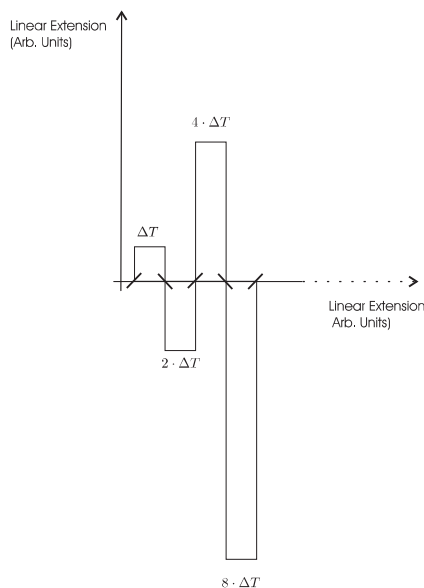
Figure 2.7: *A multi-path interferometer configuration has to be implemented in the time-bin scheme for each of the analyzer and pump interferometers. Each implemented beam splitter has a symmetric splitting ratio. Each interferometer arm implements the double time delay as the previous one. No adjustable phase setting is associated to each arm, as these have to be addressed independently with phase modulators.*

One important reason for not choosing the energy-time entanglement scheme is that in this case the number of independent phase settings is inferior to the number of dimensions d in the Hilbert space of the photons:

With a 2 arm interferometer, enabling to encode the photons in a 4 dimensional Hilbert space, only 2 phase settings would be available, for example.

This problem can be circumvented with the time bin entanglement scheme, as the possibility to trigger each time bin separately to the pulsed laser rate enables the implementation of phase modulators [4], such that a phase setting can be associated to each time-bin independently.

Following this scheme, the qudit state can be prepared using a $m = log_2 d$ arm pump interferometer such that the pump photon is split up into d time bins $|i\rangle$. The state reads as

$$|\Psi_P\rangle = 1/\sqrt{d} \sum_{i=0}^{d-1} |i\rangle_P \tag{2.19}$$

and after the down conversion process at the BBO crystal the correlated photon pair's state is

---

[4]Devices enabling to switch the phase of an optical wave by electro-optical effects in photonic crystals

$$|\Psi_P\rangle = 1/\sqrt{d} \sum_{i=0}^{d-1} |i\rangle_A |i\rangle_B \qquad (2.20)$$

Here, the relative phase settings in each interferometer arm are considered to be kept stable and equal $\phi_{P,i} = 0$ and are not taken explicitly as a degree of freedom for preparing the state. As mentioned before, the number of these phase settings is inferior to the number of dimensions encoded, such that no independent phase would be settable for each dimension.

For Bob's and Alice's analysis of the prepared state, the phase setting in the higher dimensional Hilbert space of the entangled photon state can be addressed by two different phase modulators, into which the photons are coupled before their analysis in the respective interferometer arms is undertaken. For each encoded dimension a phase setting $\phi_{A,0}, \phi_{A,1}, ..., \phi_{A,d-1}$ and $\phi_{B,0}, \phi_{B,1}, ..., \phi_{B,d-1}$ is to be set. Bob's and Alice's analysis interferometers have the same configuration as for the pump interferometer and allow them to make SPDC photon pairs emitted in different time bins coincide again.

As the pump and both SPDC photons can have taken up to d different paths in each of the 3 interferometers respectively, the photon pairs can have acquired up to d^3 different time delays with respect to each other.

The SPDC photon pairs are distributed with equal probability [5] over any of the d^3 different biphoton states $|i \cdot \Delta T\rangle_A |j \cdot \Delta T\rangle_B$ with $i, j \in 0, 1, ..., 2d-1$ as a function of the time delays ΔT introduced by any of the arms of the pump and analyzer interferometers.

$$
\begin{aligned}
|\Psi_{DC,P}\rangle \;=\; & 1/\sqrt{d} \sum_{i=0}^{d-1} |i\rangle_A |i\rangle_B \rightarrow |\Psi_{DC,AB}\rangle = \qquad\qquad (2.21)\\[2mm]
& \frac{1}{\sqrt{d}\cdot d}[e^{i(\phi_{A,0}+\phi_{B,0})}|0\rangle_A|0\rangle_B + e^{i(\phi_{A,0}+\phi_{B,1})}|0\rangle_A|1\rangle_B \\[1mm]
& + e^{i(\phi_{A,1}+\phi_{B,0})}|1\rangle_A|0\rangle_B + e^{i(\phi_{A,1}+\phi_{B,1})}|1\rangle_A|1\rangle_B + ... + \\[1mm]
& e^{i(\phi_{A,d-2}+\phi_{B,d-2})}|d-2\rangle_A|d-2\rangle_B + e^{i(\phi_{A,d-2}+\phi_{B,d-1})}|d-2\rangle_A|d-1\rangle_B \\[1mm]
& + e^{i(\phi_{A,d-1}+\phi_{B,d-2})}|d-1\rangle_A|d-2\rangle_B + e^{i(\phi_{A,d-1}+\phi_{B,d-1})}|d-1\rangle_A|d-1\rangle_B \\[1mm]
& + ... + e^{i(\phi_{A,0}+\phi_{B,0})}|d\rangle_A|d\rangle_B + e^{i(\phi_{A,0}+\phi_{B,1})}|d\rangle_A|d+1\rangle_B \\[1mm]
& + e^{i(\phi_{A,1}+\phi_{B,0})}|d+1\rangle_A|d\rangle_B + e^{i(\phi_{A,1}+\phi_{B,1})}|d+1\rangle_A|d+1\rangle_B + ... + \\[1mm]
& e^{i(\phi_{A,d-1}+\phi_{B,d-2})}|2d-2\rangle_A|2d-2\rangle_B + e^{i(\phi_{A,d-2}+\phi_{B,d-1})}|2d-2\rangle_A|2d-1\rangle_B + \\[1mm]
& e^{i(\phi_{A,d-1}+\phi_{B,d-2})}|2d-1\rangle_A|2d-2\rangle_B + e^{i(\phi_{A,d-1}+\phi_{B,d-1})}|2d-1\rangle_A|2d-1\rangle_B]
\end{aligned}
$$

A more intuitive description of the physical meaning of this state is given in Fig. (2.8), where the biphoton states are distributed over 2d-1 postselection windows each

---

[5]Each beamsplitter has an ideal symmetric splitting ratio

covering exactly one distribution peak. However, the amplitude of the superposing biphoton states varies from window to window, and, as will be shown subsequently, depends on the dimension of the maximally entangled state to be analyzed.
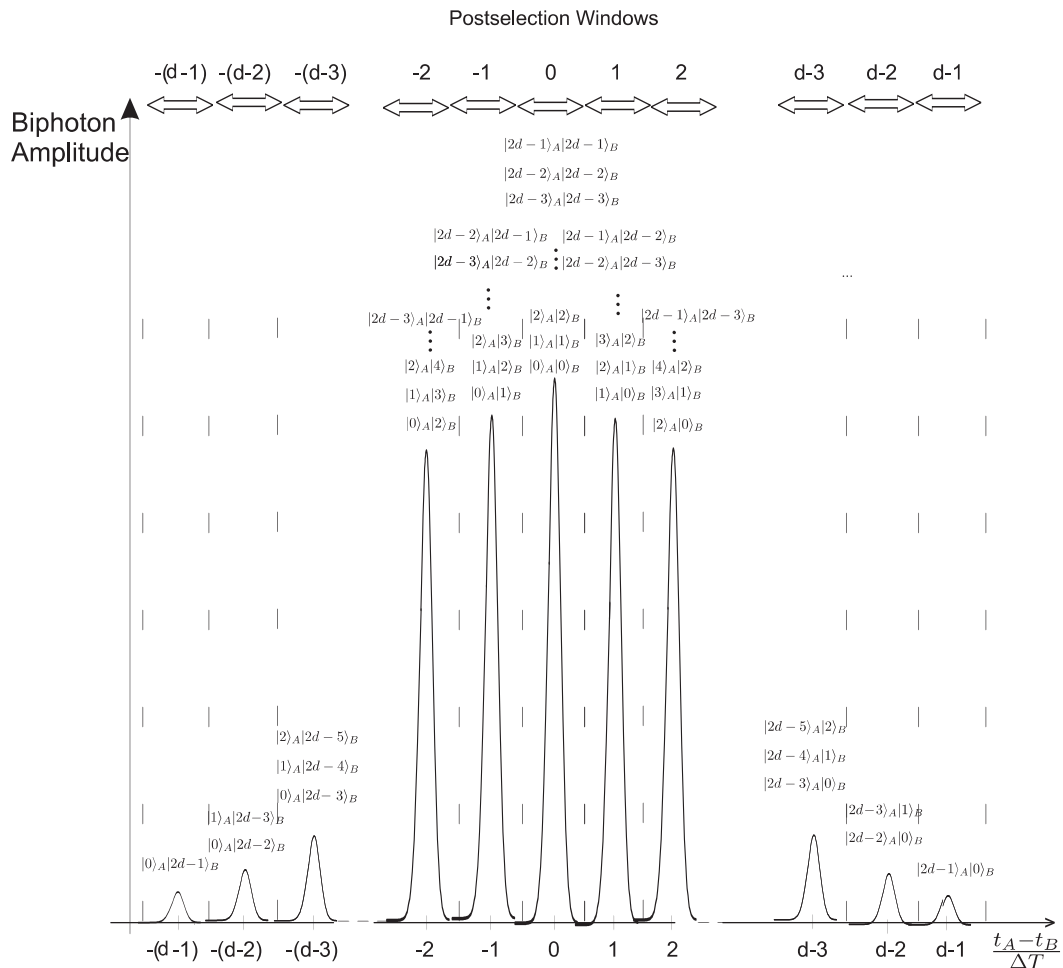
Figure 2.8: *Schematic description of the amplitudes for the SPDC biphoton states after their passing through the three d arm interferometers and with respect to their detection time difference $(t_A - t_B)$. A postselection projection into any of the $2d - 1$ postselection windows is possible, which corresponds to a projection into a specific Hilbert space of a specific dimension $\leq d$ of the photon states. However the entangled nature of the photon pairs can be analyzed only by measuring in the $(t_A - t_B - t_P)$ time basis, as displayed in Fig. (2.9)*

For the subsequent discussion only a projection into the postselection window 0 in the $t_A - t_B$ time basis will be considered. This window selects coincidence counts for SPDC photon pairs having taken the same path in their respective analyzer interferometers. The photon pairs postselected at the different side peaks are delayed by exactly the same amount multiple of ΔT:

$$t_A - t_B = d \cdot \Delta T$$

Nevertheless, for each of these PWs, the which path information of each photon pair through the interferometers can easily be extracted by triggering the photon arrival time to the emission time of the corresponding pump photon such that the biphoton states in each postselection window (PW) are distinguishable with respect to each other. Again, this is solved by projecting the state of the selected postselection window into the $(t_A - t_B - t_P)$ time basis, as depicted in Fig. (2.9.). In this basis, each biphoton state $|i\rangle_A|j\rangle_B$ with $(i,j) \in [0, 2d-1]$ is again distributed over 2d-1 different peaks, triggered to the emission time of the pump photon t_P.

For clarification, a change in notation $|i\rangle_A|i\rangle_B \rightarrow |i\rangle_P|j\rangle_{A,B}$, defining each photon's time delay acquired in the pump and analyser interferometers distinctly, will be necessary. For example:

$$(e^{i(\phi_{A,0}+\phi_{B,0})} + e^{i(\phi_{A,1}+\phi_{B,1})} + ... + e^{i(\phi_{A,d-1}+\phi_{B,d-1})})|d-1\rangle_A|d-1\rangle_B \rightarrow$$
$$e^{i(\phi_{A,0}+\phi_{B,0})}|d-1\rangle_P|0\rangle_{A,B} + e^{i(\phi_{A,1}+\phi_{B,1})}|d-2\rangle_P|1\rangle_{A,B} + ...$$
$$+e^{i(\phi_{A,d-1}+\phi_{B,d-1})}|0\rangle_P|d-1\rangle_{A,B} \qquad (2.22)$$

In Fig. (2.9) the distribution of the biphoton states are depicted for both chosen notations in order to clarify how the maximally entangled states are realized.

The selection of the coincidence counts in the postselection window 0 in Fig. (2.9.) triggered to the pump photon emission time will allow to project the biphoton states into the higher dimensional Hilbert space with dimension d:

$$|\Psi_d\rangle = \frac{1}{\sqrt{d}}(e^{i(\phi_{A,0}+\phi_{B,0})}|d-1\rangle_P|0\rangle_{A,B} + e^{i(\phi_{A,1}+\phi_{B,1})}|d-2\rangle_P|1\rangle_{A,B} + ...$$
$$+e^{i(\phi_{A,d-2}+\phi_{B,d-2})}|1\rangle_P|d-2\rangle_{A,B} + e^{i(\phi_{A,d-1}+\phi_{B,d-1})}|0\rangle_P|d-1\rangle_{A,B}). \qquad (2.23)$$

The state can be interpreted as the superposition of all the d different possible paths the postselected photon pair could have taken on its way through the pump and analysis interferometers, such that both photons have been delayed by $d \cdot \Delta T$. Following the same discussion as in the sections before, it has to be warranted that the respective time delays $\Delta T, 2 \cdot \Delta T, ..., 2^{d/2} \cdot \Delta T$ introduced in the three interferometers are respectively equal up to the SPDC photon's coherence time in order to warrant the indistinguishability of all postselected biphoton states. In the same way a stable and fixed phase relation has to be warranted for in each interferometer arm, such that the phases in the prepared entangled stated are only determined by the phase modulator settings.
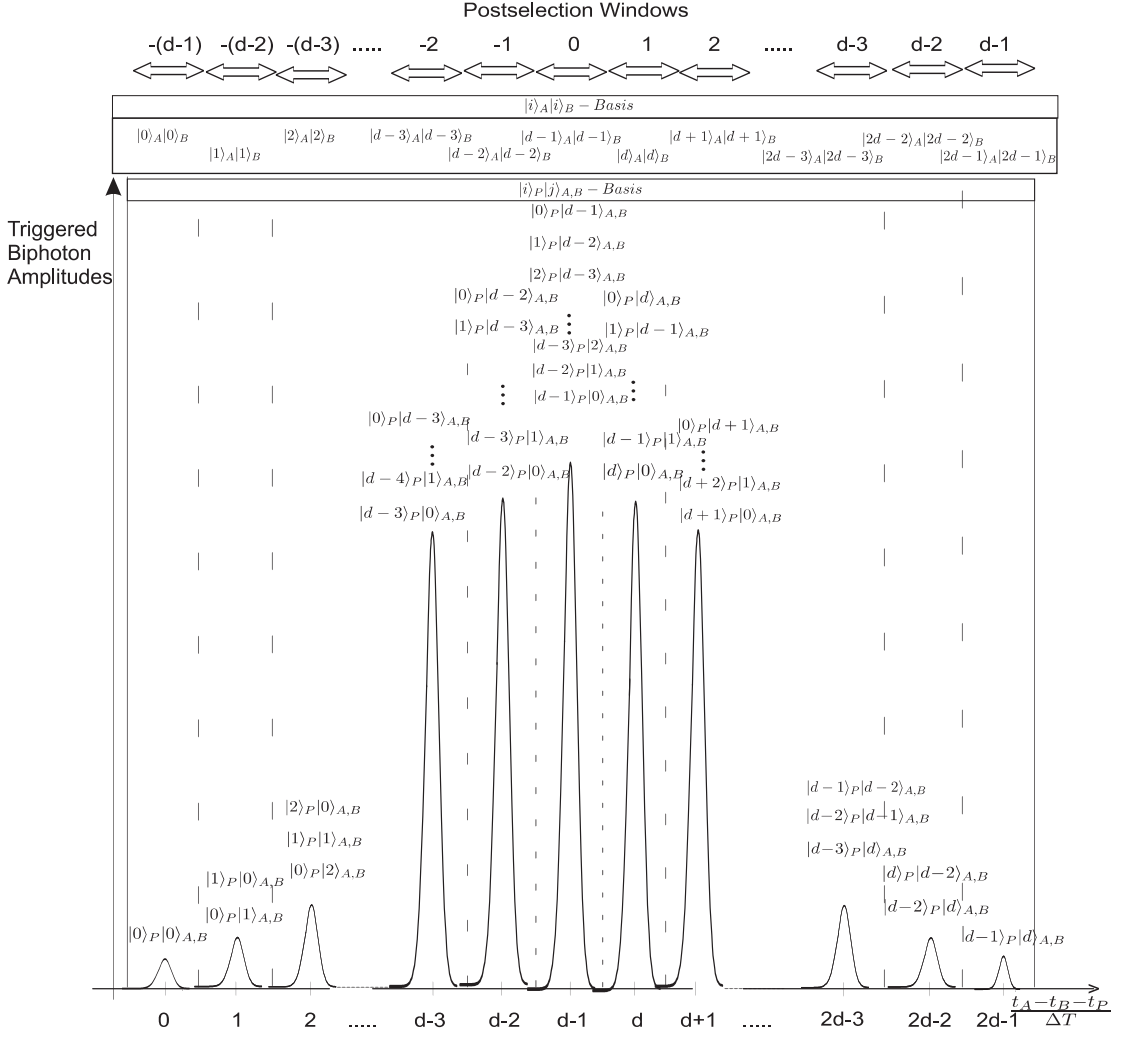
Figure 2.9: *Schematic description of the SPDC biphoton states amplitude in the $(t_A - t_B - t_P)/\Delta T$ time basis. For clarification, the biphoton states depicted are both described in the $|i\rangle_A|i\rangle_B$ and the $|i\rangle_P|j\rangle_{A,B}$ notation. A postselection projection into any of the 2d-1 postselection except the first and the last windows corresponds to the projection of the photonic state into a higher dimensional maximally entangled state. The dimension is different for every postselection window and is limited to d.*

However, the discussion presented here is analogous for the states analysed when choosing any of the $2d - 1$ different postselection windows except the first and last one in the $(t_A - t_B)$ time basis. Nevertheless, the dimension of these states is smaller than d. For any of these PWs no additional timing information can be extracted once a measurement in the $(t_A - t_B - t_P)$ time basis is performed, yielding that the prepared states are maximally entangled, too.

Considering these facts, we see that the scheme presented here is very well suited for selecting a specific higher dimensional entangled state and for analyzing each dimension independently with the phase settings $\phi_{A,i}$ and $\phi_{B,i}$.

It is to note that the practical limitation with regards of the maximal dimension of the biphoton states to be encoded is given by the detector timing resolution Δt_d and by the time delay ΔT_{RR} between subsequent pulses emitted by the pulsed laser:

The path length difference ΔT has to be chosen to be larger than the timing resolution Δt_d. If not, the capability to distinguish between SPDC photon pairs emitted at the different time bins would be reduced. In order to avoid the overlap between photon pairs emitted by subsequent pulses, the total time delay has to be chosen as $(2d-1) \cdot \Delta T < \Delta T_{RR}$. With the implemented instruments, higher dimensional entanglement up to d=8, i.e. corresponding to the implementation of three arm preparation and analysis interferometers, should be feasible:

A d=8 dimensional entangled state reads as

$$|\Psi_8\rangle = \frac{1}{\sqrt{8}}(e^{i(\phi_{A,0}+\phi_{B,0})}|7\rangle_P|0\rangle_{A,B} + e^{i(\phi_{A,1}+\phi_{B,1})}|6\rangle_P|1\rangle_{A,B} + ... + e^{i(\phi_{A,6}+\phi_{B,6})}|1\rangle_P|6\rangle_{A,B} + e^{i(\phi_{A,7}+\phi_{B,7})}|0\rangle_P|7\rangle_{A,B}).$$

Nevertheless, the discussions presented here show that the preparation and analysis of entangled states is rather inefficient. Only a small portion of the triggered SPDC photon pairs are postselected. An approximation about the reduction in the coincidence count rates for a 4 and 8 dimensional entangled biphoton state can be found in section (5.1.).

2.4.3   Multiple Events

As experimentally investigated in [22], the possibility that multiple SPDC photon pairs are emitted with each down-converted pump photon increases with the power of the pump source. Specially for pulsed sources the peak power can correspond to values of several W, such that the multiple photon pair rate is highly enhanced. These multiple photon pairs are generally not prepared in the same entangled state as for single photon pairs and as single photon detectors cannot discriminate multiple from single photon pairs, a reduction of the entanglement quality in dependence of the multiple photon pair probability has to be expected. This could be experimentally verified in [22].

Therefore, for this experiment pulsed laser diodes with a peak power not exceeding the maximal CW power achievable for the diodes ($P_{max} \propto 60mW$) were considered.

As the probability to create multiple photon pairs depends on the efficiency of the down-conversion process, this factor has to be regarded, too, when dealing with crystals offering high effective nonlinearities.

2.5   Bell-Inequality for energy-time entangled states

The purpose of this section is to derive a CHSH inequality for energy-time entangled states. A violation of this inequality for the states considered in the previous section

would provide the definite proof that the SPDC photon pairs are indeed energy-time entangled. However, in this work a Bell inequality suited only for 2 dimensional systems will be derived.

2.5.1 Bell inequality for energy-time entangled states for two dimensions

Considering the proposal of the EPR paradox, Bell, in his seminal work, [26] devised an experiment designed to univocally show the incompleteness of quantum mechanics. By incompleteness was meant the impossibility to assign a local realistic model onto the predictions of quantum mechanics. The experimental settings Bell initially considered were based on anti-correlated Spin 1/2 particles having only interacted at their joint emission point and propagating in different directions. The analysis of the correlation was devised to be done by a Stern-Gerlach type measurement $\vec{\sigma}_x, \vec{\sigma}_y, \vec{\sigma}_z$ on the spins $\vec{\sigma}_1$ and $\vec{\sigma}_2$ of each particle. However, only perfectly anti-correlated particles, i.e. particles in a Singlet state were considered. Under this condition, the measurement results $\vec{\sigma}_1 \cdot \vec{a}$ on the photon's spin with respect to a selected analysis direction $\vec{a}$ parallel for both photons are restricted to measurement results $+1$ and -1.

Another Bell type theorem, the CHSH theorem, was proposed by Clauser, Horne, Shimony and Holt in 1969 [27] and extended in 1974 [41], such as to offer a straightforward application on particle systems to be prepared experimentally: The theorem could be applied on correlated particle systems where the measurement outcomes could be any real value within $[+1, -1]$.

The CHSH inequality can be applied on particle systems correlated in the energy-time basis, too, as considered in this work. Similar derivations can be found on publications on other energy-time entanglement experiments [42].

A Franson type experiment, as described in section 2.2, already offers the characteristics envisioned for a Bell type test: The two correlated photons only interacted at their emission time t_0 and propagate to two spatially separated analyzer interferometers for Alice and Bob who can choose the local settings ϕ_A and ϕ_B the photons acquire through their path in the respective interferometers. Classically, the experiment can be interpreted as a Bernoulli type experiment on the binary output values, $+1$ and -1 for a detection at output $+$ or at output $-$ respectively, as the photons are split randomly at the output beamsplitter of the respective interferometers.

However, for an energy- time entangled state

$$|\Psi\rangle_{AB} = 1/\sqrt{2} \cdot (|0\rangle_A |0\rangle_B + e^{i \cdot (\phi_A + \phi_B)} |1\rangle_A |1\rangle_B) \qquad (2.24)$$

as derived in section (2.3) for the Franson experiment, specific correlations can be expected. The biphoton states $|1\rangle_A |1\rangle_B$ and $|0\rangle_A |0\rangle_B$ represent the correlated possibilities

that the photon pairs have both taken either the long or the short arm of their respective interferometers, situated at a space-like distance from each other. As long as the indistinguishability between both biphoton states, projected into the $t_A - t_B$ time basis, is ensured, two photon interference can be observed:

Both photon pairs will either be detected in the detector pair $(+, +)$ or in the detector pair $(-, -)$, a correlation result which cannot be explained by a LHVT, as will be shown in the following.
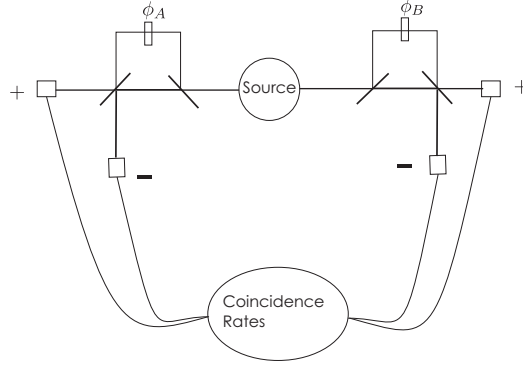
Figure 2.10: *Schematic representation of a Bell experiment for analyzing the energy-time correlations of the correlated photons. The photon pairs are created at the same source and are analyzed by Bob's and Alice's interferometers. The photons taking either the $(\pm, \pm)$ output of their respective interferometers are detected with single photon detectors.*

If the correlation measurements between the detectors are to be interpreted in the framework of a local hidden variable theory, the hidden variable λ has to be introduced. Assume that the measured single and coincident photon count rates are determined by the set of hidden variables $\lambda \in \Lambda$, which define the possible photon states after their creation but prior to their measurement. Once the measurement results $0 \leq P_\pm^A(\phi_A, \lambda) \leq 1$ and $0 \leq P_\pm^B(\phi_B, \lambda) \leq 1$ between the different $+$ and $-$ outputs of Alice's and Bob's interferometers are compared, the different correlation probabilities $P_{+,+}^{A,B}(\phi_A, \phi_B, \lambda), P_{+,-}^{A,B}(\phi_A, \phi_B, \lambda), P_{-,+}^{A,B}(\phi_A, \phi_B, \lambda), P_{-,-}^{A,B}(\phi_A, \phi_B, \lambda)$ can be extracted. However, experimentally testable observables, in this case the single photon count rates $N_{A,\pm}/N$, $N_{B,\pm}/N$ and correlation count rates $N_{A,B,\pm}/N$ with $N = \sum_\pm N_{A,B,\pm}$, have to be defined accordingly. This requirement can be met by setting

$$N_{A,\pm}/N := P_\pm^A(\phi_A) = \int_\Gamma P_\pm^A(\phi_A, \lambda)\rho(\lambda)d\lambda. \tag{2.25}$$

$$N_{B,\pm}/N := P_\pm^B(\phi_B) = \int_\Gamma P_\pm^B(\phi_B, \lambda)\rho(\lambda)d\lambda. \tag{2.26}$$

and

$$N_{A,B,\pm}/N := P_{\pm,\pm}^{A,B}(\phi_A, \phi_B) = \int_\Gamma P_\pm^{A,B}(\phi_A, \phi_B, \lambda)\rho(\lambda)d\lambda. \qquad (2.27)$$

where $\rho(\lambda)$ is the normalized probability density of the distribution of λ over its space Λ.

It is to note that due to the limited detection efficiency of the detectors, limiting the probability of a photon detection, the assumption that these probabilities are statistically equivalent to the measured count rates has to be met. This assumption is often referred to as the fair sampling condition, still leaving a so called detection called detection loophole for this experiment.

The condition of locality intrinsic to a LHVT can be met by requiring

$$P_{\pm,\pm}^{A,B}(\phi_A, \phi_B, \lambda) = P_\pm^A(\phi_A, \lambda) \cdot P_\pm^B(\phi_B, \lambda), \qquad (2.28)$$

i.e. the statistical independence between both probabilities $P_\pm^A(\phi_A, \lambda)$ and $P_\pm^B(\phi_B, \lambda)$: Assuming the objective nature of the biphoton states, i.e. their determination by the set of hidden variables λ, the local setting ϕ_B of the photon analyzed by Bob cannot instantly determine the probability $P_\pm^A(\phi_A)$ of Alice's photon as Alice's and Bob analyser interferometers are situated at a space-like distance from each other. Bob's phase setting cannot instantly determine the measurement result $P_\pm^A(\phi_A)$ at Alice's site as no information about his measurement settings can be transmitted faster than the speed of light.

Under these conditions the CHSH theorem states that in a LHVT the normalized correlation function for the coincident detection between the detector pairs $(\pm_A, \pm_B)$, for two different settings $\phi_A, \phi_{A'}$ and $\phi_B, \phi_{B'}$ for Alice and Bob, is

$$|E(\phi_A, \phi_B)| = \frac{\int_\Lambda \rho(\lambda)d\lambda(|P_+^A(\phi_A, \lambda) - P_-^A(\phi_A, \lambda)) \cdot (P_+^B(\phi_B, \lambda) - P_-^B(\phi_B, \lambda)|)}{\int_\Lambda \rho(\lambda)d\lambda(|P_+^A(\phi_A, \lambda) + P_-^A(\phi_A, \lambda)) \cdot (P_+^B(\phi_B, \lambda) + P_-^B(\phi_B, \lambda)|)} =$$

$$\frac{|P_{+,+}^{A,B}(\phi_A, \phi_B) + P_{-,-}^{A,B}(\phi_A, \phi_B) - P_{+,-}^{A,B}(\phi_A, \phi_B) - P_{-,+}^{A,B}(\phi_A, \phi_B)|}{|P_{+,+}^{A,B}(\phi_A, \phi_B) + P_{-,-}^{A,B}(\phi_A, \phi_B) + P_{+,-}^{A,B}(\phi_A, \phi_B) + P_{-,+}^{A,B}(\phi_A, \phi_B)|} \quad (2.29)$$

such that $|P_+^B(\phi_B, \lambda) - P_-^B(\phi_B, \lambda)| \leq 1$ and $|P_+^A(\phi_A, \lambda) - P_-^A(\phi_A, \lambda)| \leq 1$ holds. With these definitions, the CHSH inequality can be formulated as

$$S(A, B; A', B') = |E(\phi_A, \phi_B) - E(\phi_A, \phi_{B'}) + E(\phi_{A'}, \phi_B) + E(\phi_{A'}, \phi_{B'})| \leq 2 \quad (2.30)$$

with $S(A, B; A', B')$ being the Bell parameter to be tested experimentally.

In order to verify if indeed a LHVT can account for the correlation results for energy-time entangled states as derived in sections (2.3)-(2.4.), let us now derive the expected results for the quantum mechanical description of the biphoton system. The state and the coincidence rate calculated in Eq.(2.13), have to be reformulated in order to account

for the detection of the photons at different detector pairs at different outputs $(\pm, \pm)$ of Bob's and Alice's analysis interferometers:

$$|\Psi\rangle_{A_\pm, B_\pm} = 1/\sqrt{2} \cdot (|0\rangle_{A_\pm}|0\rangle_{B_\pm} + kl e^{i\cdot(\phi_A + \phi_B)}|1\rangle_{A_\pm}|1\rangle_{B_\pm}). \qquad (2.31)$$

with the factors $k, l = \pm 1$. These factors can be explained by taking a closer look at the four possible possibilities for a coincident detection:

Photons taking the reflection output mode (in this case $(-, -)$) of the respective interferometer's second beamsplitter, acquire a relative phase shift of $e^{i\pi} = -1$. For the detector configuration $(-, -)$ this factor reads as $e^{i\pi} \cdot e^{i\pi} = (-1)^2 = k \cdot l$, while the detector configuration $(+, -)$ yields a factor of $e^{i\pi} \cdot 1 = (-1) \cdot 1 = k \cdot l$. Similar arguments hold for the two other coincidence probabilities.

The coincidence function can be reformulated as

$$P_{\pm, \pm}^{A,B}(\phi_A, \phi_B) = M \cdot (1 + ijV \cdot cos(\phi_A + \phi_B)) \qquad (2.32)$$

with $M = (\alpha + \beta)/2$ and the visibility $V = 2 \cdot \alpha\beta \cdot /(\alpha^2 + \beta^2)$.

The correlation function reads as $E(\phi_A, \phi_B) = V \cdot cos(\phi_A + \phi_B)$, such that a maximum $S = 2\sqrt{2}$ for the Bell parameter S can be found for the analyzer settings $\phi_A = -\pi/4; \phi_{A'} = \pi/2; \phi_B = 0$ and $\phi_{B'} = \pi/2$. Therefore, a quantum mechanical description of the correlation between both photons cannot be consistent with a LHVT, as this result is clearly above the bound $S = 2$ derived for this type of theory. In the same paper [41] cited before a more experimentally accessible CHSH inequality was formulated for entangled particles, for which it can be experimentally verified that the respective coincidence probabilities $P_{\pm, \pm}^{A,B}(\phi_A, \phi_B)$ don't depend on the respective local phase settings independently but only on their sum: $P_{\pm, \pm}^{A,B}(\phi_A, \phi_B) = P_{\pm, \pm}^{A,B}(|\phi_A + \phi_B|) = P_{\pm, \pm}^{A,B}(\Phi)$. If additionally it is verified that the single count rates $P_{\pm}^{A}(\phi_A)$ and $P_{\pm}^{B}(\phi_B)$ don't vary with a change in the analyzer settings ϕ_A and ϕ_B, the Bell inequality can be reformulated as

$$S = |3E(\Phi) - E(3\Phi)| < 2 \qquad (2.33)$$

corresponding to a value

$$S = 2\sqrt{2}V < 2 \Leftrightarrow V \geq 1/\sqrt{2} \approx 70,7\% \qquad (2.34)$$

when introducing the correlation function $E(\Phi)$ as calculated above.

It is to note that in this experiment only the correlation between a detector pair $P_{+,+}^{A,B}(\phi_A, \phi_B)$ was measured. Nevertheless the correlation function can still be extracted, starting from the assumption that the measured coincidence count rates are equivalent to a representative sample of the total count rates expected. This condition can be expressed as

$$\sum_{\pm,\pm} P_{\pm,\pm}^{A,B}(\phi_A, \phi_B) = 1, \tag{2.35}$$

i.e. the normalization to 1 of all calculated coincidence count rates, such that $M = \frac{1}{4}$ holds. The following relations between the different coincidence rates can be extracted from this condition:

$$P_{+,+}^{A,B} = 1/2 - P_{+,-}^{A,B}$$
$$P_{-,-}^{A,B} = 1/2 - P_{-,+}^{A,B} \tag{2.36}$$

Similarly, the coincidence rates calculated fulfil

$$P_{-,-}^{A,B} = P_{+,+}^{A,B} \tag{2.37}$$

according to Eq.(2.42).

The correlation function will therefore only depend on the measured coincidence count rate $P_{+,+}^{A,B}(\Phi)$

$$E(\Phi) = 4P_{+,+}^{A,B}(\phi_A, \phi_B) - 1 = V\cos(\Phi) \tag{2.38}$$

leading to the same bounds $V \geq 70,7\%$ for a Bell parameter $S \geq 2$ as given in Eq.(2.44). According to this derivation, the measurement of a two photon interference with a visibility V higher than $70,7\%$ will therefore be the direct experimental evidence that the two photon correlation cannot be described by a LHVT and that the two photons are energy-time entangled. Nevertheless, a conclusive test of a Bell inequality for this system can only be given when all the coincidence count rates between the different detectors are measured.

Additionally, the fact has to remain clear that the entangled state $|\Psi\rangle_{A_\pm, B_\pm}$ can only be discriminated by a postselection method in the coincidence time basis $t_A - t_B$, as the two other biphoton states $|0\rangle_{A_\pm}|1\rangle_{B_\pm}$ and $|1\rangle_{A_\pm}|0\rangle_{B_\pm}$ are distinguishable in the time basis. Therefore only two out of four biphoton states are indistinguishable with respect to each other. This means that the theoretical achievable visibility without the postselection method is limited to 50%, which is lower than the level of $70,7\%$ required to verify the entanglement of both photons.

A detailed discussion on this problem is given in [43], arguing that a local hidden variable model able to describe the correlations exists, even for the postselected state. In the same paper it is argued that a violation of a Bell inequality can still be warranted for the interferometer systems used for the analysis, as long as a fast random phase switch within the timescale $\Delta T/c$ is made. In this case the Bell parameter for a LHVT model is still smaller than for a quantum mechanical model. However, the Bell

inequality derived under these conditions would be violated only with an upper bound of $V > 96$. The results of this paper have to be revisited.

Nevertheless, the postselection problem could be circumvented experimentally in [44] by encoding the states additionally in the polarization basis such that effectively the photons are only prepared in indistinguishable biphoton states, requiring no further postselection. In this case a visibility high enough to violate a Bell inequality could be verified.

Bell inequality for two dimensional time-bin entanglement   As mentioned in section (2.4.), the stringent difference between energy-time and time-bin entanglement is that time-bin entanglement can be understood as the gated version of energy-time entanglement: The entangled photon pairs are emitted at discrete emission times, called time bins. A time bin entangled state

$$\Psi = e^{i \cdot (\phi_A + \phi_B)} |0\rangle_P |1\rangle_{A,B} + e^{i \cdot \phi_P} |1\rangle_P |0\rangle_{A,B} \qquad (2.39)$$

is defined. Analogically to energy-time entanglement, the entanglement of this state is verified as the two photon interference in the coincidence rate, too, with the only difference that the correlation probabilities between the different detector pairs $(\pm_A, \pm_B)$ have to be measured with respect to the pump photon emission time t_P.

This means that the same Bell inequality derived for energy-time entangled states applies for time bin entangled states as well. The measurement of the two photon interference visibility V by changing the phase ϕ_A and ϕ_B characterizes the quality of the entanglement.

2.6   Dispersion effects of the SPDC photons in optical fibres

Problem   In view of the practical implementation of energy-time and time-bin entangled states, dispersion effects in optical fibres and optical components have to be accounted for as they can lead to a decrease of the entanglement quality to be achieved. Before giving concrete details about the experimental setup, it will suffice to consider the experimental scheme for a time-bin experiment as depicted in Fig. (2.11):

A pulsed laser is coupled into an unbalanced free space interferometer introducing a path length difference of ΔL between the photons taking its short and long arm [6]. One output of the interferometer is used to produce degenerate SPDC photons on a BBO crystal. The emitted down-conversion photons are filtered by a filter with Gaussian frequency transmission centred at λ_0 and with a bandwidth of $\Delta \lambda$. Due to the finite

---

[6]The free space configuration has to be chosen as no commercial fused fibre couplers exist for the used UV wavelengths
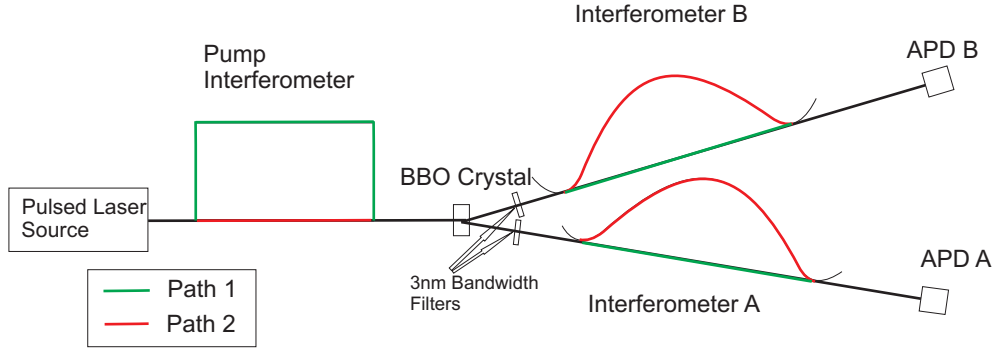
Figure 2.11: *Schematic presentation of a time-bin experiment employing one free space and two all-fibre interferometers. A pulsed pump laser emits pulses which are coupled into the unbalanced free space interferometer with a symmetric splitting ratio such that two pump pulses with a time delay ΔT exit the two outputs. Subsequently, one of the interferometer outputs is directed on a BBO crystal, such that approximately each 10^{-10}th pump photon is down-converted into a SPDC photon pair. Each SPDC photon of a pair is filtered by a 3nm bandwidth filter and is coupled into two distinct all-fibre interferometers with symmetric splitting ratios which introduce the same time delay as the pump interferometer. One output of each interferometer is coupled into an APD. The red and the green markings denote two different paths a pump photon and the corresponding down-converted photons can have taken in each of the interferometers of this configuration.*

bandwidth of the filter, non-degenerate photon pairs with a maximal wavelength difference of $\pm\Delta\lambda/2$ for the FWHM of the filter are coupled into two distinct all-fibre interferometers introducing the same time delay as the pump interferometer.

In difference to the free space interferometer, where the dispersion of the pump pulses are negligible due to their propagation through air, dispersion effects at the all-fibre interferometers represent a problem not to be underestimated: The photon wave packets will disperse because of the wavelength dependent group velocity in the silica medium of standard optical fibres. To illustrate the problem, consider the case when the signal and idler photons with wavelengths $\lambda_1^{s,i} = \lambda_0 + \Delta\lambda_\epsilon/2$ and $\lambda_2^{i,s} = \lambda_0 - \Delta\lambda_\epsilon/2$ with $\Delta\lambda_\epsilon < \Delta\lambda$, are coupled into their respective all-fibre interferometers. Each SPDC non-degenerate photon pair acquires a wavelength dependent time delay of $\Delta t(\Delta\lambda_\epsilon, \Delta L) = t_s(\lambda_0 + \Delta\lambda_\epsilon/2, \Delta L) - t_i(\lambda_0 - \Delta\lambda_\epsilon/2, \Delta L)$ with respect to its correlated photon as they are detected at the APDs. This time delay depends upon the path $\Delta L = \Delta T \cdot c$ the photons have traversed through the dispersive medium considered and upon their degree of non-degeneracy $\Delta\lambda_{epsilon}$.

The case of interest here is when both signal and idler SPDC photons either both take the path marked by the red or the green line in their respective all fibre interferometers. Then, for a photon pair with a frequency difference of $\Delta\lambda_\epsilon$ the time delay between two non-degenerate SPDC photon pairs due to dispersion will correspond to $\Delta t_L = \Delta t(\Delta\lambda_\epsilon, L_0 + \Delta L)$ and to $\Delta t_S = \Delta t(\Delta\lambda_\epsilon, L_0)$ respectively. Here Ł$_0$ denotes the path in the short arm of each interferometer. The amount of dispersive delay between

the SPDC photons is directly proportional to the path length traversed through the interferometers such that $\Delta t_L - \Delta t_S \neq 0$: The indistinguishability of non-degenerate photon pairs having taken different arms will be reduced at their respective detection at the APDs.

Calculation and Interpretation   An accurate description of these dispersion effects can be given by evaluating the joint time distribution of the two photon wave packets in dependency of the time delay $t_{\lambda_1} - t_{\lambda_2}$ between two non-degenerate photons of wavelength $\lambda_1 = \lambda_0 + \Delta\lambda_\epsilon/2$ and $\lambda_2 = \lambda_0 - \Delta\lambda_\epsilon/2$ with $\lambda_1 > \lambda_2$. For that, the formalism developed in more detail in [45] and [46] can be applied. Due to its accuracy, this description of the SPDC photon pairs as biphoton states will be referred to in the rest of this work.

The dispersion of the pump, signal and idler photon in the optical fibres ($M = Si$) and in the BBO crystal ($M = BBO$) can be characterized by the group velocity dispersion D_x^M of the photon wave packets, propagating with their corresponding group velocities v_x^M:

$$d_x^M = \frac{1}{v_x^M} = \frac{dk_x}{d\omega_{k_x}} = (n_{\lambda_x} - \lambda_x \frac{dn(\lambda_x)}{d\lambda_x})/c \qquad (2.40)$$

$$D_x^M = \frac{d^2 k_x}{d^2 \omega_{k_x}} = \frac{\lambda_x^3}{2\pi c^2} \frac{d^2 n(\lambda_x)}{d\lambda_x^2} \qquad (2.41)$$

The time distribution of the SPDC photon modes after being affected by dispersion can be described by the biphoton probability amplitudes $A_S(t_s, t_i)$ and $A_L(t_s, t_i)$. Following the paths marked in Fig. (2.10), these correspond to the amplitudes for the pump photon having traversed the long pump interferometer arm while both corresponding down-converted signal and idler photons have taken the short arm in their respective all-fibre interferometers (green) or vice versa (red).

Following the scheme outlined in detail in [46], the biphoton states are defined via the transition matrix between the SPDC photon state $|\Psi^{(2)}(0,t)\rangle$ into the vacuum state $|0\rangle$:

$$A_{S,L}(t_s, t_i) = \langle 0|E_s^+(0, t_0 + t_s)E_i^+(0, t_0 + t_i)|\Psi^{(2)}(0,t)\rangle, \qquad (2.42)$$

with $E_s^+(0, t_0 + t_s)$ and $E_i^+(0, t_0 + t_i)$ being the field operators of the signal and idler photon. The evolution of the SPDC photon state as a function of the Taylor expanded wave numbers $k_m(\omega_{k_m}) = k_m^0(\omega_m^0) + 1/v_m(\omega_{k_m} - \omega_m^0) + D_m/2(\omega_{k_m} - \omega_m^0)^2 + ...$ with $m = s, i$ will allow to describe the effect of dispersion in the optical fibres. This results in

$$
\begin{aligned}
A_{S,L}(t_s, t_i) \;=\;& C \int_{-L}^{0} dz \int_{-\infty}^{\infty} d\nu_p \int_{-\infty}^{\infty} d\nu_s \int_{-\infty}^{\infty} d\nu_i \\
&\cdot e_s(\omega_s^0) e_i(\omega_i^0) \Gamma_p^+(0, \nu_p) \cdot e^{-i(\omega_p^0 + \nu_p)(t_P + L_{L,S} \cdot c)} \cdot e^{-i(\omega_i^0 + \omega_s^0 + \nu_i + \nu_s) L_{S,L} \cdot c} \\
&\cdot e^{i(\nu_p / v_p^{BBO} - \nu_s / v_s^{BBO} - \nu_i / v_i^{BBO}) z} e^{i/2(D_p^{BBO} \nu_p^2 - D_s^{BBO} \nu_s^2 - D_i^{BBO} \nu_i^2) z} \\
&\cdot e^{i(k_s + k_i) L_{S,L}} \cdot e^{i(\nu_s / v_s^{Si} + \nu_i / v_i^{Si}) L_{S,L}} \cdot e^{i/2(D_s^{Si} \nu_s^2 + D_i^{Si} \nu_i^2) L_{S,L}} \\
&\cdot \delta(\nu_p - \nu_s - \nu_i) e^{i(\nu_s t_s + \nu_i t_i)} \sqrt{F_s(\nu_s)} \sqrt{F_i(\nu_i)}. \qquad (2.43)
\end{aligned}
$$

with $\Gamma_p^+(0, \nu_p)$ being the Fourier transform of the pump field envelope at $z = 0$ and $F_x(\nu_x) = e^{-2\nu_x^2 / \sigma_x^2}$ being the frequency transmission of the respective filters. C is a constant including the effective nonlinearity and the amplitudes $e_m(\omega_{k_m})$ of the signal and idler photon modes with wave vectors k_m and central frequencies ω_{k_m}, for $m = s, i$. The calculations consider the effect of pump, signal and idler wave dispersion at the BBO crystal, as denoted by the corresponding group velocities v_x^{BBO} and dispersion D_x^{BBO} with $x = p, s, i$. For small crystal lengths $L \propto 1mm$, the amount of dispersion at the BBO crystal is however negligible [46]. Only the group velocities and the dispersion at the silica material of the optical fibres characterized by $v_x^{Si} = 1/d_x^{Si}$ and D_x^{Si} over the corresponding path lengths $L_S = L_0$ and $L_L = L_0 + \Delta L$ will be of interest here.
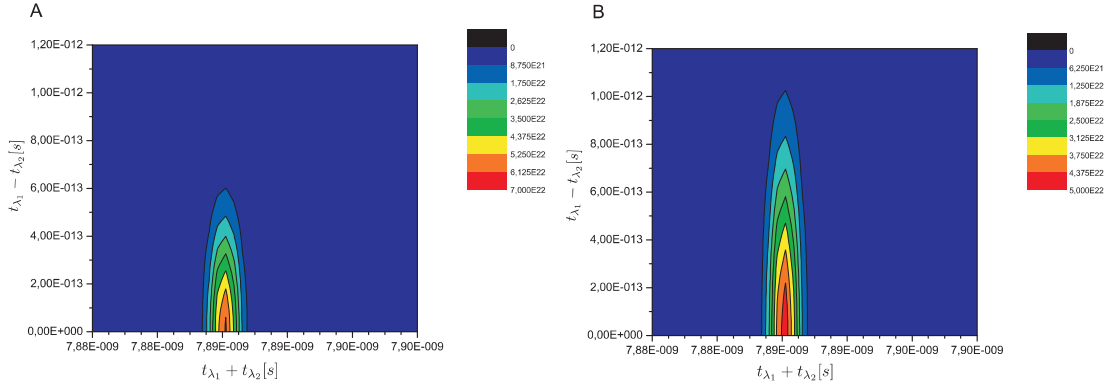
Figure 2.12: *Non-normalized biphoton amplitudes for both photons of a pair taking either the short (A) or the long (B) interferometer arm of an all-fibre interferometer as a function of the photon arrival time difference $t_{\lambda_1} - t_{\lambda_2} > 0$ and their sum $t_{\lambda_1} + t_{\lambda_2}$. The path length difference introduced is $\Delta L = 0,6m$, while the bandwidth of the SPDC photons, as defined by the bandwidth of the used filters, is chosen to be $\Delta\lambda = 3nm$. The overlap between the biphoton amplitudes in the $t_{\lambda_1} - t_{\lambda_2}$ time basis decreases due to dispersion: Each non-degenerate photon pair with wavelength $\lambda_1 = \lambda_0 + \delta\lambda_\epsilon/2$ and $\lambda_2 = \lambda_0 - \delta\lambda_\epsilon/2$ with $\delta\lambda_\epsilon < \delta\lambda = 3nm$ acquires a wavelength dependent time shift with respect to each other, directly proportional to the optical fibre path traversed. A high overlap of the pulsed SPDC photons in the $t_{\lambda_1} + t_{\lambda_2}$ time basis is ensured for both path configurations in Fig. (2.10) is exactly equal.*

In Fig (2.11) the non-normalized biphoton amplitudes for the short and the long arm are depicted for pulsed down-conversion photons acquiring a path length difference of $\Delta L = 0,6m$ and being filtered by a $\Delta\lambda = 3nm$ filter. The amplitudes are depicted

as a function of the relative and absolute time basis $t_{\lambda_1} - t_{\lambda_2} > 0$ and $t_{\lambda_1} + t_{\lambda_2}$, for SPDC photons with the different non-degenerate wavelengths λ_1 and λ_2, for $\lambda_1 < \lambda_2$. The distribution of the two-photon modes in the $t_{\lambda_1} - t_{\lambda_2} < 0$ axis is symmetric to the displayed distribution for $\lambda_1 > \lambda_2$. In this model, the polarization transformation of both photons traversing both interferometer configurations is the same, such that no polarization dependent time delay between both photons is simulated.

The $t_{\lambda_1} + t_{\lambda_2}$ time basis describes the absolute arrival time of the centre of the two photon wave packets with respect to the pump pulse arrival time. Nevertheless, as the interferometer path length difference is equal between all three interferometers in the setup, the absolute arrival time of the pump and SPDC photon pairs having traversed both paths in Fig.(2.10) is equal. This ensures a high indistinguishability in this time basis.

However, a clear mismatch between the distribution of the different SPDC photon frequency modes in the $t_{\lambda_1} - t_{\lambda_2}$ time basis can be observed, due to the wavelength dependent dispersion in the long and in the short arm of the all-fibre interferometers. Each photon mode acquires a different wavelength dependent time delay $t_{\lambda_1} - t_{\lambda_2} > 0$. The maximal time delay can be evaluated to be

$$\Delta t_{S,L}^{max} = t_{\lambda_0 + \Delta\lambda/2} - t_{\lambda_0 - \Delta\lambda/2} = L_{S,L} \cdot \left(\frac{1}{v_{\lambda_0 + \Delta\lambda/2}} - \frac{1}{v_{\lambda_0 - \Delta\lambda/2}} \right), \qquad (2.44)$$

with the path length $L_S = L_0$ and $L_L = L_0 + \Delta L$ for the short and long interferometer arm respectively. For $\lambda_0 = 805nm$ and $\Delta\lambda = 3nm$ the respective group velocities read as $v_{\lambda_0 + \Delta\lambda/2} = 2,03793 \cdot 10^8 m/s$ and $v_{\lambda_0 - \Delta\lambda/2} = 2,03779 \cdot 10^8 m/s$.

For a path of $L_0 = 0,6m$ and a path difference of $\Delta L = 0,6m$, this results in a maximal wavelength dependent time delay of $|\Delta t_S^{max}| = 0,1951ps$ and of $|\Delta t_L^{max}| = 0,3902ps$ between the respective photon pairs with wavelengths $\lambda_1 = \lambda_0 + \Delta\lambda/2$ and $\lambda_2 = \lambda_0 - \Delta\lambda/2$. The maximal shift in the FWHM distribution of both biphoton amplitudes is evaluated to be $\Delta t_L^{max} - \Delta t_S^{max} = 195fs < t_c \approx 720fs$, only slightly smaller than the coherence time t_c of the photon wave packets. This time delay refers only to the photons with a wavelength limited by the FWHM of the filters. For photons at a lower transmission level of the filters, this delay is even higher.

We note that the maximal SPDC photon's path differences in a multiple arm interferometer configuration have to be chosen to add to a total of $\Delta L = 4,20m$, a path length difference 7 times higher than the computed here, as will be displayed in section (3.1.3). For this value, the reduction in the overlap between both biphoton states distributions would increase and the maximal time shift between two correlated biphoton would even be higher than the coherence length of the photons. A loss of coherence and a reduction in the entanglement quality between two biphoton wave packets having traversed two different paths in the interferometer has to be expected as a function of the path length difference ΔL of the all-fibre interferometers and the degree of non-degeneracy

$\Delta\lambda_\epsilon$ of the SPDC photons. Therefore the all-fibre interferometer configuration should be avoided in this experiment.

Proposed and chosen solutions   The difference to experiments where all-fibre interferometers could be successfully employed [16],[15] is given by the pump laser wavelength and by the optical fibre types used. It is advantageous to choose pump wavelengths for which SPDC photon pairs can be produced in the telecom wavelength regime and to implement commercial optical fibre components with a zero dispersion wavelength corresponding to the central wavelength of the degenerate photon wave packets. Additionally, the magnitude of the dispersion coefficients of the non-degenerate signal and idler photon can be chosen to be equal up to a high accuracy: $|D_s^{Si}| = |D_i^{Si}|$.
Under these conditions one can take advantage of the effect of dispersion cancellation, which is based on the entangled nature of biphoton states. As described by J.D. Franson in [47] the dispersion $D_s^{Si}\nu_s^2$ and $D_i^{Si}\nu_i^2$ in Eq.(2.45.) for each entangled photon pair with wavelength $\lambda_s = \lambda_0 + \Delta\lambda_\epsilon$ and $\lambda_i = \lambda_0 - \Delta\lambda_\epsilon$ is of opposite sign

$$D_s^{Si}\nu_s^2 = -D_i^{Si}\nu_i^2, \tag{2.45}$$

as long as λ_0 corresponds to the zero dispersion wavelength of the silica medium. This warrants that for the entangled biphoton state both dispersion components will cancel each other for general ϵ.
This presents an interesting alternative based on the observation in Fig. 2.12 that the distinguishability of both biphoton amplitudes for both correlated photons taking either the long or the short arm in their respective all fibre interferometers increases with the path length difference introduced. Therefore, an experimental alternative would be the integration of Photonic Crystal Fibres (PCFs) into the interferometers, offering the characteristic that the zero dispersion wavelength for the fibre material can be shifted down to IR wavelengths, such as to make it correspond with the degeneracy wavelength of the photon wave packets. As long as this special fibre is introduced instead of the standard fibres accounting for the path length difference $\Delta L = \Delta T/c$, the dispersion cancels for both biphoton probability amplitudes as described above. However this approach would be difficult to implement experimentally, as the accuracy required in the zero dispersion wavelength of commercially available PCFs couldn't be warranted [48]. Another disadvantage lies in the very difficult handling of the PCFs.
As will be described in detail in the experimental section, the solution to this problem was given by substituting the standard fibres accounting for the path length difference ΔL by a free space path, i.e. the amount of dispersive silica material the photons traverse for the long and the short path is equal, such that effectively both biphoton states remain indistinguishable.

Chapter 3

Experimental Implementation

This chapter deals with the practical implementation of energy-time and time-bin entanglement. The experimental setup chosen for this purpose is described in detail. Beginning with the SPDC photon source, special focus will be given on the interferometer system required to analyze the entangled state.
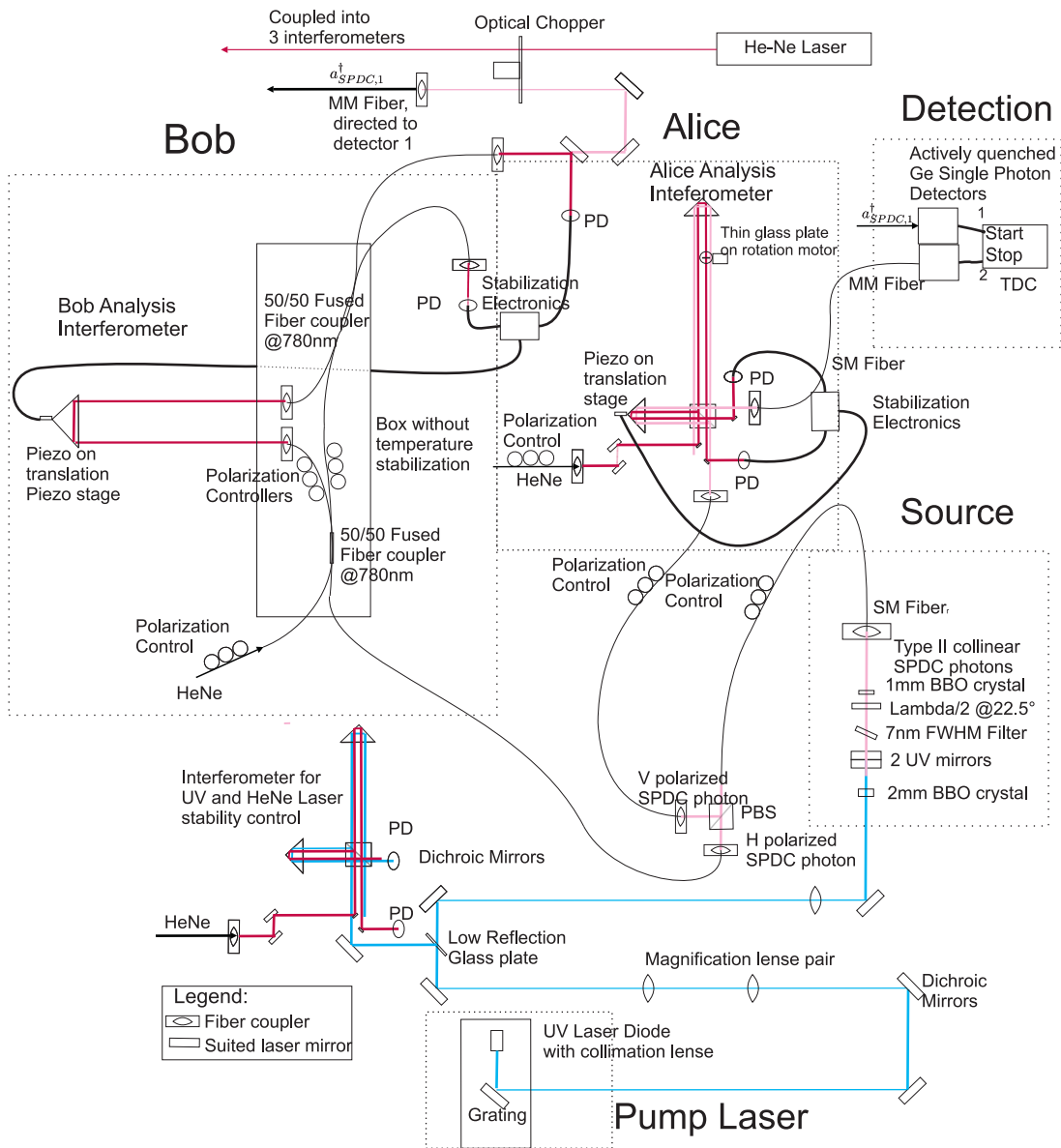
3.1 Presentation of the experimental setup

Here, starting from the schematic presentation and description of the experimental setup in Fig. (3.1), the advantages and disadvantages of the implemented components with respect to the achievement of higher dimensional entanglement will be discussed, which is the aim for further experiments in the future.

3.1.1 Blue Laser Diode and further optical components

The choice of a laser diode in the wavelength regime of $400nm$ has been met on the following criteria: The experiment is not planned to be suited for the distribution of entangled SPDC photons over large distances, such that the implementation of commercial optical fibres in the telecom regime $(1, 3 - 1, 5\mu m)$ which has proven to be very fruitful for this purpose [16], will not be considered.
As the scheme used to prepare the photons in higher dimensional states is afflicted by a relatively high loss rate at the interferometer sets, a high efficiency and reduced noise rates of the single photon detectors would be favourable. Silicon avalanche photodiodes (APDs) holding to these criteria exist for the visible wavelength regime $\lambda = 600 - 900nm$ offering efficiencies of up to 70% at the peak wavelength, much higher than for InGaAs APDs suited for telecom wavelengths. Therefore, a blue laser diode with a free running wavelength of 402,5nm (Nichia, NDHV310APC, 60mW of maximal output power), suited for creating degenerate SPDC photon pairs at 805nm, is implemented. At this wavelength regime the implemented actively quenched Si APDs offer specified detec-

Figure 3.1: *Scheme of the experimental setup for two dimensional energy-time entanglement. The source for the SPDC photons is a grating stabilized blue CW laser diode, whose stability can be monitored with the help of an additional free space interferometer. The pump beam is directed onto the setup allowing the creation of Type II collinear SPDC photon pairs with respective H and V polarization. These can be separated by a PBS and redirected onto the two spatially separated interferometers, of the Free Space and Hybrid Michelson interferometer type, respectively. One output of each interferometer is coupled into an APD and the coincidence rate between both detectors measured with a Time to Digital Converter (TDC). For the interferometer stabilization a HeNe laser is coupled into one input of each interferometer and their output signals compared by Proportional-Integral (P-I) regulation electronics. The electronic circuit of this device is in a closed loop with a piezo actuator correcting for the fluctuations of each interferometer's path length difference.*

tion efficiencies of up to 60.5%. The laser diode is mounted inside a collimation tube with suited collimating optics, while a Peltier element placed directly under the diode mounting permits to continuously stabilize it to room temperature. The polarization of the emitted laser beam is oriented on the vertical axis.

As described in the theoretical section (2.3) one of the requirements for observing energy-time entanglement for SPDC correlated photons is that the uncertainty in their creation time τ_1, defined by the pump laser coherence time, is much higher than their time delay ΔT acquired at the respective interferometers.

In order to be able to distinguish between photon pairs having taken different paths through the interferometer the time delay ΔT has to chosen to be larger than the detector's timing resolution Δt_D. For the actively quenched Si detectors used in this experiment, a $\Delta t_D \geq 2ns$ FWHM timing resolution could be observed.

Therefore the time delay ΔT introduced by the analysis interferometers has to satisfy the condition $\Delta t_D < 2ns < \Delta T << \tau_1$. However, this condition cannot be warranted generally for free running laser diodes as they offer coherence times only in the range of $\tau_{1,FR} \approx 1ns$.

However, there exists a simple solution, based on the application of an holographic grating (line density of 3600/mm) as an external cavity mirror (See Fig. 3.1). This method is called grating stabilization and is described in detail in [49]. Additional details on its function and on measurements on the achieved enhancement in the coherence time will be given in section (3.1.1).

Collimation Optics Further optical elements are introduced into the path of the blue laser beam: In order to reduce the background light in a wavelength range 500-900nm emitted by the blue laser diode, which could falsify the count rates of the SPDC photons, the blue beam is reflected 4 times by dichroic UV-mirrors with a designed high reflection coating for 390nm and low transmission for 780nm, still suited for the wavelengths of 402,5nm for the pump laser and of 805nm for the down-converted photons. This ensures that with each reflection the background light intensity at the wavelength regime of the down-conversion photons reduces.

Additional optical components, like a magnifying pair of lenses ($f_1 = 150mm$ and $f_2 = 200mm$), with one of them mounted on a translation stage, were introduced in order to correct for the divergence of the pump beam and to increase the beam waist w_0. [1]

---

[1] The improvement of the spatial mode collimation and the enhancement of the Raleigh length $z_R = \pi w_0^2 / \lambda$ up to the interferometer path length difference would have been necessary for the time-bin experiment such as to provide a better mode overlap at the preparation interferometer. However this experiment wasn't performed in the actual work.

Frequency stability control A free space interferometer was available, which enabled to monitor the frequency stability of the grating stabilized blue laser diode during the experimental runtime (See section (4.1.4):

A thin glass plate was used for splitting up a small component of the blue laser beam and coupling it into one input mode of this interferometer. Its path length difference was chosen to be larger than the free running laser diode's coherence length, such that an increase in the bandwidth and the corresponding reduction in its coherence length would be characterized by a large decrease in the interference visibility observed at one output of the interferometer while scanning its path length difference with a piezo. Further details are given in section (4.1.4).

The monitoring of the laser diode's frequency stability is crucial for the experiment, in order to ensure the condition $\Delta T << \tau_1$ for the blue laser's coherence time to hold over the whole measurement time.

### 3.1.2   SPDC Source

After the collimation optics, the blue laser diode beam is directed onto a 2mm thick BBO ($\beta - BaB_2O_4$)-crystal cut at an angle $\Theta = 42,13°$ for producing Type II SPDC photon pairs. In order to achieve a high SPDC photon pair rate, several criteria with respect to the spatial mode of the blue laser beam have to be met:

The spatial mode of the laser diode has to be as close to a Gaussian form as possible. This maximizes the overlap between the intensity distribution of the SPDC photons and the transversal mode distribution guided in single mode fibre, into which the SPDC photons are coupled. In this setup, the quality of the blue laser mode guided through the setup in Fig.(3.1) was sufficiently good such that only a simple iris was necessary for achieving a mode quality as depicted in Fig. (3.2.).

The blue laser beam is focused onto the BBO crystal with a f=200mm lens, ensuring that the waist of the beam lies at the BBO's crystal position. The waist of the focused pump beam is chosen such that the divergence of the emission modes matches the divergence of the modes collected by the fibre with a core diameter of $2,9\mu m$. The fibre coupler with a $f = 11mm$ aspheric lens is mounted on two translation stages allowing its translation along the horizontal and the vertical axis and the adjustment of the horizontal and vertical tilting in the coupling direction is possible. In order to minimize the divergence of the pump photons, effectively resulting in a higher bandwidth of the phase matched SPDC photons (See section 2.1.), a waist radius not less than $50\mu m$ has to be warranted for. In this experiment a waist radius of $57,4\mu m$ was achieved (Fig. 3.2.). For these parameters, an ideal separation of 165mm between the waist of the beam and the aspheric lens focusing the photons into the core of the fibre could be calculated.

The BBO crystal was tilted by about 2° with respect to the vertical axis in order to en-
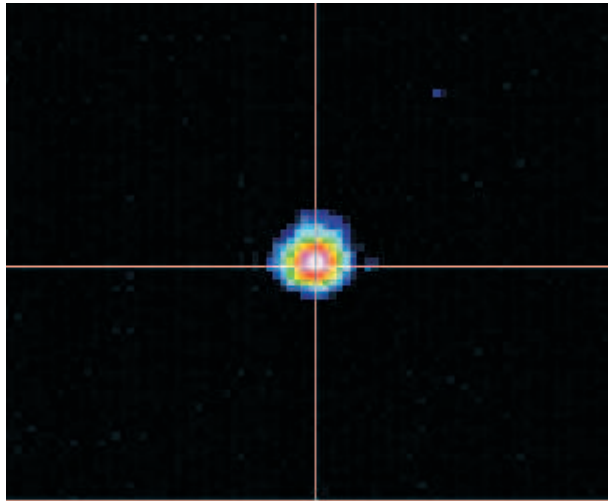
Figure 3.2: *Beam waist at the position of the BBO crystal. The beam waist radius amounts to*
57, 4μm.

sure the collinearity of the SPDC photon pair emission cones. The vertical polarization
of the laser beam ensures it to be extraordinarily polarized with respect to the crystal's
optical axis, as required for Type II SPDC. Therefore H and V polarized SPDC photon
pairs will be emitted. In order to prevent photons of the blue laser beam of being cou-
pled too into the SM fibre, too, two mirrors with suited HR coating for 400nm reflected
back the laser beam. An additional interference filter with a maximum transmission of
81,1% at the central wavelength of 807,92nm and with a 6nm FWHM was introduced.
However, the tilting of the filter in the horizontal plane shifts the central transmission
wavelength down to the desired wavelength of 805nm, such as to permit preferably the
transmission of the degenerate SPDC photon pairs created in this scheme.

In order to ensure the deterministic discrimination between H and V polarized photons
of a SPDC photon pair the output of the SM fibre guiding the SPDC photons is di-
rected onto a PBS. In order to maximize the discrimination, this component is slightly
tilted in the vertical direction such that the polarization of the reflected photons is
parallel to the V polarized photons emitted at the crystal. With an additional fibre
controller on the input fibre, it can be ensured that the rotation in the polarization
introduced by the guiding fibres is compensated. Finally, the H and V outputs of the
PBS are coupled onto separate SM fibres directed onto distinct interferometers. The
coupling of the SPDC photons into the single mode fibre is adjusted by monitoring the
coincidence rate between the detection count rates of the correlated SPDC photons in
both detectors. The coincidences can be monitored with the help of a coincidence card
with a suited coincidence time interval $\approx 1.3ns$ mounted on a computer.

Additionally, it has to be considered that the tilting of the interference filter necessary
to couple preferably degenerate photon pairs will introduce a vertical displacement into

the SPDC photon's path, such that the coupling adjustment will be lost. It helps to leave the interference filter without tilting in first place, yielding a reduced coincidence rate, and then to gradually readjust the tilting together with the coupler's horizontal position such as to maximize the coincidence rate again. The optimal tilting of the filter is achieved when maximal coincidence rates are measured.

The longitudinal and transversal walk-off described in (2.2.1) is compensated for with a $\lambda/2$ adjusted such as to ensure the rotation by $90°$ of the polarizations of both SPDC photons respectively and by an additional BBO crystal with the same cutting characteristics as the first one but only with a thickness of 1mm. The optimal compensation will only be ensured by adjusting the tilting of this BBO crystal with respect to $\vec{k}_p$ such as to be exactly the same as for the first crystal. This is easily done by inserting this BBO crystal instead of the first one and adjusting its tilting until the coincidence count rates are optimized for this crystal, too.

At 9mW of optical power, maximal coincidence rates of $1875/s$ with respect to an average single count rate of $10.500/s$ could be measured, yielding a coincidence ratio of $17,85\%$ and down conversion efficiencies of $208/(s \cdot mW)$. However, in the final experimental setup a readjustment of the SPDC setup proved to be necessary, as the grating stabilization method applied on the diode wasn't sufficiently optimized such as to offer its required frequency stability. With a readjustment of the grating, the spatial mode would have changed. A necessary readjustment yielded a lower single to coincidence count ratio of $13,5\%$.

3.1.3   Considered and implemented interferometer types

As discussed in the introductory chapter, energy-time entanglement proposes several advantages with respect to entanglement in the polarization basis. However the practical implementation is difficult due to the high sensibility of the interferometer's relative phase to mechanical instabilities and to frequency instabilities in the lasers used (See section 3.1.3.2). This work tries to achieve higher dimensional entanglement requiring the use of multi-arm interferometers, with each arm introducing twice the time delay as the previous one. With a minimum path length difference of $\Delta L = \Delta T/c = 0,60m$ for the first interferometer arm, determined by the detectors timing resolution $\Delta t_D \geq 2ns$, the path length of the following arms would amount to $\Delta L_2 = 1,20m$ and $\Delta L_3 = 2,40m$ and so on, respectively.

The configuration with three interferometer arms, encoding the biphoton state in an eight dimensional Hilbert space, already amounts to a maximal path length difference of 4,20m, between a SPDC photon having taken the shortest arm and the correlated photon taking the longest one, respectively. The stabilization of path length differences of this magnitude offers a challenge not trivially to be solved.

As long as no detectors offering a better timing resolution are used, enabling to reduce

the path length difference required, adding further interferometer arms, such as to encode the photon pairs in even higher dimensional entangled states, is difficult.

Free Space interferometer The free space interferometer consists of a beamsplitter with a design wavelength of 780nm offering an optimal $(48.9 \pm 2/51.1 \pm 2)$ splitting ratio as measured for an H polarized laser diode at 812nm. The output of the SM fibre guiding the V SPDC photons is directed into one input of the BS such that the spatial mode is split up into two separate modes.

Both SPDC photon modes are redirected onto the BS with the help of the two retro-reflection prisms with a 90° angle accuracy better than $5''$ [2]. This high accuracy is an important advantage when adjusting the mode overlap between both retro-reflected beams at the beam splitter. The quality of the mode overlap achieved, which characterizes the degree of indistinguishability between both modes, is studied in section (4.1.2). In order to change the path length difference, one retro-reflection prism is mounted on a micro-translation stage with its adjustment screw driven by a step motor [3]. A change of the path length difference on a nm resolution is achieved by the additional piezo actuator [4] installed in the same translation stage [5].

As the analysis of the entangled state is undertaken by a change in the relative phase each photon acquires on their path through the interferometer, the stability of this phase setting has to be ensured. Mechanical vibrations of the optical table, fluctuations in the refractive index along the interferometer path as well as the bending of the optical table are all factors which can contribute to a random change in the phase setting.

For this reason a stabilization laser, in this case a HeNe laser (632.8nm), is implemented such that its beam follows a path parallel on the same horizontal plane as for the SPDC photon's path in the interferometer. Even if the splitting ratio at the BS is highly asymmetric at this wavelength regime, interference could be observed in both output modes of the BS. A voltage proportional to the intensity at both output modes, as measured by two different photodiodes the output modes are directed to, is subtracted and the difference compared to a voltage value of 0V by an Proportional-Integral (P-I) regulator. The P-I regulated output signal of this electronic device is proportional to the deviation from the zero voltage difference level. As long as it is applied at the piezo actuator after being amplified, the path length difference in the interferometer can be stabilized on a nm scale. This warrants that as long as a closed regulation loop between the photodiode voltage differences and the voltage applied at the piezo is ensured, all

---

[2]Bernhard Halle GmBH Model UPS1.20
[3]OWIS DMT-40
[4]PhysikInstrumente P830.10
[5]OWIS MT45

mechanical instabilities in the interferometer will be compensated for by a readjustment in the path length difference by the piezo (See section 4.1.2, and for a detailed description of the electronics: [50]).

In order to be able to change the relative phase setting in the interferometer, a thin glass plate with a thickness of 1mm mounted on a rotation motor [6] was introduced into the path of the HeNe beam in the longest interferometer arm. A rotation of the glass plate will allow to shift the phase of the HeNe laser beam in the interferometer. The voltage difference measured between both output photodiodes is therefore shifted from the zero voltage value adjusted by the stabilization electronics. Due to the closed control loop, the piezo is driven as long as the voltage difference reaches 0V again, such that effectively the piezo will have introduced the desired change in the phase of the SPDC photons guided through the same interferometer.

Hybrid interferometer The designation "hybrid" for the second interferometer type derives from its composition of 2 fused 2x2 fibre couplers offering a (50/50) splitting ratio for 780nm [7] and an additional free space path. The fibre coupler pigtail lengths are equal up to a length difference $\leq 2cm$. Both fused fibre couplers are installed in an aluminium box in order to limit the variation of the optical path length through the fibres with temperature fluctuations.

The H polarized SPDC photons are coupled into one input arm of the fibre couplers such as to be split up with a ratio of $(41 \pm 2/59 \pm 2)$. One output is directly connected to the input of a second fused fibre coupler, while the SPDC photons at the other output are extracted and collimated by an aspheric lens in order to be transmitted over a free space path outside the box. With the help of a retro-reflection prism the beam can be redirected back into a fibre coupler in the box, such as to be focused into one input of the second fused fibre coupler. This arrangement ensures that both modes overlap at the fused beam splitter with a splitting ratio of $(44 \pm 2/56 \pm 2)$. Due to the fact that the fibre pigtails have only small length differences $\leq 2cm$, the path length difference ΔL the photons acquire in the interferometer is given in its majority by its free space component. The path length difference of the interferometer can be changed by the micro-translation stage with attached piezoactuator the retro-reflection prism is mounted on.

As the mode overlap at the second fused fibre coupler is free of any mismatch in the spatial mode, the spatial indistinguishability of both modes is minimal. However, due to the birefringent nature of the fibres [8], the polarization transformation in any of the

---

[6]OWIS SM40

[7]Thomas&Betts

[8]Due to the manufacturing process of fused fibre couplers, even the compensating effect of polarization maintaining fibres would be lost

two fibres is arbitrary. Therefore this has to be readjusted for such that both fibre paths introduce the same unitary transformation to the polarization state of the photons. Nevertheless, the maximal indistinguishability between both modes requires the adjustment on two different polarizations rotated by 45° with respect to each other, such as to ensure that at their overlap both modes share exactly the same sign in their polarization transformation. This can be adjusted with the help of two fibre polarization controllers ("bat-ears") along both fibre paths of the photons.

Finally both output modes of the interferometer are collimated again and transmitted over a free space path.

For the same reasons illustrated above for the free space interferometer, a stabilization laser is coupled into the input fibre of the first fused fibre coupler, ensuring it to be guided along the same path in the interferometer as for the SPDC photons. Of course, at this wavelength regime of 632.8nm, well below the design wavelength of 780nm, the single mode operation of the fibre couplers had to be ensured. For this wavelength a relatively bad splitting ratio of $(78.9 \pm 2/18.1 \pm 2)$ and of $(17.7 \pm 2/82.3 \pm 2)$ at the two fused fibre couplers was observed. However, the interference visibilities achieved were still higher than 40% in both output modes, sufficient for applying the same stabilization method described above. A fibre polarization controller at the input fibre for this laser allows to improve the interference visibility at both outputs, as the splitting ratios in the fused fibre couplers are highly polarization dependent for this wavelength. As for the Hybrid interferometer the HeNe laser and the SPDC photons are coupled the same fused fibre coupler, their spatial modes share essentially the same distribution. For the discrimination between both modes a dichroic mirror with specified high reflection at 478nm and high transmission at 780 was available and was introduced on the path of one output mode of the interferometer. Only reduced transmission losses were observed for the SPDC photons at this mirror, while for 632.8nm it offered a sufficiently good reflection.

The reflected HeNe beam is directed onto one photodiode, while the 805nm photons transmitted are coupled into a Multimode (MM) fibre guiding the photons to one of the detectors. The intensity of the HeNe laser beam at the second output mode of the interferometer is directly measured by a second photodiode. Again the stabilization of the interferometer is undertaken with the help of P-I regulation electronics driven by the photodiode's voltage difference.

It is to note that the remaining photon flux of the HeNe laser still being transmitted through the dichroic mirror is orders of magnitude higher than the SPDC photon flux, such that even a combination of several long-pass filters of the type RG645 and RG715 and a 7nm FWHM interference filter at 805nm is not sufficient to suppress it. Even if a suited dichroic mirror with high reflection at 632.8nm was used, the remaining transmitted HeNe laser could still influence the measurement results.

A higher suppression of the HeNe photon flux could be obtained by introducing an optical chopper into the experimental arrangement as depicted in Fig. 3.1.:

The main HeNe beam is blocked alternately by the chopper blades before being coupled into the interferometers such that effectively a modulation in the HeNe intensity with a frequency of up to $f = 1kHz$ is achieved. In parallel, one output mode of the interferometer directed onto the MM fibre coupler is guided through the optical chopper blades too, such that the blocking of the SPDC photons is alternating with the blocking of the HeNe laser beam. This ensures that only for a time interval of $1ms = \frac{1}{1kHz}$ where the HeNe laser is not guided through the Hybrid interferometer, the count rates of the SPDC photons are measured on the detector, and vice versa. Effectively, this corresponds to the continuous switching between a stabilization time and a detection time, such that both share 50% of the total measurement time. Therefore a reduction of the coincidence rate of 50% has to be accounted for.

In contrast, using asymmetric chopper blades would allow to switch between the measurement and the stabilization time by an unbalanced ratio, for example 80% to 20% respectively.

Additionally, this method offers the possibility to avoid the detection of wrong counts due to Raman scattering processes, i.e. the inelastic scattering of HeNe laser photons on the atoms of the silica medium accompanied by the emission of Stokes and Anti-Stokes photons with a frequency $\nu \neq \nu_{HeNe}$. As the HeNe beam is coupled into the fibres with an average power in the range $P \propto 100 - 500\mu W$, there exists a finite probability that photons in the 800nm regime are emitted due to these processes. With the scheme presented here the HeNe laser isn't guided through the fibres during the measurement time and the problem of inelastic scattering can be circumvented.

It is to note that due to the vibrations the motor in the optical chopper could transmit onto the optical table the interferometer's phase can suffer additional fluctuations. Therefore the chopper was attached to a support above the optical table, such as to ensure that all contact with the optical table is avoided.

In order to avoid a reduction of the stabilization quality, a modulation rate higher than the inverse of the response time $\frac{1}{\tau_R} \approx \frac{1}{0.1ms} = 100Hz$ of the piezo actuators has to be chosen. The modulation with a frequency $f = 1kHz$ satisfied this condition.

3.1.3.1 Advantages and disadvantages of the different interferometer types

Next, the advantages and disadvantages of the two interferometer types will be discussed in view of achieving higher dimensional entanglement. In addition, these two types will be compared to a third interferometer type composed entirely of fibre optical material not implemented in this work, but which offer many advantages as already demonstrated in [15]. In difference to the hybrid interferometer described before, this

type is composed of two 2x2 fused fibre couplers with a 50/50 splitting ratio whose pigtail lengths are not equalized. The two output fibre pigtails of one fibre coupler are directly connected to the two input pigtails of the second one, such that the path length difference between the two couplers differs by $\Delta L_{Si} = \frac{\Delta T}{n_{Si}c}$ where n_{Si} is the refractive index of the fibre's silica material at the design wavelength. In contrast, for the hybrid interferometer it is defined entirely by its free space path $\frac{\Delta T}{c}$.

1. Free Space Michelson interferometer
   Advantages: ´

   - The stability and robustness of this interferometer type could be shown even for high path length differences $\Delta L \geq 1m$.

   Disadvantages:

   - Due to its free space nature, a perfect mode overlap of both retro-reflected beams at the beamsplitter is difficult to implement and offers the most important limit for achieving a high interference visibility. A perfect collimation of the mode over the whole range of the interferometer would be necessary, requiring the refocusing of the beam into the beamsplitters with additional pairs of lenses. This problem is enhanced when several interferometer arms are to be appended in series as required for achieving higher dimensional entanglement. For three arms a good collimation over a range of $4, 20m$ between the shortest and the longest interferometer path would be necessary.

   - Connecting several interferometer arms in series would present the additional problem that a small drift in the mode of the first interferometer will directly affect the mode overlap in the subsequent interferometers. Thermal drifts in the optical components or the bending of the optical table are the major factors contributing to this problem. Variations in the interference visibility are therefore difficult to control. A very time intensive adjustment would have to be done in order to compensate this detrimental effect.

   - As could be observed in previous experimental realizations of interferometers in the group [51], a reduction in the long term phase stability of the interferometer can be expected due to the bending of the optical table and the corresponding tilt in the optical components used in the interferometer. This is a problem which gets enhanced when the stabilization laser isn't guided at exactly the same height as the SPDC photons path such that both modes acquire a different phase shift with the tilting of the affected optical component. In this case the bending of the table would introduce a different

phase drift between both spatial modes, such that once the path of the HeNe laser is readjusted with the stabilization scheme mentioned before, it would erroneously change the SPDC photon's phase setting, too.

- A problem not to be underestimated is the rotation in polarization at the optical components implemented. A high rotation in the polarization could be observed at the output for the input beam being polarized at $+45°$, being possibly due to the birefringent nature of the dielectric layer of the BS. This effect will be detrimental for ensuring that both modes share exactly the same polarization state at their overlap at the beamsplitter. A compensation for this effect can be undertaken with the help of $\lambda/2$ waveplates or birefringent quartz plates [50].

2. All-Fibre interferometer
   Advantages:

   - The most stringent advantage of this interferometer is the good spatial overlap achieved between two input modes at the fused fibre beam splitter, ensuring both modes to be perfectly indistinguishable in their spatial distribution.

   - No active stabilization of the interferometer against mechanical vibrations is required as the optical fibres used are less sensible to them. The active stabilization on the temperature of the optical fibres is required as the fibres are subject to length differences with a change in the room temperature.

   Disadvantages:

   - The handling of the fibres of this interferometer is difficult. As the path length differences of the interferometers have to be equalized up to the SPDC photon's coherence length $l_c \propto 100\mu m$, a high precision when cutting and connecting the fibres has to be achieved. Stretching the fibres to the desired path length can overstretch them.

   - As already discussed in section (2.6) dispersion effects at the optical fibres will reduce the attainable indistinguishability of the SPDC biphoton states in dependency of the path length traversed and the bandwidth $\Delta\lambda$ of the photons. The two possible biphoton evolutions, i.e., both correlated photons taking different arms in their respective all fibre interferometers, will not be perfectly indistinguishable in the coincidence time basis. This limits the visibility of the two photon interference between both biphoton states.

   - The arbitrary transformations in the polarization state of the photons introduced by the optical fibres need to be compensated for. This is achieved with the help of fibre polarization controllers such that the polarization states are

adjusted to be the same for both overlapping modes. As the polarization state in the fibres will change with the fluctuations in the ambient temperature, this adjustment will be worse after some weeks.

3. Fibre and Free space (Hybrid) interferometer
   Advantages:

   - Analogically to the all-fibre interferometer the mode overlap at the fused fibre couplers ensures the maximal indistinguishability of the overlapping modes in their spatial distribution.

   - For this interferometer type successively appended interferometer arms aren't as interdependent in their respective mode overlap as for the free space interferometer, as there is no spatial mismatch between the overlapping modes in each interferometer arm.

   - As discussed in section (2.6) the detrimental dispersion effects are reduced for this kind of interferometer. Dispersion effects are only due to the small mismatch in the length of the fused fibre coupler pigtails $\leq 2cm$ and due to the dispersion of the photon wave packets at the retro-reflection prism implemented. However, these small effects can easily be compensated by cutting the relative length difference of the fibre pigtails between the long and the short arm to the required length.

   - For this interferometer type the stabilization laser mode is guided though exactly the same path as for the SPDC photon modes. This increases its phase stability with respect to the free space configuration, where detrimental effects such as the bending of the optical table can cause additional phase shifts.

   - The rotation in the polarization at the retro-reflection prism can easily be compensated for with the implemented fibre polarization controllers.

   - In difference to the all fibre configuration, a change in the path length difference in order to match it with another interferometer is easily realized, as this change can easily be implemented on the free space path.

   Disadvantages:

   - An active stabilization scheme as implemented for the free space interferometer is required for compensating the mechanical instabilities. Additionally a temperature stabilization of the fibres would be desirable in order to minimize their contribution to a phase drift. However, as the fibre pigtail lengths of both fused fibre couplers are nearly equalized, this effect is reduced, as the

phase drifts in both interferometer arms would be synchronous. As demonstrated in section (4.1.2), this interferometer type requires only an active stabilization scheme in order to correct for the phase fluctuations.

- A not so simple problem is given when connecting several interferometer arms. Each interferometer arm is subject to its specific mechanical instabilities such that they have to be stabilized independently from each other. Therefore, the stabilization laser has to be extracted at a position on the path of the subsequent interferometer arm, while the stabilization laser for the subsequent arm has to be introduced in this interferometer arm, too. In parallel it has to be ensured that the SPDC photons don't suffer by losses at the optical components introduced along all interferometer arms. As long as the wavelengths of the SPDC photons and of the stabilization laser are dichroically separable, at least one scheme for solving this problem could be found. These will be presented in section 5.1.

- For the free space path the extraction and the coupling of the photon modes from one fused fibre coupler output to the fibre input of the next fused coupler cause additional intensity losses $\propto 10-20\%$, depending on the path length difference chosen. This decreases the indistinguishability between a photon taking the long and another one taking the short arm. However, the expected reduction in the interference visibility is less compared to the reduction given in the free space interferometer due to the spatial mismatch between both modes. The interference visibility in one interferometer arm scales as $V = \frac{2\sqrt{I_1 I_2}}{I_1+I_2} = \frac{2\cdot\sqrt{\eta}}{1+\eta}$ [52] in the ratio η between the intensity I_1 and I_2 of both input modes such that for $\eta = 0,8$ the visibility would only reduce by $0,62\%$ with respect to the ideal visibility. In comparison a reduction of the mode overlap on the nm range can cause a higher reduction in the visibility as is the case for the free space interferometer. This behaviour will be quantified in section (4.1.2).

Conclusion Judging by the advantages and disadvantages listed above, the most suited interferometer type for achieving higher dimensional entanglement is the Hybrid interferometer. Due to its detrimental dispersion characteristics, an all fibre interferometer would not be implementable at the IR wavelengths of the SPDC photons, while for the free space configuration the spatial mode overlap presents the most important limitations for achieving a high interference visibility. In the same way the adjustment of the mode overlap and the reduction of the interdependency of different interferometer arms appended in series is a very time consuming process. Instead, for the hybrid interferometer only the coupling and re-coupling of the mode into the fibre coupler pigtails and the adjustment of the polarization state in both arms is necessary.

However, for the time bin experiment the pump interferometer has to be build in the free space configuration, as fused fibre couplers for the blue wavelength regime (400nm) aren't commercially available. The hybrid configuration is therefore chosen only for the analyzer interferometers.

3.1.3.2   Stability considerations for the energy-time and time-bin entanglement scheme

Both implemented interferometer types, the free space and the hybrid interferometer require an active stabilization over the whole path of the interferometer in order to ensure that the relative phase settings ϕ_A and ϕ_B Alice and Bob can choose to set are not affected by random variations.

It is to note that these discussions are based on the idealized assumption that the frequency of the CW pump laser and of the stabilization laser remains fixed. For diode lasers in single mode operation, typical variations in the laser frequency range to values of $\Delta\nu_{Pump} \leq 500Mhz$ [53] even over short time intervals as long as no frequency stabilization method is applied. Due to the frequencies ω_s and ω_i of the degenerate SPDC photons holding to the phase matching condition (2.7), the variations in both pump laser and SPDC photon's frequency are correlated according to $\Delta\nu_{Pump} = 2\Delta\nu_{SPDC}$. A path length difference introduced by a $60cm$ interferometer is 5 orders of magnitude higher than the wavelength of 805nm of the SPDC photons, involving that the number of wavelengths fitting into this path length difference is $N = \Delta L/(\lambda) \propto 7,45{\cdot}10^5$. Hence a variation in the laser wavelength $\Delta\lambda$ will produce a change 5 orders in magnitude higher in the relative phase $\phi = 2\pi\Delta L/(\lambda)$ of the interferometer, as an approximation displays: $|\Delta\phi| \approx 2\pi\frac{\Delta L}{\lambda}\frac{\Delta\lambda}{\lambda} = 2\pi N\frac{\Delta\lambda}{\lambda} \propto 2\pi$. Therefore, a change of approximately 2π in the encoded phase of the entangled state only due to variations in the laser frequency can be expected even over a short measurement time. Of course, as this phase change scales proportionally with the path length difference, for $\Delta L = 2,40m$ a phase change over 4 full phases of the SPDC photons $\Delta\phi \approx 4 \cdot 2\pi$ can be expected.

The same argument applies to variations in the frequency ν_{HeNe} of the stabilization laser serving as a reference to stabilize the path of the SPDC photons in the interferometer. A corresponding variation in its relative phase $\Delta\phi_{HeNe}(\Delta\nu_{HeNe})$ in the interferometer will be compensated by the stabilization electronics driving the piezo. Of course, as both lasers aren't mode locked to each other and as therefore both lasers have uncorrelated frequency variations, the variation in the path length by the piezo erroneously changes the relative phase for the SPDC photons, too. Effectively, a phase change of $-\phi_{HeNe}$ is introduced. For this experiment a HeNe laser with a specified long term frequency stability in the range $\Delta\nu_{HeNe} \leq 500Mhz$ was implemented.

Phase variations for energy-time entangled states For the energy-time entanglement scheme, these random changes $\Delta\phi_{DC,A,B}$ and $-\phi_{HeNe,A,B}$ in the relative phase both SPDC photons acquire when taking the long interferometer arm in their respective interferometers will be detrimental for the analysis of the energy-time entangled state:

$$|\Psi\rangle_{AB} = 1/\sqrt{2} \cdot (|0\rangle_A|0\rangle_B + e^{i\cdot(\phi_A+\Delta\phi_{DC,A}-\Delta\phi_{HeNe,A}+\phi_B+\Delta\phi_{DC,B}-\Delta\phi_{HeNe,B})}|1\rangle_A|1\rangle_B).$$
(3.1)

A successful scheme for reducing the frequency variations down to $\Delta\nu \leq 10MHz$ is based on the active stabilization on a suited stable reference frequency, as for example the frequency of a photon being emitted after an atomic transition. This stabilization scheme is routine in atomic physics where the laser frequency has to be suited to excite a specific atomic transition. A broad experience exists for the stabilization of Rb-lasers with a wavelength of 780nm for example [51]. However, for this experiment this presupposes that a suitable atomic transition in the 400nm range can be found for stabilizing the pump diode.

As the stabilization laser would have to be dichroically separable from the 805nm SPDC photons (see section 5.1.), the well studied Rb or Cs lasers stabilized on the corresponding atomic transition can't be considered. The wavelength of the HeNe laser (632.8nm) lies within this constraint. HeNe lasers with a long term frequency stability $\Delta\nu_{HeNe} \leq 3MHz$ over 8 hours corresponding to a phase shift $\delta\phi(\nu_{HeNe}) \approx 0,006 \cdot 2\pi << 2\pi$ over $2,40m$ path length difference are commercially available [54].

Phase variations for time bin entangled states However, when considering the time bin entanglement scheme with pulsed diode lasers, these considerations don't apply directly anymore. Due to the pulsed character of the diode, involving that for each pulse a slightly different bias current is applied, the frequency of the pump laser will vary from pulse to pulse. Therefore each SPDC photon pair created by a different pump pulse will acquire a different phase in the interferometers with respect to each other. As no stabilization scheme working for CW lasers can be applied for pulsed laser diodes, at first sight this presents an unsolvable situation.

Nevertheless, a closer analysis of the phase the time bin correlated SPDC photons acquire at the set of pump and analyzer interferometers will reveal that the solution is intrinsic to the time entanglement scheme. It suffices to consider the postselected time-bin entangled state

$$|\Psi\rangle = e^{i\cdot(\phi_A+\phi_B)}|0\rangle_P|1\rangle_{A,B} + e^{i\cdot\phi_P}|1\rangle_P|0\rangle_{A,B}.$$
(3.2)

The state is given by the superposition of the biphoton probability amplitudes for both photons having taken the long interferometer arm in the analyzer interferometer or the

pump photon having taken the long arm of the pump interferometer respectively.

An important condition to be met for the discussion here, is that the same HeNe laser is applied to stabilize all the arms of the pump and analysis interferometers. Therefore the additional phase shifts due to a variation in the frequency of the pump or the stabilization laser described above will contribute to the state as

$$
\begin{aligned}
|\Psi\rangle \quad = \quad & \\
& e^{i \cdot (\phi_A + \phi_B + 2\Delta\phi_{DC,A,B} - 2\Delta\phi_{HeNe,A,B})} |0\rangle_P |1\rangle_{A,B} + \\
& e^{i \cdot (\phi_P + \Delta\phi_P - \Delta\phi_{HeNe,P})} |1\rangle_P |0\rangle_{A,B} = \\
& (e^{i \cdot (\phi_A + \phi_B - \Delta\phi_{HeNe,A,B})} |0\rangle_P |1\rangle_{A,B} + e^{i \cdot \phi_P} |1\rangle_P |0\rangle_{A,B}) e^{i \cdot (\Delta\phi_P - \Delta\phi_{HeNe})} \quad (3.3)
\end{aligned}
$$

where the relations $\Delta\phi_{DC,A} \approx \Delta\phi_{DC,B} \cong \Delta\phi_{DC,A,B}$ as well as $\Delta\phi_{HeNe,P} \approx \Delta\phi_{HeNe,A,B} = \Delta\phi_{HeNe}$ hold as the interferometer arms are equalized up to the coherence length of the SPDC photons. Therefore the change in the phase in both interferometers will be negligible. Due to the phase matching conditions of the degenerate SPDC photons, once the frequency of the pump photon changes, the phase variation $\Delta\phi_P$ in the pump interferometer will correspond to a variation $2\Delta\phi_{DC,A,B}$ for both analyzer interferometers. The same doesn't hold for the variations in the phase $\Delta\phi_{HeNe,A,B}$ of the HeNe laser as the accumulated phase difference is given by the three interferometers it stabilizes. Therefore it still contributes to a random relative phase shift in the entangled state. However, as discussed before, this fluctuation can be reduced to $\Delta\phi_{HeNe,A,B}(\Delta L) << 2\pi$ with frequency stabilized lasers.

The important result is that the phase fluctuations due to the frequency variation in the pulsed laser diode behave as a global phase, and do not influence the relative phase between both correlated probability amplitudes, the parameter setting the entangled state. This results in an additional advantage of the time-bin scheme with respect to the energy-time scheme, as the stability of the latter entangled state is highly affected by the frequency instabilities of the pump and stabilization laser.

The same discussion is valid for higher dimensional states, encoded by the superposition of up to d biphoton states defined by the d possible paths the SPDC photon pairs can have taken through the set of pump and analyzer interferometers. As the path each photon can take is the same up to the coherence length of the SPDC photons, the phase shifts introduced are practically equal, such that for the same reasons given before they only behave as a global phase. For eight dimensional entanglement, the maximal phase fluctuations over several hours due to a variation in the stabilization laser frequency are limited to $\Delta\phi_{HeNe}(7 \cdot \Delta L) = 7 \cdot \Delta\phi_{HeNe}(\Delta L) \approx 0,042 \cdot 2\pi << 2\pi$, for a frequency stabilized laser.

3.1.4   Coincidence Unit

The signal of both detectors measuring the SPDC photon rate at one output of each interferometer is connected with the stop and start input of a Time to Digital Converter (TDC) card [9] connected to a computer running under Linux. This instrument allows to measure arrival time differences between both detectors with a resolution of 72ps or better (of course, the effective resolution is limited by the detectors timing resolution Δt_D), triggered by the detection signal of the SPDC photon connected to the start input. Next, only coincident SPDC photons passing through the corresponding interferometers are discriminated from the single photons emitted at the SPDC process, corresponding to a direct projection onto the coincidence time basis as required for the analysis of the entangled states.

---

[9]ACAM GPX TDC

Chapter 4

Measurements

This section will present the measurement results displaying the energy-time entangled nature of the SPDC photons in a two dimensional Hilbert space. Several adjustments and measurements are necessary prior to this, such as the measurement of the pump laser coherence length and the equalization of the interferometer path length differences of both interferometers. In order to test the suitability of both interferometers for preparing the photon states in a higher dimensional state a detailed study on their characteristics was performed. Finally, the first experimental efforts necessary to prepare the SPDC photon pairs in time bin entangled states are presented. This includes the measurements of the blue pulsed laser diode.

4.1 Franson experiment

4.1.1 Measurement of the coherence length of a blue laser diode source

For energy-time entangled photons, the coherence length of the CW pump source plays an important factor, as described in the theoretical section (2.3): Its value quantifies the distinguishability between the SPDC biphoton states for a photon pair having taken two different interferometer paths in the experimental setup described in section (3.1). A good quality of the two photon interference between both biphoton states can therefore only be warranted for coherence lengths $l_{c,P} >> \Delta L$, i.e. exceeding considerably the path length difference implemented in the interferometers. Therefore this section will be focused on studying the enhancement of the coherence length of a blue laser diode by applying the grating stabilization method, as described in more detail in [49]. The basic function of this method can be described as follows:

The reflection of first order of the holographic grating installed on the laser diode's output is injected back into the diode. The reflected beam has a narrow bandwidth and its central frequency is dependent on the horizontal tilting angle of the grating,

such that once it is re-injected into the diode, only a single frequency mode of the laser diode will be enhanced. Effectively, this results in a reduction in the bandwidth $\Delta\nu_{Pump}$ of the laser diode and a corresponding enhancement of the coherence length $l_c = \frac{c}{\Delta\nu_{Pump}}$. An empirical observation in the experimental group is that the highest stability of the laser diode will be achieved when enhancing only one of the frequency modes dominant for the free running diode.

Higher dimensional entanglement is to be achieved using the time-bin entanglement scheme, such that the entanglement quality doesn't depend upon the laser diode's coherence length being higher than the interferometer path length differences implemented (See section 2.3.). Therefore, it will suffice to warrant that the coherence length is higher than the path length difference of a one arm interferometer, needed for analyzing two dimensional energy-time entangled states as done in this experiment.

The most elegant way to measure the coherence length of a blue laser diode is to use a confocal cavity of the Fabry-Perot type. In our case, one of the two cavity mirrors separated by a distance of $l \approx 12.0cm \pm 0.5cm$ with a high reflection of $R = 96 \pm 2\%$ at a wavelength of 400nm is mounted on a piezo cell. The spatial mode of the grating stabilized laser diode (Nichia NDHV310AFBE2 with 35mW of maximal output power) is focused into the cavity. To be able to scan the full spectral range (FSR) of the cavity a periodic triangle signal amplified by a high voltage amplifier is applied to the piezo tube. The FSR is defined as the frequency interval between the respective interference maxima in the cavity and is given by $\Delta\nu_{FSR} = \frac{c}{2l} = 1,25GHz$ in this case. The coherence length of the laser can directly be extracted by measuring the FWHM $\Delta\nu_{FWHM}$ of the transmission peak. The coherence length can be defined as $l_c = \frac{c}{\Delta\nu_{FWHM}} \approx \frac{\lambda_0^2}{\Delta\lambda_{FWHM}}$. It is to note, however, that the resolution of the cavity is limited by the reflectivity of the mirrors used, such that the maximal resolvable coherence length which can be measured will be limited too. The cavity resolution $\Delta\nu_{FWHM,R}$ can be extracted via the Finesse, defined as the ratio of the FSR with respect to the FWHM of the transmission maxima: $F = \frac{\Delta\nu_{FSR}}{\Delta\nu_{FWHM}} = \frac{\pi\sqrt{R}}{1-R}$. As the second part of the equality depends only on the reflection coefficient R of the cavity mirrors used, the finesse is $F = 69, 8 \pm 0, 5$. The measurement of the coherence length will therefore be limited by the maximum achievable frequency resolution $\Delta\nu_{FWHM,R} = \frac{\Delta\nu_{FSR}}{F} = 17,91MHz$ to $l_{c,max} \approx \frac{c}{\Delta\nu_{FSR}} = 16,75m$.

The cavity output signal is measured with a photodiode and is visualized on an oscilloscope, as depicted in Fig. (4.1).

As discussed before, the FWHM of the transmission maxima will be a direct measure of the coherence length. A fit into the transmission curve on the oscilloscope signal yields a time width of $\Delta t = (8, 9 \pm 0, 02) \cdot 10^{-4}s$. The conversion of this value into the path scanned by the piezo cell is still necessary. The path length scanned during the measurement time interval $\Delta t = (9 \pm 0, 02)ms$ is given by $\Delta s = d_{31} \cdot L \cdot \Delta U/d \cdot \Delta t \cdot f$ [55], where $\Delta U = 8, 14V$ is the potential difference between the maximum and minimum
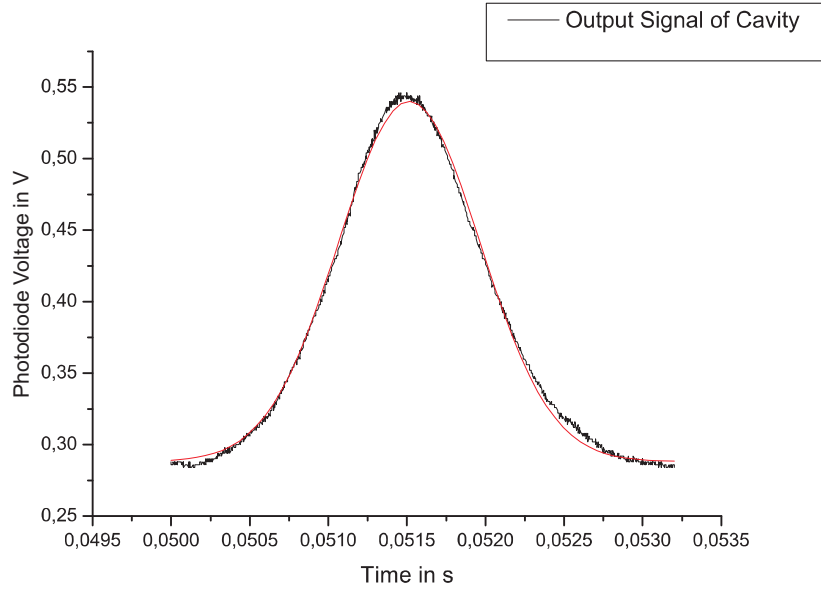
Figure 4.1: *Output signal at the cavity measured with a photodiode and visualized on an oscilloscope. The FWHM of the transmission curve observed is proportional to the coherence length of the diode. The piezo actuator was scanned with a triangle signal with a voltage difference of $\Delta U = 8,14V$ and a frequency of $f = 64Hz$. A higher bound for the coherence length of $l_c \leq 4,91 \pm 1,23m$ could be measured.*

voltage of the applied signal while f is the scan frequency of the signal, $d = 1mm$ is the wall width of the piezo cell, $L = 0,01m$ is the length of the piezo tube and $d_{31} = 2,1 \cdot 10^{-10}/V$ is the piezoelectric constant of the piezo cell. Hence a value of $\Delta s = (9,8 \pm 0,01) \cdot 10^{-9}m$ can be extracted.

As interference is responsible for observing a transmission maximum, the path difference Δs scanned over which interference is observed is limited to the uncertainty $\Delta\lambda_{FWHM}$ of the laser diode wavelength. This dependency can be rewritten as $\Delta\lambda \geq \frac{\lambda \cdot \Delta s}{s}$ with the length s of the cavity. A lower bound for the bandwidth of $\Delta\lambda_{FWHM} \geq (8,23 \pm 0,008) \cdot 10^{-9}\lambda_0$ can be extracted by this way. A higher bound for the coherence length of the laser diode therefore corresponds to $l_c \approx \frac{\lambda_0^2}{\Delta\lambda_{FWHM}} \leq 4,91 \pm 1,23m$. Therefore, the coherence length measured for this diode clearly satisfies the condition $l_c >> \Delta L$. This shows that the grating stabilization method is very well suited for achieving the desired coherence lengths.

The final measurements on energy-time entanglement of the SPDC photons pumped by a blue laser diode were performed on a similar grating stabilized diode (Nichia NDHV330APC). Therefore a similar coherence length can be expected when carefully stabilizing its frequency. Nevertheless, no measurement of its coherence length in a cavity was made. Instead, measurements done with it before by coupling it into a free space Michelson interferometer with a path length difference of up to 2,20m were available.

An interference visibility of up to V=32,6%, V=51,56% and V=62,1% could be observed at one output of the interferometer for path length difference of $2,20m$, $1,20m$ and of $0,60m$ respectively. As the visibility depends on the ratio between the path length difference implemented and the coherence length of the laser, a lower bound for the coherence length can be given. As the parameterization of this decrease will depend on the line shape of the frequency distribution of the laser, which is not known, a lower bound for the coherence length is chosen. This bound is given by the path length difference at which the interference visibility is reduced to one half. Following this scheme we extract a lower bound of $l_c \approx 1,20m > \Delta L$, a value which is suited for the experiment. Later, this value was further improved by a careful frequency stabilization of the diode such that a visibility of $V \geq 90\%$ could be measured at a path length difference of $0,60m$. Therefore, it can be argued that the coherence length reached larger values $l_C > 1,20m$ during the experiment for achieving energy-time entanglement.

4.1.2 Characterization of the different interferometer types implemented

As discussed in section 3.1.3, 2 different Michelson interferometer types, the Hybrid and the Free Space type, were studied in this experiment. However, due to the Hybrid interferometer not being well studied before, a quantitative comparison of its most important characteristics with respect to the Free Space interferometer had to be given.

Indistinguishability of overlapping modes in the interferometers   As the quality of the entanglement will depend directly on the indistinguishability of the overlapping modes in each interferometer type, this characteristic will be studied in first place. The best way to quantify the indistinguishability of two overlapping modes at the respective interferometer beamsplitters, is the observation of the first order interference visibility achieved for a suited source being coupled into the interferometers.
As the path length difference implemented in the interferometers is orders of magnitude higher than the coherence length of the SPDC photons, no single photon interference could be observed. Therefore the optimal adjustment of the mode indistinguishability had to be done with the help of a grating stabilized laser diode at 812nm, which offered the desired coherence length properties. It was considered that the deviation of 7nm of the laser wavelength from the central wavelength of the SPDC photons at 805nm would only lead to a small error in the degree of indistinguishability to be achieved for the SPDC photons. The contributions to this error are given in its majority by the slightly different collimation properties of the 812nm beam in the Free Space interferometer or by the slightly different polarization transformation in the fibres of the Hybrid interferometer.

As already discussed in section 3.1.3., for the Free Space interferometer the non perfect mode overlap offers the highest limitation in order to achieve a high interference visibility. In this setup it can be adjusted by guiding the 812nm laser beam into the same path in the interferometer as the SPDC photons. First, the beam guided by a single mode fibre is collimated with an aspheric lens, such that the size of both retro-reflected beams after the second BS, observed on a CCD camera, is the same. The mode overlap between both modes could be adjusted by use of the differential adjuster screws on the retro-reflection prism's supports and by varying the horizontal position of one of the prisms with a micro-translation stage. For reasons which will be described in section (4.1.3) one of the output modes of the interferometer was coupled into a SM fibre, such that effectively only one spatial mode of both retro-reflected beams is coupled. The spatial mode overlap between both coupled modes is maximal such that the reduction in the interference visibility due to this factor is reduced.

Only small losses in the visibility could be attributed to a different rotation of the polarization state of the photons in both paths of the interferometer. The rotation was minimal for the adjusted input polarization of H and amounted only to a shift of $\Delta\psi_R = (0, 5 \pm 0, 1)\%$ with respect to this input polarization. The expected reduction in the visibility $V' \propto cos^2(\Delta\psi)V = 99,996\% \cdot V \approx V$ is therefore small.

Nevertheless, after the adjustment, a fitted visibility of only $V = (89, 67 \pm 0, 2)\%$ could be achieved as depicted in Fig. (3.4). The fitting function was parameterized as $C(1 + V\sin[2\pi(x + \phi)/\lambda])$ as a function of the visibility V, phase ϕ, the wavelength λ and a constant offset C. The fitted visibilities were only slightly reduced by $\leq 2\%$ with respect to the raw visibilities observed. A small mismatch between the fitted wavelength and the wavelength of $812nm$ can be attributed to the inaccuracy of up to 20% in the expansion coefficient of the piezo.

The interference visibility achieved was high enough such as to ensure the violation of a Bell inequality in the subsequent experiments according to the discussions in section (2.5.). Due to the temporal limitation of this work, the visibility couldn't be further improved.

In comparison, the performance of the Hybrid interferometer was tested such that the same 812nm laser was coupled into one of the interferometer inputs. First, the beam following the free space path of the interferometer and redirected back by the retro-reflection prism had to be coupled into the input fibre pigtail of the second fused fibre coupler such that the coupled intensity was maximized. Only $70, 1\%$ of the input intensity could be coupled as measured in both interferometer outputs. From these losses of $29, 9\%$ in the intensity, $(8, 7 \pm 1)\%$ could be associated to reflection losses at the retro-reflection prism not provided with a suited antireflection coating for 805nm. Nevertheless, the expected visibility considering the splitting ratios and losses observed in this interferometer setup would still reach up to 97%.
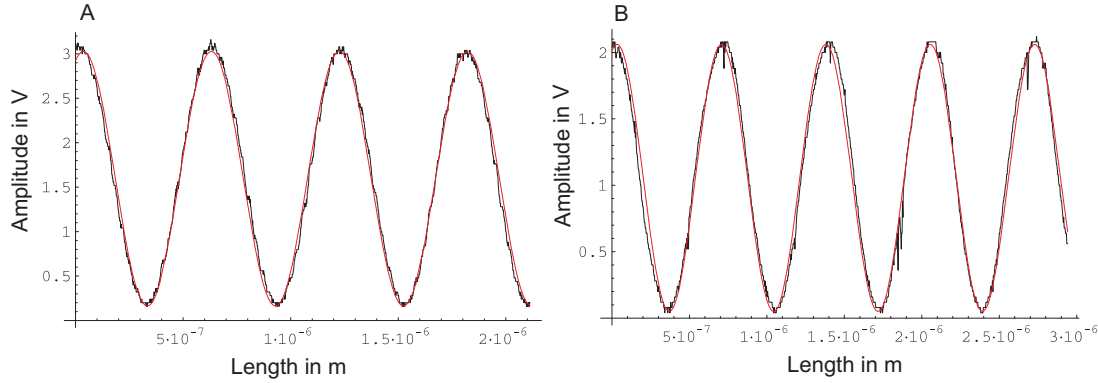
Figure 4.2: *Measured interference visibility at one output of the Free Space (A) and of the Hybrid (B) interferometer for a grating stabilized laser diode at 812nm. In order to scan the interference fringes, an amplified triangle output signal was applied on the piezo actuator such as to periodically change the path length difference of the interferometers. On the signal measured by a photodiode and displayed on a 40MHz oscilloscope, an interference visibility of (A) $V_{FS} = (89,67 \pm 0,2)\%$ and of (B) $V_H = (95,16\pm0,45)\%$ could be fitted. The fitting function was parameterized as $C(1+V\sin[2\pi(x+\phi)/\lambda])$ as a function of the visibility V, phase ϕ, wavelength λ and a constant offset C*

Additionally, it is necessary to ensure that both modes of the interferometer overlapping at the second fused fibre coupler are indistinguishable in their polarization state. Therefore, the polarization state had to be adjusted on two different input polarizations rotated by 45° with respect to each other, for what purpose the fibre polarization controllers were used. As the transformation adjusted for one polarization will be lost when adjusting on the other polarization, a good strategy to follow is to make the "pad-ears" adjustment on each polarization as independent as possible. Once a rough adjustment has been achieved by this method, usually it will suffice to turn only on one "pad-ear" at a time for the fine tuning, such that a wrong adjustment can easily be reversed. An accuracy better than $0,35\%$ could be achieved for the adjustments on both H and 45° polarizations.

The interference fringes recorded when scanning the path length difference by the piezo actuator are depicted in Fig. (4.2). The interference visibility of $V = 95,16 \pm 0,43\%$ could be fitted. This demonstrates that the Hybrid interferometer offers an important advantage with respect to a Free Space interferometer in regards to achieving higher dimensional entanglement, as a good interference visibility can be achieved with less efforts.

Stability of the implemented interferometers   On the other side, the stability of the different interferometer types has to be warranted:

As described before, the Hybrid interferometer not only consists of a free space part, but of a path guided in optical fibres, too. In order to compensate for the phase fluctuations in the free space path an active stabilization scheme has to be used, by

coupling the HeNe laser into the interferometer and by the employment of suited P-I (Proportional-Integral) stabilization electronics.

It has to be ensured that a closed control loop exists between the difference of the voltages measured at the two output photodiodes of the interferometer and the P-I regulated and amplified voltage applied at the piezo actuator. A closed loop will therefore warrant that all vibrations in the optical path will be compensated for by the piezo actuator setting the path length difference of the interferometer.

Due to the asymmetric splitting ratio in both of the fused fibre couplers implemented, the intensities of the interfering HeNe modes split up into any of the interferometer outputs are not equal. When scanning the interference fringes with a piezo and visualizing them on an oscilloscope, it could even be observed that the minimum voltage in one output doesn't meet with the maximum interference voltage in the other output. As the stabilization electronics compares both photodiode signals to a zero voltage level, this stabilization scheme wouldn't be implementable.

However, the easiest solution consists in changing the position of the photodiodes, such as to change the magnitude of the laser beam incident on the photodiode area. Effectively, the magnitude of the interference signal measured can be changed, until the average of the interference signals in both outputs overlaps again. The difference between both photodiode voltages can be 0 again. Of course, the visibilities observed between both outputs differed by up to 30%, what was still sufficient for achieving a successful stabilization. The same approach could be used for matching the asymmetric output signals of the HeNe laser at the Free Space interferometer.

A second issue to handle are the correct settings of the Proportional and Integral regulation devices of the stabilization electronics, in regards to the specific composition of both interferometers: For the free space interferometer, the optimal stabilization can only be achieved for a suited integration time of the integrator, such that the piezo is readjusted with exactly the same frequency as the mechanical oscillations destabilizing the interferometer. The proportional regulation parameter is set such that the regulation loop doesn't oscillate, as could be monitored in the output signal measured on an oscilloscope.

In difference, for the hybrid interferometer, the question is if the additional drifts in its length due to temperature variations can be compensated by the same stabilization scheme as used for its free space path:

Readjusting the hybrid interferometer such as to be composed only by its fibre components and coupling a reference diode at 812nm into one output enabled to approximate the velocity of phase drifts given only on the fibres. The drifts over a full phase were varying on average on a timescale of $\overline{\Delta t}_{Drift,Fibre} \approx 5,1 min$ corresponding to an average drift frequency of $\overline{f}_{Drift,Fibre} \approx 0,0033 Hz$ (See Fig. (4.4)). Of course this measurement is only approximate, as the contribution of a possible fluctuation in the

laser frequency wasn't monitored.

The low frequency of the fibre drifts can be explained by the fact that the corresponding length difference between the output and input fibre pigtails are nearly equalized, such that a change in the fibre path will be nearly synchronous as long as the temperature changes are not localized on one fibre. The relative phase between the long and the short interferometer arm, the parameter which characterizes the entangled state, will therefore suffer only variations with a small frequency.
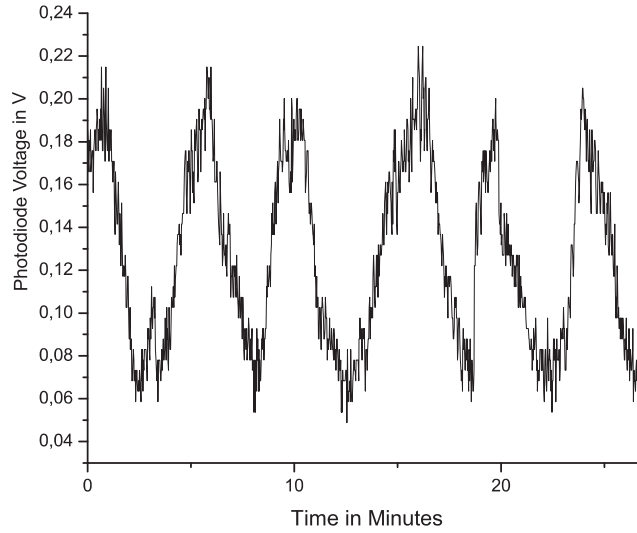

Figure 4.3: *Measured fluctuations in the output signal for the HeNe laser of an all fibre interferometer built with the same optical fibres implemented in the Hybrid interferometer. The measured voltage drifts over a whole phase periode have an average frequency of $f_{Drift,Fibre} \approx 0,0032Hz$.*

The frequency of the integrator circuit of the stabilization electronics should therefore be chosen to be slightly lower than for a free space interferometer, in order to be able to compensate these drifts too.

Experimentally, it could be verified that for the Free Space interferometer the optimal integrator frequency was $f_{FS} = \frac{1}{R \cdot C} = 6,51Hz$, given by a condensator with $C = 47\mu F$ and by a resistance of $R = 138.5k\Omega$. For this optimal setting the variations in the amplitude in one output of the interferometer was monitored in one of the outputs of the stabilized interferometer over a total time of up to $5\frac{1}{2}$ hours. As the interference amplitude depends on the relative phase ϕ, the variation in the amplitude will be a direct measure of the phase variations $\Delta\phi$:

A parameter for characterizing the quality of the stabilization achieved is the ratio between the range ΔU_F of the fluctuations measured and the difference between the maximum and minimum interference amplitude ΔU_0 observed, which are delimited by the two dotted lines in Fig. (4.4 B). This corresponds to an average phase stability of $\Delta\phi = \frac{2\pi\Delta U_F}{\Delta U_0} = 0,096rad$ over the whole measurement time.

The stabilization of the Hybrid interferometer was possible with a similar quality, how-
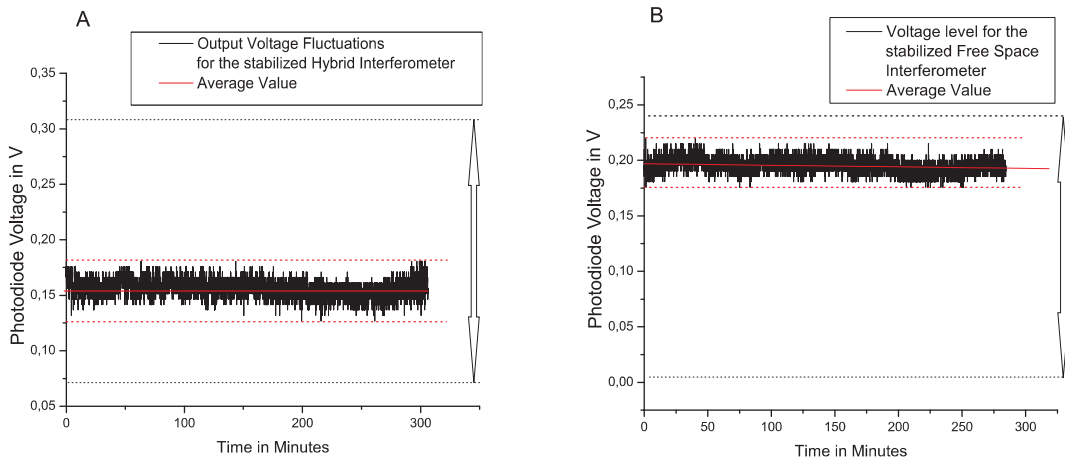
Figure 4.4: *Monitored output signal for the stabilization laser in one output of the Hybrid (A) and Free Space (B) interferometer over a total measurement time of up to $5\frac{1}{2}$ and 6 hours, respectively. The variations in the amplitude quantify the achieved phase stability of the interferometers. The two dotted lines in each figure represent the level of the maximum and minimum interference levels observed. Normalized with respect to the difference between these voltage values, a phase stability of (A) $\Delta\phi_H = \pm 0, 10 rad$ and (B) $\Delta\phi_{FS} = \pm 0, 09 rad$ respectively with respect to the average phase was achieved over the whole measurement time.*

ever the frequency of the integrator had to be chosen to be lower than for the Free Space interferometer. The optimal setting could be found for a resistance of $R = 88.5 k\Omega$ and a capacitance of $C = 47 \mu F$ corresponding to the optimal integration frequency of $f_H = \frac{1}{R \cdot C} = 4, 15 Hz$. For this setting the fluctuations in the amplitude in one interferometer output are depicted in Fig. (4.3 A). Over the whole measurement time of up to 6 hours the corresponding maximal change in the phase was evaluated to be $\Delta\phi = \pm 0, 10 rad$.

It is to note that, due to a systematic error in the measurement device [1], only found after the measurements were performed, the fluctuations measured are higher than the real fluctuations. When measured with a 40Mhz bandwidth oscilloscope, phase fluctuations in the range of only $\Delta\phi = \pm 0, 04 rad$ over a time interval of 15 min could be observed for the Hybrid interferometer. However these fluctuations weren't monitored over many hours.

Nevertheless, the important result of these measurements is that the phase stability of the Hybrid interferometer is nearly equivalent to the stability achieved for a Free Space interferometer, whose high stability has been studied in other experiments [50].

Finally it is to note, that the measured stability in the interferometer's phase doesn't automatically warrant the stability of the interferometers: Phase shifts due to frequency variations in the HeNe laser are corrected by the active stabilization scheme together with the mechanical instabilities and drifts of the interferometer. This disables the

---

[1]DT304 8-channel voltage measurement device

correction done on the path length difference of the SPDC photons. Therefore, a high stability of the pump and stabilization laser has to be warranted additionally.

4.1.3 Matching the interferometer path length differences

As explained in the theoretical section (2.3), energy-time entanglement between the state of the SPDC photon pairs used in this experiment can be achieved when the path difference $\Delta L = \Delta T/c$ introduced into both analyzer interferometers is chosen to be exactly the same, up to an accuracy given by the coherence length $l_c \approx 108\mu m$ of the SPDC photons. This warrants the indistinguishability of each of the photon pairs when passing through the long arm of the respective interferometers.
A first practical limitation when trying to directly match the time delays ΔT introduced by the interferometers, is that the needed accuracy given by the coherence time of the SPDC photons $t_c \propto 360 fs$ lies well below the resolution of standard measurement electronics. Therefore another methodology based on interference has to be chosen:
It consists in rearranging both interferometers, such that the output of one of them is directly coupled into one of the inputs of the second one. Once single SPDC photons are coupled into this set of interferometers, 4 paths through the first and second interferometer $|0\rangle_1|0\rangle_2, |0\rangle_1|1\rangle_2, |1\rangle_1|0\rangle_2$ and $|1\rangle_1|1\rangle_2$ are possible. Changing the path length difference will yield constant output intensities as long as the interferometers are mismatched. Only once the interferometer path lengths are equalized up to the coherence length of the SPDC photons and the polarization state of the photons in both output beamsplitters is equal, the two states $|1\rangle_1|0\rangle_2$ and $|0\rangle_1|1\rangle_2$ of the photons will interfere. As the FWHM of the envelope of the interference pattern is determined by the single photon coherence length $l_c \approx 108\mu m$, a very accurate matching adjustment can be realized. However, as only two out of the four possible probability amplitudes can interfere and the non-interfering states aren't temporally discriminated by the electronics, a maximum theoretical visibility of 50% can be expected. As over the range of $l_c \approx 108\mu m$ many interference fringes will be scanned for arbitrary phase settings, in average a value near to the maximum and minimum interference amplitude will be measured. Therefore it isn't necessary to stabilize the interferometers during the matching scan in order to clearly observe the interference fringes.
For this experiment, it was chosen to couple the SPDC photons into the Hybrid interferometer first. The path length difference of the second free space interferometer could be continuously changed over a range of up to 5cm with a resolution of $2\mu m$ by shifting the position of one of the retro-reflection prisms with a step motor mounted on a micro-translation stage.
A problem arises due to the non-perfect guiding of the micro-translation stage, as a shift of the retro-reflected mode in the vertical and horizontal basis would lead to a reduction of the interference visibility at the BS. In order to apply an alignment method

described in detail in [56], one output of the interferometer had to be coupled into a multi-mode fibre mounted on two micro-translation stages setting the horizontal and vertical position of the coupler. However, probably due to additional guiding errors of the translation stage after the mounting of the piezo actuator into it, a compensation for these shifts was only possible over half of the range of the translation stage.

Therefore it was chosen to couple the photons directly into a single mode fibre, in order to ensure that even if the mode overlap of both retro-reflected modes is changed, only single modes of both overlapping SPDC photon modes are selected by the fibre. By this method the interference probability of both coupled modes could be maximized. However, due to the lower collection solid angle of this fibre type with respect to a multi-mode fibre, a reduction in the coupled intensity could be observed when changing the path length difference over more than 1cm. Therefore this shift had to be compensated several times during the scan of the path length difference by readjusting the tilting of the affected retro-reflection prism.

Additionally, a non trivial problem is the accurate measurement of the path length difference introduced into the Hybrid interferometer. Probably due to density fluctuations in the fibre material conditioned by the manufacturing process, the optical path length introduced by the fibres cannot be directly determined by measuring the path length of the fibre pigtails by a meter.

The solution consists in using a pulsed laser and to measure the pulses with a fast photodiode after they are split up at the respective interferometers. A fs-laser at 780nm with a bandwidth of 6,5nm was used and coupled into each interferometer. A fast photodiode [2] with 7GHz bandwidth was used in order to measure the pulse intensity at the output of each of the interferometers. The signal was only resolvable on an oscilloscope operated in 10GHz bandwidth mode of an oscilloscope [3] after connecting the photodiode signal through an additional 3dB attenuation. By this method a resolution better than 100ps, corresponding to a path length difference of 30mm could be reached. This corresponds to a length smaller than the adjustment range of the translation stage. By this method the path length difference of both interferometers could be adjusted to the same time delay $\Delta t = (2,45 \pm 0,1)ns$, as depicted in Fig. (4.5), what corresponds to a path length difference of $\Delta L = (73,5 \pm 3)cm$.

With this measurement a rough alignment of the interferometer path length differences could be achieved. For the fine adjustment a scan with the step motor was necessary. As the coherence lengths of the fs-laser and of the SPDC photons considered in this experiment were very similar, the scan could be simplified by scanning the interference fringes with the 780nm fs-laser. The intensity of the laser was high enough such that it could be directly measured on a usual photodiode instead of an APD, subject to an

---

[2]SUV7-FC of Thor Labs
[3]Le Croy 574
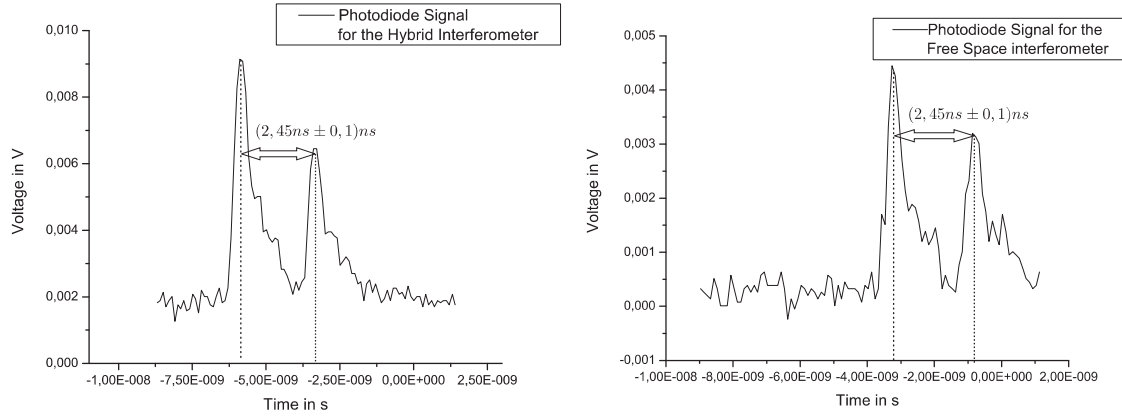
Figure 4.5: *Measured signals of a fs pulse split up into two pulses in the Hybrid and the Free Space interferometers. A fast photodiode and an oscilloscope operated in the 10GHz bandwidth modus were used. The time delay between both signals corresponds to $\Delta t = (2,45 \pm 0,1)ns$. The difference in the pulse amplitudes is due to the losses in the long arm of the Hybrid interferometer and due to the non-optimized adjustment of the Free Space interferometer.*

easy corruption of the scan. However, the measurement displayed in Fig. (4.6), was realized with an APD:
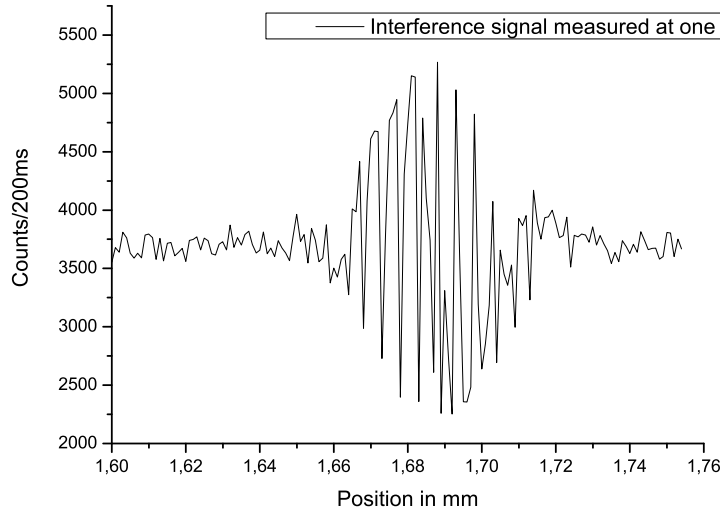
Figure 4.6: *Interference signal between the two states $|1\rangle_1|0\rangle_2$ and $|0\rangle_1|1\rangle_2$ encoded by the Hybrid and the Free Space interferometer connected in series while scanning the position of one of the retro-reflection prism. The FWHM of the envelop function corresponds to the coherence length of the fs-laser of $t_{c,fs} \approx 60,9\mu m$.*

The centre position of the interference pattern observed was $x_0 = 1,688 \pm 0,007mm$. The FWHM of the envelope function of the interference pattern observed corresponds to a coherence length of $t_{c,fs} \approx 60,9\mu m$, differing from the approximated coherence

length of $t_{c,fs} \approx 93, 6\mu m$ of the fs laser. The reason for this might be that the Fourier transform of the laser's pulse form is, specifying its bandwidth, is unknown, such that only an approximation can be given for the coherence length.

Nevertheless, it could be observed that the centre of the interference envelope is slightly shifted with respect to a matching measurement with SPDC photons at 805nm. This could be due to the different optical path difference a photon at 805nm acquires on the small fibre path's contribution to the path length difference of the Hybrid interferometer. This contribution of approximately $\Delta x \approx 9\mu m$ is due to the length difference of the fibre pigtails, which was estimated to be less than 2cm.

This is an important factor to consider as the visibility V' of the two photon interference will vary as $V' = V \cdot e^{-((\Delta L_A - \Delta L_B)/l_c)}$ with the mismatch $\Delta L_A - \Delta L_B$ between both path length differences (See equation (2.14)). Therefore this mismatch should be kept low with respect to the coherence length l_c of the SPDC photons.

However, the adjustment of the path length difference with SPDC photons is difficult due to the relatively low ratio between the single photon count rates and the noise background. The corruption of the scan results happens very easily, such that the localization of the matching point is more difficult.

4.1.4 Franson experiment for a two dimensional entangled state

Having matched the path length difference of both analyzer interferometers up to the coherence length warrants that the respective photon pairs can be described as a coherent superposition of the biphoton states $|0\rangle_A|0\rangle_B$ and $|1\rangle_A|1\rangle_B$). Only as long as the condition $\tau_1 >> \Delta T$ for the corresponding coherence times τ_1 of the pump laser holds, both biphoton states remain indistinguishable and can be superposed to an energy-time entangled state

$$|\Psi\rangle_{AB} = 1/\sqrt{2} \cdot (|0\rangle_A|0\rangle_B + e^{i\cdot(\phi_A+\phi_B)}|1\rangle_A|1\rangle_B).$$

Laser Stability   That the latter condition holds was ensured in section (4.1.1), but nevertheless it has to be warranted that it still holds over the whole measurement time. This was monitored on the additional interferometer into which one mode of the blue laser diode was coupled, as the interference visibility observed in one output while scanning its path length with a piezo quantifies the frequency stability of the diode.

The frequency stability of the stabilization laser has to be monitored, too, as the phase stability of the interferometers is dependent upon this factor. Therefore one mode of the stabilization laser was coupled along a different path into this additional interferometer, as depicted in Fig. (3.1). By this method, multimode operation of both lasers could be observed by a drastic reduction in the interference visibility. Similarly, it was possible to attribute the observed phase drifts to variations in the respective laser fre-

quencies:

Phase drifts due to mechanical instabilities in the optical path would lead to a synchronous change in both laser's phase in the interferometer, therefore being distinguishable from frequency drifts between both lasers, as these aren't mode locked to each other. Qualitative statements about the relative frequency stability of both lasers could be made: As the HeNe was running more stable than the blue laser diode, phase drifts in the interference signal were faster for the latter diode and could be referenced to the relatively stable phase of the HeNe signal. The search for an optimal current setting of the blue laser diode could be undertaken, until the velocity of its phase drifts was reduced. This enabled to further reduce the relatively high frequency instability of the blue laser diode, detrimental for the analysis of the entangled state (See section (3.1.3.2)).

Count Rates and Coincidence time measurement   As outlined in section 2.4., the violation of a Bell inequality defined for photons with a state encoded in the energy-time basis will be necessary, in order to univocally prove the entangled nature of the photon pairs. When measuring coincident photon events for $t_A - t_B = 0$ the coincidence count rate $R_{+,+}^{A,B}(\phi_A, \phi_B) = R_0/4 \cdot (1 + V \cdot \cos(\phi_A + \phi_B))$ and the correlation function $E(\phi_A, \phi_B) = 4P_{+,+}^{A,B}(\phi_A, \phi_B) - 1 = V \cos(\phi_A + \phi_B)$ could be extracted.

The measurements were performed such that each of the H and V polarized SPDC photons were coupled into distinct interferometers and one output of each interferometer was finally coupled into a multimode fibre. The single count rates $P_+^A(\phi_A)$ and $P_+^B(\phi_B)$ in each of the detectors were measured on a counting device (DT340). Count rates of 2000/s and 2500/s photons could be observed for each interferometer respectively for an applied pump diode current of 48,9mA (Of course, approximately one half of the photons take the other interferometer output). Losses in the interferometers account for the relatively low count rates with respect to count rates of 8000-9000/s as measured before coupling the photons into them. This could be evaluated by measuring the loss rate with a 812nm diode, yielding a total loss of $(42 \pm 2)\%$ for the Hybrid interferometer. These can be attributed to the coupling and reflection losses of 10-20% in each of the 3 fibre couplers. Similarly, coupling losses into the SM and MM fibres implemented account for a total loss of $(49 \pm 2)\%$, for the Free Space interferometer. As expected for these interferometer types with a path length difference ΔL much higher than the coherence length of the SPDC photons l_c, no interference in the single count rates could be observed.

Further on, the coincidence count rate $P_{+,+}^{A,B}(\phi_A, \phi_B)$ between the photon pairs was measured by triggering the start and stop timing measurement on a TDC measurement card with each of the APD's output signal:
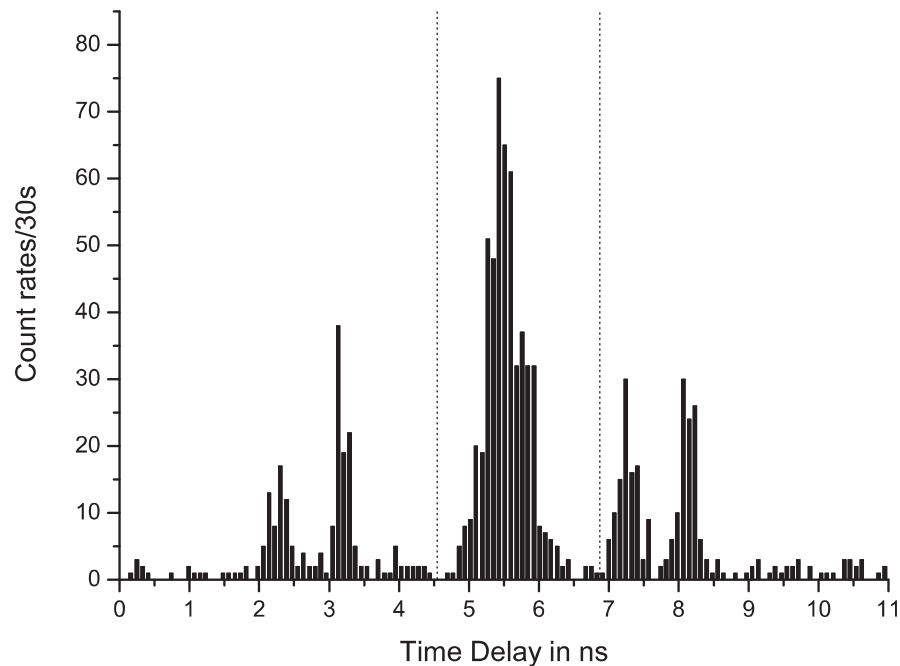
Figure 4.7: *Measurement of the time of arrival difference between both correlated photons being coupled into their respective analyzer interferometers with the TDC measurement device. The integration time corresponds to 30s and the time bin width corresponds to 82ps. The count rates of the central peak are proportional to the amplitudes of both $|0\rangle_A|0\rangle_B$ and $|1\rangle_A|1\rangle_B$ biphoton states overlapping with respect to the coincidence time, while both side peaks correspond to the biphoton states $|0\rangle_A|1\rangle_B$ and $|1\rangle_A|0\rangle_B$ respectively. Two dotted lines delimiting the range of the postselection window are displayed, such as to select only the count rates distributed around the central peak for posterior analysis. The reason for the side peaks splitting is not known, yet.*

Three coincidence time peaks are recorded in Fig. (4.7.), which correspond to the four biphoton states $|0\rangle_A|1\rangle_B$, $|0\rangle_A|1\rangle_B$) and the states $|0\rangle_A|0\rangle_B$) and $|1\rangle_A|1\rangle_B$). The latter two states are indistinguishable and overlap such that the measured coincidence times are distributed around the central peak. Therefore, a postselection measurement between the two time intervals marked in Fig. (4.7.) is made, in order to measure only the sum of the count rates distributed over the central peak.

It is to note, that the TTL output signal of the detectors had a logic level of 2,6V, which mismatched from the minimum required trigger level of 3V of the Acam TDC card. Therefore it was decided to transform the TTL signal into a NIM signal such as to be reconverted by a NIM to TTL converter with a logic level of 3V, sufficient for triggering the counts at the TDC card. The additional processing of the detector's electronic signal might be the reason for the side peaks splitting up as observed in Fig. (4.7.). Nevertheless, no splitting in the central peak was observed. Measurements on the output signals of both interferometers with a fast photodiode enabled to rule out a possible optical reason for this effect.

Coincidence count rates of nearly 20-30/s could be observed distributed between all three peaks, what corresponds to only about 8% of the coincidences before the interferometers (13,5% coincidence/single ratio). A rough approximation suffices to show that this fact is accounted for by the losses in the single photon count rates of 42% and 49% measured in each interferometer, as, due to their random nature, these will contribute to the squared amount of losses in the coincidence counts. The expected rate of $\approx 8,9\%$ corresponds very closely to the value measured above. This already hints at the necessity of reducing the losses in the interferometers by the use of suited anti-reflection coatings on the fibre interfaces, for example.

Two-photon correlation and violation of a CHSH inequality It could be observed that for a fixed integration time, the postselected coincidence count rates show a large variation with a change in the path length difference in each of the interferometers, while the count rates of the side peaks only suffer slight deviations from an average count rate. This observation can be accounted for by two photon interference between both postselected biphoton states with a change on both phase settings ϕ_A and ϕ_B of the interferometers. This characteristic and the fact that single count rates remained constant enables to apply the special CHSH Bell inequality as derived in section 2.4.:

$$S = |3E(\Phi) - E(3\Phi)| < 2 \tag{4.1}$$

yielding a minimal visibility V

$$S = 2\sqrt{2}V < 2 \Rightarrow V \geq 1/\sqrt{2} \approx 0,707 \tag{4.2}$$

where $E(\Phi) = V \cdot \cos(\Phi)$ is the correlation function depending only on the sum of Alice's and Bob's phase settings $\Phi = \phi_A + \phi_B$. A change in any of the two phases will show a cosinosoidal change in the coincidence count rate $R_{+,+}^{A,B}(\Phi) = R_0/4 \cdot (1 + V \cdot cos(\Phi))$ and in the correlation function $E(\Phi)$.

This is the behaviour actually measured, as depicted in Fig. 4.8, while changing the phase in the Free Space interferometer with a glass plate mounted on a rotation motor: It is possible to observe that the coincidence count rates can clearly be fitted by a sinusoidal function parameterized as $R_c = C(1 + V \sin[2\pi(x + \phi)/\alpha])$ as a function of the glass plate tilting angle period α and phase ϕ. The linearity between the tilting angle of the glass plate and the phase shift acquired by the photons holds approximately for small tilting angles. The visibility of the fitted interference fringes corresponds to $V = 86, 39 \pm 4, 12\%$.

Accidental coincidences are registered by the TDC, too, whose average value is given by the lower bound depicted in Fig. (4.8). These are determined by the finite probability that two dark counts of the detectors or a dark count and a single SPDC photon whose
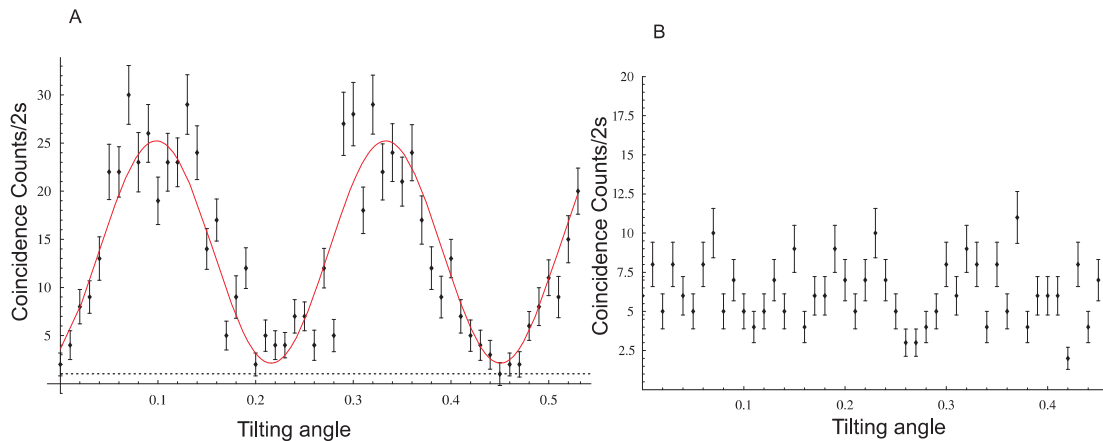
Figure 4.8: *Scan of the sum of the postselected coincidence count rates distributed around the central peak (A) and around one side peak (B) in dependence of the tilting angle of a glass plate on the Free Space interferometer. With the tilting of the glass plate the phase setting ϕ_A in this interferometer is changed. The variation of the measured coincidence rates can clearly by fitted by a sinusoidal function $R_c = C(1 + V \sin[2\pi(x + \phi)/\alpha])$ yielding a two-photon interference visibility of $V = 86,39 \pm 4,12\%$. After subtracting the measured accidental coincidence count rate delimited by the dotted line, a visibility of $V_{AC} = 94,70 \pm 4,53\%$ can be fitted. No interference can be observed in the count rates of the side peak, as expected.*

pair has been absorbed in one of the interferometers are measured as coincident by the TDC over the postselection window's time width. With the TDC they could be directly measured by counting the coincidences inside a postselection window with the same width as chosen for the central peak, but placed some ns far away from where a coincident count is expected. The measured average accidental coincidence rate was 1,095/s. The net visibility which can be fitted when subtracting this offset value corresponds to $V_{AC} = 94,70 \pm 4,53\%$.

The observed visibility therefore clearly exceeds the bound of $V \geq 1/\sqrt{2} \approx 0,707$ for a LHV theory. The Bell parameter reads as $S = 2,443 \pm 0,117 > 2$ and as $S_{AC} = 2,679 \pm 0,128 > 2$ when subtracting the accidental coincidences, such that the energy-time CHSH inequality is violated by 4 and 5 standard deviations, respectively. According to the reasoning in section (2.5) the considered biphoton states are energy-time entangled.

It is clear however, that this experiment isn't designed to close the most important loopholes inherent to the formulation of a Bell inequality for this experimental setup. As the detection efficiencies are below the minimal required levels of $\eta \geq 66\%$ [57], the detection loophole isn't closed, while the locality loophole isn't closed for the interferometers being situated at less than 2 meters from each other and the phase settings are not switched on a timescale lower than the propagation time of light between the source and the analyzer devices. However this loophole could in principle be closed by switching Alice's and Bob's phase settings with a phase modulator driven by a random

signal generator.

It is to note, that as it was not completely possible to suppress all background counts attributed to the stabilization laser passing through the Hybrid interferometer, the counting of wrong counts from the HeNe laser would have resulted.

This had to do with the fact that the optical chopper method described in section (3.1.3) still suffered from another problem. Due to the extension of the spatial modes of the HeNe laser guided through the fibre, they weren't completely blocked when the chopper blades edges were situated on the centre of the mode. This means that during the short switch intervals between the measurement and stabilization time a small component of the HeNe spatial mode was still transmitted to the MM coupler. Additional filtering with a set of long-pass filters didn't suffice to reduce the wrong count rates.

This problem couldn't be fixed completely in the short time available. However, as it was sufficient to measure with low integration times of 2s, the total measurement times were reduced to less than 2 minutes, such that only small fluctuations in the relative phase of the hybrid interferometer were expected during this time. In fact, during the measurement it sufficed to stabilize only the Free Space interferometer, while the stabilization laser wasn't guided through the Hybrid interferometer. The main contribution to the deviations of some measurement points from the fitting function observed in Fig. (4.8) could be due to this fact.

4.2 Time-bin experiment

4.2.1 Pulsing of the blue laser diode

Timing considerations For the time-bin experiment a pulsed laser has to be used. Several timing criteria have to be met by diode lasers in order to be implementable in the experimental setup designed before. A first stringent criteria to be met is that the pulse width Δt_D still remains smaller than the time delay ΔT a photon pair acquires in their respective interferometers. Limited by the timing resolution of the detectors, a minimal time delay $\Delta T > 2ns$ has to be chosen.

The second limitation is given by the Hilbert space dimension d of the entangled state to be encoded. The initial pump pulse would be split up into a succession of d pulses by the preparation interferometer, while the SPDC photon pairs created are delayed additionally by the analyzer interferometers. The photons acquire a total maximum time delay of $(2d - 1) \cdot \Delta T$. In order to avoid the overlap of photons created by subsequent pulses of the laser diode, the time delay has to hold to the condition $(2d-1) \cdot \Delta T < \Delta t_{RR} = 1/F_{RR}$ with the time delay Δt_{RR} between subsequent pulses. Concretely for 2, 4 and 8 dimensions in the Hilbert space, a maximum repetition rate of $F_{RR,2} = 166,6MHz$, $F_{RR,4} = 47,62MHz$ and $F_{RR,8} = 33,33MHz$ shouldn't be surpassed for

this reason.

Measurements   For this experiment a pulsed laser diode fulfilling these requirements
has to be implemented. The first practical problem arises due to the fact that only
ps-pulsed blue laser diodes are commercially available, which don't offer the possibility
to operate them in the CW modus. This has an important disadvantage related to the
experimental conception:

The best way to adjust the mode overlap at the unbalanced preparation interferom-
eters required for this experiment is by maximizing the interference visibility of two
overlapping spatial modes. This cannot be done with a laser diode in pulsed operation
as the required coherence length is much smaller than the path length difference to be
introduced. An alternative solution based on the implementation of a suited SM fibre,
such that either a pulsed or a CW laser can be coupled into it and guided through
the same path through the interferometer, would have the disadvantage that the laser
pulse would be exposed to additional dispersion.

Therefore it was chosen to pulse the implemented blue laser diode directly, regardless
of the fact that tests on the pulsed operation of these diodes weren't available. For
this purpose a high speed pulse generator (AvTech AVM-1-C) was available, with vari-
able pulse widths between 250 ps and 6ns and a rise time down to 100ps. The maximal
pulse height corresponds to 5V and the maximal pulse frequency of the device is limited
to 25MHz, lower than the minimal frequency allowed by the experimental conditions.
The time reference of this pulse generator had to be triggered by an additional pulse
generator, in this case we took a SRS345 model with a maximum settable frequency of
30MHz.

Nevertheless the optimal pulsed operation of the diode couldn't be warranted with this
device, as the pulse and bias current applied to the diode could only be indirectly set
by adjusting the offset voltage and the pulse height falling off at the diode's resistance.
With a diode characteristic not behaving ideally linear, the manual adjustment of the
ideally suited pulse height is difficult. Possibly due to this reason the pulses of the
diode driven with this device were accompanied by an unwanted pulse background
reaching about 13% of the maximal optical pulse height (See Fig.(4.9)). In addition,
as a possible damage of the blue diode on its long term operation could take place, this
possibility would have to be circumvented.

Luckily, a laser diode driver evaluation board with a laser driver chip (ATMEL ATR0885)
designed for driving blue laser diodes was provided by ATMEL. Research on these blue
laser diode drivers has been an ongoing effort since the introduction of DVD players
with blue laser diodes, such that these laser diode drivers have been tested to offer a
high reliability. However the suitability of this driver for driving the diode laser with
sub-ns pulse widths had to be tested.
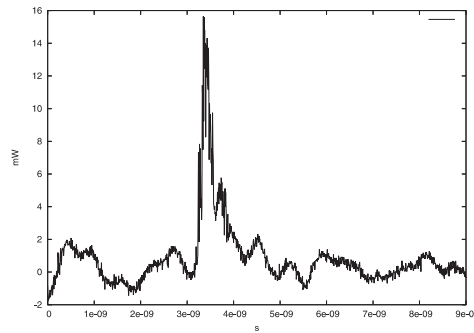
Figure 4.9: *Optical output power of a blue laser diode directly pulsed by a ps pulse generator, as measured on a fast photodiode and displayed on a 10GHz bandwidth oscilloscope. The measured background intensity reaches up to 13% of the maximal pulse power.*

The corresponding outputs of the laser driver chip had to be connected to the laser diode (NDHV310APC diode of Nichia, maximum output power of 60mW) with a BNC cable as short as possible, in order to reduce the noise signals the cable could acquire. In order to prevent reflections of the electronic pulse signal at the diode back into the laser driver chip, an additional resistance of 300 Ohm was applied in parallel between the diode's cathode and anode. By this way, the operating diode resistance $R_{op} = 52,94\Omega$ above the laser threshold is adapted to the chip's output closure resistance of $R = 50\Omega$. Basically, the laser diode driver allowed to apply a fixed bias current to the diode, while its pulse height could be independently controlled by the application of a modulated pulse current with inverse polarity on the cathode of the diode. Therefore, effectively a pulse with positive polarity is applied between the diode's anode and cathode. However, a reference pulse generator generating pulses with a sub-ns width has to be applied on the laser diode chip, such as to trigger the electronic pulses applied on the diode. The laser driver was suited to be driven by a single signal with logical levels of 3V or by a differential signal, with differential logical levels of 0,5V.

Nevertheless, both the rising and falling edge of the electronic input pulse triggers the start and stop time of the electronic pulse on the diode respectively. Therefore, the width of the electronic signal at the diode is effectively determined by the pulse width of the pulses from the pulsing device. For this reason the same AvTech pulse generator was applied to trigger the laser diode driver in single signal operation. For this purpose the maximal pulse height of 5V was ideally suited. However, using this device limited the repetition rate of the pulsed laser to 25MHz.

Alternatively, a sub-ns pulse generator developed in the group for cryptographic experiments generating a differential pulse signal was tested for triggering the laser driver. However the differential signal offset levels weren't suited to the required levels of the driver chip. A modification in the design of this electronic component should suffice to adapt it to the required logic levels in the future. This would offer the advantage that a

higher repetition rate than 25MHz could be achieved, such as to maximize the average power of the diode laser. It is to note, that for the pulsed operation with frequencies higher than 40MHz a reduction in the lifetime of a pulsed diode could be observed [4]. The optical output signal could be coupled into a fast photodiode (SUV7-FC of Thor Labs) and displayed at a 10GHz oscilloscope (Agilent 80000B Series Infiniium). It could be demonstrated experimentally that the laser driver was suited for driving the diode with ps pulses down to a FWHM of 176ps for an optical pulse power of 50mW, as depicted in Fig. (4.10 A). In order to achieve higher average pulse powers, an increase of the optical pulse area would be of advantage. However, for FWHM pulse widths higher than 500ps a variation of the pulse form could be observed (Fig. (4.10 B)). A possible reason for this effect are relaxation oscillations between the photon density and the charge carrier density in the laser diode, as long as a short electrical pulse with a width larger than the relaxation time is applied on the diode [58]. For relaxation times shorter than the width of the applied electrical pulse, no modulations in the pulse form can be observed. This is the qualitative behaviour which can be inferred from Fig. (4.10).
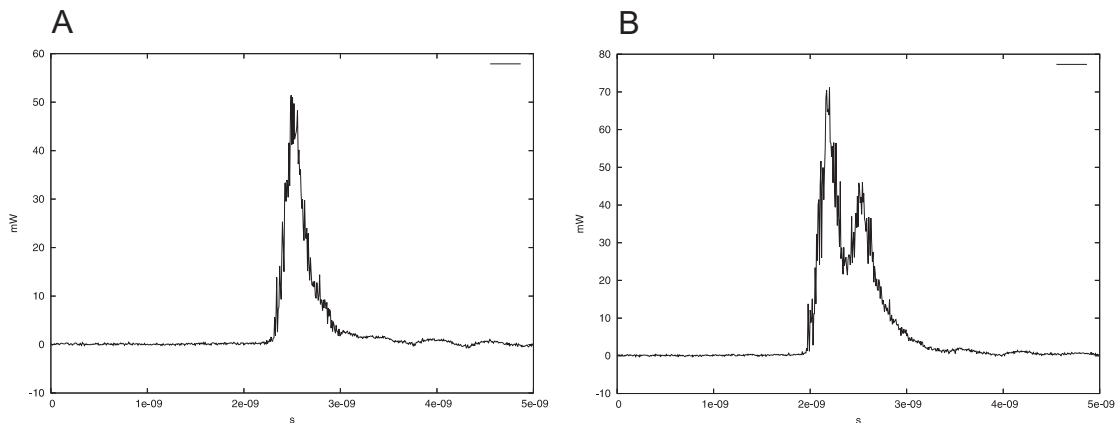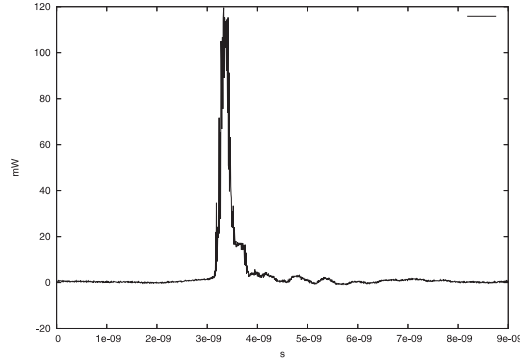

Figure 4.10: *Optical output pulse power as measured with a fast photodiode and displayed on a 10GHz oscilloscope. A minimum FWHM of 176ps could be achieved for an maximal pulse power of 50mW (A). For higher pulse widths a modulation of the pulse form could be observed (B). This behaviour is possibly due to relaxation oscillations between the laser diode's energy level populations.*

As could be measured on a multimode blue diode (NDH310AFBE1) with 200mW of maximum optical power, the laser diode driver is suited for pulsing a blue laser diode with a peak power of 115mW and a FHWM of 167ps (See Fig. (4.11)). However, as the frequency operation of this diode is multimode, it isn't suited for this experiment. This measurement shows that it would be possible to pulse a 60mW diode with almost the double of its CW corresponding maximum power without a significant increase in its pulse width. Nevertheless, as the performance and lifetime of a pulsed blue diode

---

[4]Observations by Picoquant, a company related to the production of ps-pulsed laser diodes

wasn't known under these conditions, this wasn't tried.

Figure 4.11: *Optical output pulse power of a blue laser diode with 200mW of maximal output power as measured with a fast photodiode and displayed on a 10GHz oscilloscope. A minimum FWHM of 167ps could be achieved for a maximal pulse power of 115mW.*

Spectrum of a pulsed blue laser diode and pulsed down conversion process
As measured with a $0,25nm$ resolution spectrometer, the spectrum of a pulsed laser diode was shifted by up to $(0,75 \pm 0,25)nm$ with respect to the central wavelength of the predominant mode at $401,47nm$ in the CW operation modus (See Fig. (4.12)).
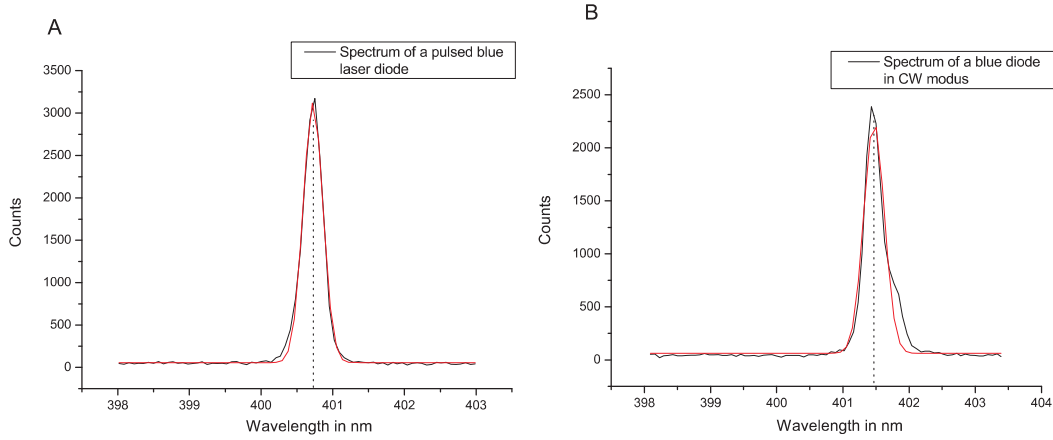
Figure 4.12: *Measured spectra for the pulsed (A) and the CW (B) operation of a blue laser diode with a 0,2nm resolution spectrometer. A shift of $(0,75 \pm 0,25)nm$ between the central wavelength of both spectra could be observed. The displayed fitting function is a Gaussian.*

The reasons contributing to this rather large change can be associated to a change in the temperature and in the average current which is applied onto the diode during the pulsed operation. This is a factor which has to be accounted for when pumping a down conversion crystal for creating correlated SPDC photons. As the emission directions $\vec{k_s}$ and $\vec{k_i}$ of the correlated photon pairs are bound by the phase matching condition (2.7.) and (2.8.), they will be slightly changed with a variation in $\vec{k_p} = \frac{2\pi}{\lambda_p}$, the wave vector

of the pump photons. The coupling into the single mode fibre will be lost.

For a 1MHz pulsed laser diode (Nichia NDH310AFBE1) with 30mW of maximal output power the optical power P_P corresponded to 2,05% of the measured optical power P_{CW} for the CW operation. Nevertheless, the measured coincidence count rates were negligible with respect to the measured count rates of $C_{CW} = 458/s$ for the CW operation.

A slight heating of the pulsed laser diode helped in shifting the frequency back by 0,3nm, but only with a readjustment of the coupling of the SPDC photons into the single mode fibre, the expected reduction in the count rates $\eta = \frac{C_P}{C_{CW}} = 1,8\% \approx \frac{P_P}{P_{CW}}$ could be measured.

These readjustments in the SPDC photon coupling will have to be done, when running the laser diode in pulsed operation instead of in the CW modus.

4.3 Conclusion

The Hybrid and Free Space interferometer configuration is well suited for being implemented for higher dimensional entanglement. Both interferometers offer similar stability characteristics over up to 6 hours of measurement time, what enables them to be used in experiments, where measurements are to be performed over long integration times.

As it was easier for the Hybrid interferometer configuration to achieve a high indistinguishability between both overlapping modes, this type should be preferentially used in a higher dimensional entanglement experiment, requiring the connection of several interferometer arms.

Measurements were limited on the study of the energy-time correlations of the SPDC photon pairs in the two dimensional Hilbert Space. These were inconsistent with the results predicted by a LHV theory, as a corresponding energy-time CHSH inequality could be violated by up to 5 standard deviations. A quantum mechanical model could be applied in order to understand the observed energy-time correlations.

Preparatory measurements for the time-bin experiment, such as the pulsing of the blue laser diode implemented, were performed. The pulsing of the diode with a required minimal pulse width below the detector's timing resolution could be achieved.

Chapter 5

Future Prospects

Here, the details about future possible realizations and implementations of higher dimensional entangled states are discussed. The experimental scheme which can be employed is described in detail.

In parallel, several theoretical proposals can be further investigated with the help of higher dimensional states. Only to name a few, the violation of a Bell inequality for higher dimensional bipartite systems or the experimental implementation of a Kochen-Specker theorem can be explored.

5.1 Experimental Prospects

5.1.1 Time-Bin experiment in higher dimensions

As discussed in the theoretical section (2.3.2.), the scheme chosen for encoding the SPDC photons in a higher dimensional Hilbert state is a natural extension of the time-bin entanglement scheme, with the implementation of multiple-path interferometers. A preparation and two analysis interferometers with up to 3 interferometer arms are necessary for preparing and analyzing the photon states in a 8 dimensional Hilbert space.

Nevertheless, as discussed in the Appendix A, the high inefficiency in the preparation and analysis process as well as losses in each of the interferometer arms contributes to a high decrease in the coincidence count rate. Therefore the pumping of a PPLN waveguide yielding down-conversion efficiencies up to 4 orders of magnitude higher than for the BBO-setup used here is recommended.

The pulsed character of the source allows the implementation of phase modulators, which can be driven triggered to the repetition rate of the laser, such that a distinct phase setting $\phi_0, \phi_1, ..., \phi_{d-1}$ can be applied for the entangled SPDC photons created in distinct time bins. It is to note however, that this requires to drive the phase modulators with a pulse pattern modulated on a frequency scale of 500MHz. This is the

frequency range required such as to switch the phase setting every 2ns, the time delay between the distinct time bins. Nevertheless, a non trivial solution to this problem consists in driving the phase modulators by Field Programmable Field Arrays (FPGAs) triggered by the laser repetition rate. Alice and Bob can be provided with two distinct phase modulators such as to analyze the entangled state.

Under these conditions the photons can be prepared and analyzed in an $d \leq 8$ dimensional entangled state:

$$|\Psi_8\rangle = e^{i(\phi_{A,0}+\phi_{B,0})}|7\rangle_P|0\rangle_{A,B} + e^{i(\phi_{A,1}+\phi_{B,1})}|6\rangle_P|1\rangle_{A,B} + ... + e^{i(\phi_{A,6}+\phi_{B,6})}|1\rangle_P|6\rangle_{A,B} + e^{i(\phi_{A,7}+\phi_{B,7})}|0\rangle_P|7\rangle_{A,B}.$$

Stabilization scheme for the multiple-arm hybrid interferometer   As discussed in section (3.1.3), the stabilization scheme of a multiple-path Hybrid interferometer is not straightforward: An independent active stabilization scheme is required for each interferometer arm appended in series. This requires to extract the two output modes of the stabilization laser directly after overlapping on the second fused fibre coupler of each interferometer arm, while the stabilization laser for the previous arm has to be coupled into the same second fused fibre coupler (See Fig. (5.1)).

As the stabilization laser is guided through the interferometer configuration sharing exactly the same mode as the SPDC photons, the spatial discrimination between both modes is not trivial. To simplify this task, the wavelength of the stabilization laser and of the SPDC photons have to be chosen to be dichroically separable, for example a HeNe laser at 632.8nm and SPDC photons at 805nm. In this case, standard dichroic optical components can be used to discriminate between both wavelengths.

The simplest solution based on a dispersion prism wouldn't work: The stabilization laser mode $HeNe_1$ of the first interferometer arm in Fig. (5.1) has to be extracted on both outputs of the middle interferometer arm. Nevertheless, the stabilization mode $HeNe_2$ introduced in the prior interferometer arm meant to stabilize this middle arm would be extracted too by the same dispersion prism. The same problems holds for a HeNe laser mode $HeNe_3$ used to stabilize a third interferometer arm. A discrimination based on the employment of dichroic mirrors would cause similar problems.

Additionally, it is difficult to warrant that the SPDC photons don't suffer from additional transmission losses due to a reduced transmission at these optical components. Under these circumstances, it is obvious that the additional discrimination between the different stabilization laser beams is necessary.

A discrimination scheme based upon the implementation of polarizing beamsplitters suited for a wavelength of 630nm, but still offering a full transmission of the SPDC photons at 805nm would enable to discriminate between different stabilization lasers by their polarization, adjusted at the respective fibre polarization controllers of each interferometer arm. In parallel, the same polarization controllers have to be used to

adjust the polarization state such as to be the same for both the long and short path in each interferometer arm. However, as observed in optical fibres, the rotation in the polarization state is wavelength dependent, therefore making an optimal adjustment on the polarization of both wavelengths difficult.

A different approach to discriminate between all three laser beams is to use the method of frequency modulation and demodulation, as it is routine in the conversion and re-conversion of radio frequencies: A carrier signal is modulated with a signal frequency to be transmitted. At the point of reception it is demodulated again, such that only the carrier signal can be filtered out. Similar techniques are standard in the field of Frequency Modulation (FM) Spectroscopy.

In this case, the modulation of the respective HeNe laser frequency with a different modulation frequency Ω_1, Ω_2 and Ω_3 would be necessary, such that even if both laser beams are spatially indistinguishable, they can still be discriminated by demodulating their respective frequencies. A schematic of this procedure is given in Fig. (5.1).
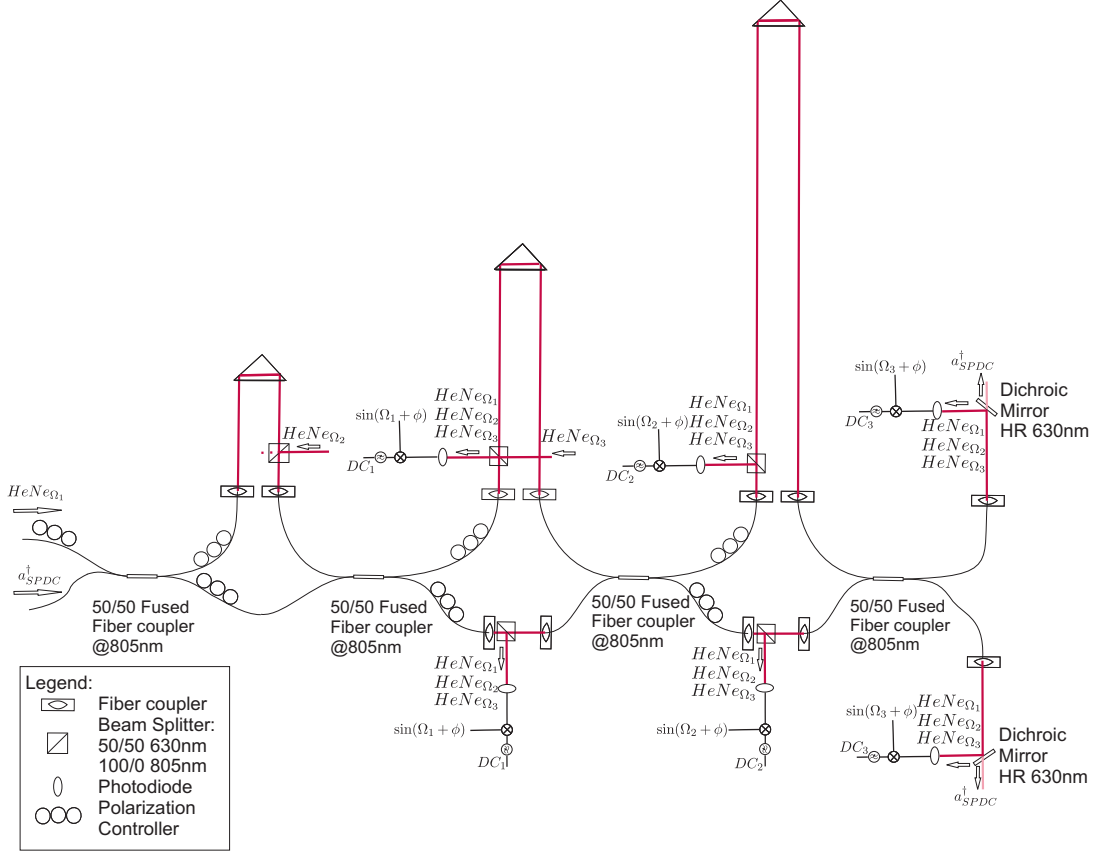
The modulation of the HeNe laser frequency can be achieved by the implementation of Acousto Optical Modulators (AOMs). The refraction of first order $m = 1$ yields the special characteristic, that its frequency is Doppler shifted by up to $\Omega = 400MHz$ with respect to the laser frequency ω_{HeNe}. Additionally, the amplitude of the wave is modulated between 0 and up to 80%.

The frequency and amplitude modulation can be parameterized as $f_{HeNe,i}(t) \rightarrow f(\omega_{HeNe} + sin(\Omega_i \cdot t)) \cdot (1 + \alpha sin(\Omega_{A,i}t + \phi))$ with the amplitude modulation $(1 + \alpha sin(\Omega_{A,i}t + \phi))$ and the frequency variation $f(\omega_{HeNe} + sin(\Omega_i \cdot t))$.

Nevertheless, as long as the coupling α between frequency and amplitude modulation is small, the modulation $(1 + \alpha sin(\Omega_{A,1}t + \phi))$ in the amplitude in the HeNe laser amplitude will be of no relevance here, as the modulation frequency $\Omega_{A,1} \propto 1MHz$ is much higher than the inverse response time $\frac{1}{t_R} \approx 100Hz$ of the piezos used to stabilize the interferometers (See section (3.1.3).

As depicted in Fig.(5.1), both laser beams can be extracted by a 50/50 beamsplitter applied on the path of both interferometer outputs. The choice of a 50/50 beamsplitter designed for 630nm ensures that half of the component of the $HeNe_1$ and $HeNe_2$ laser beams are still transmitted. Placing another 50/50 beamsplitter on the other interferometer arm ensures that the losses in both long and short paths are the same and that therefore the interference visibility at the second fibre coupler isn't reduced. In order to minimize losses for the 805nm SPDC photons the same beamsplitter coatings should be suited for fully transmitting the SPDC photons at 805nm.

For example, both the $HeNe_1$ and $HeNe_2$ modulated with different frequencies Ω_1 and Ω_2 are reflected on the same output mode of a BS. The sum of both signals $f_{HeNe,1}(t)$ and $f_{HeNe,2}(t)$ is measured on a photodiode with a bandwidth higher than

Figure 5.1: *Schematic representation of a possible stabilization scheme for a 3 arm Hybrid interferometer based upon the modulation and demodulation of the HeNe laser signals. Each interferometer arm is comprised by two fused fibre couplers and a free space path implementing the double path length difference with respect to the previous arm. The frequency modulated HeNe laser beams with three different frequencies Ω_1, Ω_2 and Ω_3 are coupled into the respective interferometer arms by making use of suited 50/50 Beamsplitters at 630nm. After having followed the path of the corresponding interferometer arm, each HeNe laser beam, containing the contribution of up to three frequency modulated HeNe lasers, is extracted by another BS situated after the respective outputs of each interferometer arm. Subsequently, the amplitude of each HeNe laser is measured on a photodiode and its output signal applied on a frequency mixer. The mixing with the corresponding oscillator signal with frequencies Ω_i and the application of a suited frequency filter allows to extract the DC signal proportional to the amplitude of the HeNe laser stabilizing the respective interferometer arm. Both corresponding DC output signals can be used to stabilize each interferometer arm independently. The SPDC photons coupled into this set of interferometers can finally be extracted at the outputs by making use of suited dichroic mirrors.*

the modulation frequencies of the AOMs. A scheme for extracting the DC output signal corresponding to each modulated signal of a specific HeNe laser beam is described in the Appendix C. Only frequency mixers and filters are required for this purpose. The output signals extracted at the respective outputs of each interferometer arm can be used in order to implement the active stabilization scheme described in this work.

The scheme works analogously when more than two different modulation frequencies

have to be demodulated. Nevertheless, in order to avoid the expansion into terms with higher harmonics, the respective modulation frequencies Ω_1, Ω_2 and Ω_3 have to be chosen such as to be no multiple of each other.

5.2 Theoretical Prospects

5.2.1 Higher Dimensional Bell Inequality

The demonstration that higher dimensional maximally entangled states (i.e. qudits) more strongly violate a local realistic theory than a two dimensional states (i.e. qubits) [40] has motivated the formulation of Bell inequalities for these systems by different authors, such as Peres [20] or Collins et al. [59]. A maximally entangled state in a higher dimensional Hilbert space is defined as $|\Psi\rangle = \frac{1}{\sqrt{d}} \sum_{m=1}^{d} |m\rangle_A |m\rangle_B$, a state which is considered in this work.

In [59] the constraints on possible correlations between bipartite qudits could be formulated by an expansion of the CHSH inequality, showing that the largest violation of local realism could be expected in the limit $d \to \infty$. Nevertheless, Bell inequalities of this type have to be further analyzed in detail such that the required observables to be measured can be adapted to the time-bin entanglement scheme as regarded in this work.

5.2.2 Possible implementation of a Kochel Specker Theorem

Similarly, the possibility to test non-contextual hidden variable theories, first termed by Kochen and Specker [60], is given for higher dimensional entangled states. A non-contextual theory is defined by the characteristic that the expected measurement outcomes are independent of the context of the measurement process, i.e. independent of the special characteristics of the measurement device. The theorem states that a theory based upon the assumption of hidden variables determining its measurement outcomes (value dependency) isn't compatible with the assumption of non-contextuality.

In this sense, the test of a non-contextual hidden variable theory would enable to further restrict the class of possible hidden variable theories. It is to note that non-local hidden variable theories as proposed by Bohm [61, 62], which are intrinsically contextual, aren't classified in this category.

Several proposals exist for displaying the incompatibility between both assumptions of non-contextuality and value dependency for higher dimensional Hilbert spaces up to $d = 4$. A proof by Cabello et al. [63] requires that for an individual system in H_4, 4 propositions P_u(represented by a projector $P_u = |u\rangle\langle u|$) P_1, P_2, P_3, P_4, corresponding to the four distinct eigenvalues q_1, q_2, q_3, q_4 with possible yes-no outcomes $q_i = \{0, 1\}$,

are considered.

The constraints derived for the measurement outcomes on a system described by quantum mechanics would require to test up to 18 different measurement result configurations $\{q_1, q_2, q_3, q_4\}$. As these constraints cannot be fullfilled by all these configurations, the inconsistency of the assumptions of non-contextuality and value dependency can be derived.

The verification that these constraints cannot be fullfilled for a quantum system and that therefore Quantum Mechanics isn't compatible with a non-contextual hidden variable theory, can be provided for a higher dimensional system as considered in this work. Nevertheless, the details about the experimental realizations have to be further discussed.

Other experimental tests were proposed for example in [33].

5.2.3   Possible emulation of Continuous Variable Systems

Due to their increased robustness with respect to decoherence, continuous variable systems, such as Gaussian states, play an important role in the field of quantum information [64]. Naturally present as coherent light emitted for example by lasers, these states are characterized by a Gaussian distribution function in the phase space as well as a Gaussian density operator in the Fock space. Bipartite Gaussian states have been proven to be well characterized by their separability, being an important advantage for the manipulation of quantum information encoded in these states.

These states are defined in an infinite dimensional Hilbert space, but an interesting possibility would be to emulate their characteristics for low dimensions with a quantum system as described in this work. This would allow to study their entanglement properties in more detail.

Appendix A

Coincidence count rates for a higher dimensional entangled time-bin state

Another important question relevant for the development of the experiment are the coincidence count rates to be expected for a higher dimensional state. For low coincidence count rates, the measurement times have to be extended accordingly and a high stability of the interferometers over these time intervals would have to be ensured. For the higher dimensional time-bin entanglement scheme as treated in section (2.3.2), the SPDC photon pairs can be detected in any of the 2d-1 detection time windows in the $t_A - t_B - t_P$ time basis after traversing the preparation and analysis interferometers. However, only SPDC photon pairs post-selected in any of these windows would be indistinguishable with respect to each other and be maximally entangled. As the detection times of the SPDC photon pairs are randomly and equally distributed over any of the $2d-1$ detection windows, a total detection probability of $d \cdot /2 \cdot (1/2)^{2d-1}$ can be evaluated for the higher dimensional entangled state with dimension d. The additional factor 1/2 denotes the losses at the final beamsplitter of the interferometers, when only one output is coupled, while the factor d denotes that up to d different triggered coincidences can be detected in this PW. For a 4 and 8 dimensional Hilbert space a reduction of the coincidence count rate by a factor of 32 and of 8192 can be expected, respectively.

In analogue, another limiting factor which has to be considered is the loss rates at each of the interferometer arms implemented, which can be parameterized as $P = (1 - P_{IF})^{(5log2d)}$ as a function of the dimension d. Here the loss rate P_{IF} in each of the $m = log2d$ arms of the required preparation and analysis interferometer configurations is introduced and is assumed to be equal for all arms and interferometers. Losses in the two analyzer interferometers contribute to the squared amount of losses $(1 - P_{IF})^{(2log2d)}$

in the final coincidence count rate: Is a photon lost on one of the interferometer arms, will the coincidence not be registered even if the correlated photon isn't lost, and vice versa. Nevertheless, as these losses are of statistical nature, any of the photons of a pair can be lost in any of the interferometer configurations.

Making the realistic assumption that the total loss rates can be reduced down to $P_{IF} = 25\%$ (See section (2.2.4)) yields a reduction of the coincidence count rate by a factor of 23 and of 99 for photons encoded in a 4 and 8 dimensional Hilbert space, respectively.

These two points make clear that the maximization of the efficiency of the SPDC process has to be improved, in order to warrant a suitable coincidence count rate.

In order to approximate the rate of coincident SPDC photons, the number of pump photons emitted by a pulsed laser diode has to be calculated. Pulsing a diode with the maximal output power per pulse of $P_{P,max} = 60mW$, a Gaussian FHWM of $\Delta t_D = 0, 6ns$ and a repetition rate of $F_{RR} = 33MHz$ will lower the average power to $P_P \approx 1, 98mW$. The energy per pulse can be approximated as $E_P = \int_0^{\Delta t_P} dt \approx P_P \cdot \Delta t_P = 36pJ$ when using the peak power $P_{P,max}$ of the diode. To each pump photon of $\lambda = 403nm$ corresponds an energy of $E_{Ph} = h \cdot c/\lambda = 4, 92 \cdot 10^{-19}J$, such that the mean photon number emitted with each pulse amounts to $N_{P,max} = \frac{E_P}{E_{Ph}} = 7, 3 \cdot 10^7/s$. The blue photon rate will therefore correspond to $N_P \cdot F_{RR} = 2, 41 \cdot 10^{15}/s$. Are the pump photons to be down-converted into two SPDC photons by a BBO crystal as considered in our setup, only each $10^{-10}th$ pump photon will undergo this process. A further reduction can be expected for this setup, as only a small portion $\eta_{Filter} = \frac{\Delta\lambda_{Filter}}{\Delta\lambda_{Filter}}$ of the photons has to be filtered out by an additional filter, such as to minimize the dispersion at the optical fibres implemented.

Under idealized conditions, with detector quantum efficiencies of up to 60%, single count rates of $S_{BBO} = 22000/s$ and coincidence count rates of $C_{BBO} = 4300/s$ for a single to coincidence ratio of 20% can be accounted for under these settings. Considering again the high inefficiency of the preparation and analysis of the states described above, very low count rates of higher dimensional entangled photon pairs can be expected. With additional losses given by each interferometer, the coincidence count rates would even be lowered to $C_{BBO,4} \approx 6/s$ and to $C_{BBO,8} \approx 5 \cdot 10^{-3}/s$ for the 4 and 8 dimensional case.

These the reasons why SPDC photon pairs created on Periodically Poled Lithium Niobate (PPLN) waveguides are considered for a future experimental implementation. Indeed, this special arrangement of down-conversion crystals allows to yield a down-conversion efficiency $\propto 10^{-6}$ [65], 4 orders of magnitude higher than for conventional BBO crystals. A SPDC photon count rate of $S_{SPDC,PPLN} = 10, 4 \cdot 10^7/s$ and a coin-

cidence count rate of $C_{SPDC,PPLN} = 2,89 \cdot 10^7/s$ can be expected for this device [1].
Considering both the inefficiency of the preparation and analysis of the higher dimensional state, as well as the losses in each interferometer arm, a total reduction in the count rates by a factor of 736 and of $8,1 \cdot 10^5$ for 4 and 8 dimensional entanglement respectively can be assumed. Under idealized conditions, coincidence count rates of $40000/s$ can be assumed for a 4 dimensional entangled state while for 8 dimensional entanglement this rate would be reduced to $36/s$. With count rates of this magnitude, measurement times of up to 1 hour would completely suffice.

Nevertheless, as an increase in the probability for creating multiple photon pairs could be measured in [65] for higher average pump powers, a compromise has to be found between the expected increase in the multiple photon pair creation (See section 2.4.3.) and the coincidence count rates required. If a coincidence count rate not lower than $0,1/s$ has to be warranted, the average power of the pump source can be reduced accordingly such as to diminish the probability for multiple photon pair creation. The pump power per pulse would have to be reduced by a factor ≈ 360 to $P_P = 166 \mu W$ in order to reach these coincidence count rates. Nevertheless, only the experimental study of the source would allow to make exact statements about the required reduction in the power per pulse.

---

[1]Again assuming a ratio of 20% between the single and coincidence count rates and quantum efficiencies of the detectors of up to 60%

Appendix B

Coincidence function in second order quantization

A framework using second order quantized SPDC photon fields was used in section (2.5) for evaluating the time-distribution of the SPDC photon modes due to dispersion, based upon the detailed derivations as presented in [46]. A similar approach can be chosen to evaluate the coincidence count rate $R_c(\phi_A, \phi_B)$ between the photons encoded in both biphoton states, corresponding to the integral over the second order correlation function $G^{(2)}(\tau_A, \tau_B) = |A(\tau_A, \tau_B)|^2$ with the respective detection times of Alice's and Bob's photon and the biphoton amplitude $|A(\tau_A, \tau_B)|$ as defined in Eq. (2.43). A similar approach was chosen in the original paper of Franson [35].

The aim is to derive the correlation function for both two-photon real valued amplitudes α and β for both photons having taken the long or the short arm in their respective interferometers.

The coincidence count rate directly after the down-conversion crystal reads as

$$
\begin{aligned}
R_0 &= \frac{1}{T} \int_0^T dt_A \int_0^T dt_B G^{(2)}(\tau_A, \tau_B) = \\
&\quad \frac{1}{T} \int_0^T dt_A \int_0^T dt_B \langle \Psi^{(2)}(0, t_0) | \hat{E}_A^{(-)}(r_A, t_A') \hat{E}_B^{(-)}(r_B, t_B') \cdot \\
&\quad \hat{E}_A^{(+)}(r_A, t_A') \hat{E}_B^{(+)}(r_B, t_B') | \Psi^{(2)}(0, t_0) \rangle.
\end{aligned}
\tag{B.1}
$$

Here the respective electric field operators $\hat{E}_m^{(-)}(r, t)$ of the down-conversion field are defined as

$$
\hat{E}_m^{(-)}(r, t) = \sum_{k_m} e_m(\omega_{k_m}) \hat{a}_m[k_m(\omega_{k_m})] e^{i(k_m(\omega_{k_m})r - \omega_{k_m}t)} + h.c.
\tag{B.2}
$$

for general arrival times $t_A' = t_0 + \tau_A$ and $t_B' = t_0 + \tau_B$ with respect to their creation time t_0 at the crystal.

The concrete temporal evolution of the SPDC two-photon state $|\Psi^{(2)}(0, t_0)\rangle$ won't be of interest here, as in this case the dispersion for both possible paths of the interferometers is equal.

Only the transformation on the electric field amplitudes by the interferometers introducing the same time delay ΔT and with a general splitting ratio $\sqrt{\alpha}$ and $\sqrt{\beta}$ will be considered:

$$\hat{E}_m(r_m, t'_m) \rightarrow \sqrt{\alpha}\hat{E}_m(r_m, t'_m) + \sqrt{\beta}e^{i\phi_A}\hat{E}_m(r_m, t'_m - \Delta T) \tag{B.3}$$

In full analogy to [35], it can be shown that the coincidence function derived under these conditions with both interferometers put into the path of the SPDC photons is determined by

$$P_c = \frac{R_c}{R_0} =$$
$$1/2(\alpha + \beta e^{-i[\frac{(\omega_{k_A} + \omega_{k_B})\Delta T}{\hbar} + \phi_A + \phi_B]})(\alpha + \beta e^{i[\frac{\omega_{k_P}\Delta T}{\hbar} + \phi_A + \phi_B]}) =$$
$$1/2(\alpha^2 + \beta^2 + 2\alpha\beta\cos(\phi_A + \phi'_B)) \tag{B.4}$$

with R_0 being the coincidence count rate without any additional interferometer transformation as defined by Eq. (5.1). An additional phase offset $\frac{\omega_{k_P}\Delta T}{\hbar}$ is given by the wavelength of the pump photon. Under experimental conditions, the fluctuations in the wavelength introduces an additional phase variation, as is explained in more detail in section (3.3.2).

With reference to the notation chosen in section (2.2), the amplitudes α and β correspond to the amplitude of the biphoton states $|0\rangle_A|0\rangle_B$ and $|1\rangle_A|1\rangle_B$.

Appendix C

Demodulation of a MHZ frequency modulated signal

The output signal of the photodiode is applied on a frequency mixer. A local oscillator $\sin(\Omega_1 \cdot t + \phi)$ given by the modulation signal of the first AOM, is mixed with this signal at this device.

A short proof of principle for the function of the frequency mixer can be given by applying a Taylor expansion on the frequency modulated functions:

$$f(\omega + \sin(\Omega_i t)) \approx_{\sin(\Omega_i \cdot t) \to 0} f(\omega) + f'(\omega) \cdot sin(\Omega_i t) + \frac{f''(\omega)}{2} \sin^2(\Omega_i t) + \ldots$$

The respective frequency mixers apply the transformation $f(\omega + \sin(\Omega_i t)) \cdot sin(\Omega_i \cdot t + \phi) = f(\omega) \cdot sin(\Omega_i \cdot t + \phi) + f'(\omega) \cdot sin(\Omega_i t) \cdot sin(\Omega_i \cdot t + \phi) + \ldots$. It can be shown on these grounds that the non-oscillating part of the signal is limited to the uneven expansion terms $f'(\omega) \cos(\phi), f'''(\omega) \cos(\phi)$, etc., depending only on the fixed relative phase ϕ between the input signal and the local oscillator signal. This relative phase can be set by changing the length of the BNC cables connecting the local oscillator to the frequency mixer. Only even terms proportional to $f(\omega)$, $f''(\omega)$ will show an oscillatory dependency on the frequencies Ω_i and $2\Omega_i$.

Therefore, in order to extract the DC signal proportional to the amplitude of the corresponding $HeNe_i$ beam, the discrimination of the non-oscillating output signals has to be realized with suited frequency filters.

Bibliography

[1] E. Schroedinger, Naturwissenschaften **48**, 807 (1935).

[2] G. Ribordy, J. Brendel, J.-D. Gautier, N. Gisin, and H. Zbinden, Phys. Rev. A **63**, 012309 (2000).

[3] J. F. Sherson *et al.*, Nature **443**, 557 (2006).

[4] N. Kiesel, C. Schmid, G. Toth, E. Solano, and H. Weinfurter, Physical Review Letters **98**, 063604 (2007).

[5] N. J. Cerf, M. Bourennane, A. Karlsson, and N. Gisin, Phys. Rev. Lett. **88**, 062308 (2002).

[6] H. Bechmann-Pasquinucci and W. Tittel, Phys. Rev. A **61**, 062308 (2000).

[7] D. Witthaut and M. Fleischhauser, Quant. Inf. Comp. **4**, 122 (2004).

[8] D. Bouwmeester *et al.*, Nature **390**, 575 (1997).

[9] T. Jennewein, C. Simon, G. Weihs, H. Weinfurter, and A. Zeilinger, Phys. Rev. Lett. **84**, 4729 (2000).

[10] D. S. Naik, C. G. Peterson, A. G. White, A. J. Berglund, and P. G. Kwiat, Phys. Rev. Lett. **84**, 4733 (2000).

[11] T. Pittman, B. Jacobs, and F. J.D., Phys.Rev.Lett. **88**, 257902 (2002).

[12] R. Ursin *et al.*, Nature Physics **3**, 481 (2007).

[13] G. S. Mecherle, editor, *Free-Space Laser Communication Technologies XIV* Vol. 4635, 2002.

[14] S. Fasel, N. Gisin, G. Ribordy, and H. Zbinden, The European Journal of Physics D **30**, 143 (2004).

[15] I. Marcikic *et al.*, Phys. Rev. Lett. **93**, 180502 (2004).

[16] W. Tittel *et al.*, Phys. Rev. A **57**, 3229 (1998).

[17] I. Ali-Khan, C. J. Broadbent, and J. C. Howell, Physical Review Letters **98**, 060503 (2007).

[18] I. Marcikic, H. de Riedmatten, W. Tittel, H. Zbinden, and N. Gisin, Nature **421**, 509 (2003).

[19] J. A. W. van Houwelingen, A. Beveratos, N. Brunner, N. Gisin, and H. Zbinden, Physical Review A (Atomic, Molecular, and Optical Physics) **74**, 022303 (2006).

[20] A. Peres, Phys. Rev. A **46**, 4413 (1992).

[21] R. Thew, A. Acin, H. Zbinden, and N. Gisin, Quantum Information and Computation **4**, 93 (2004).

[22] H. de Riedmatten *et al.*, Physical Review A **69**, 050304 (2004).

[23] D. Stucki, H. Zbinden, and N. Gisin, J. Mod. Optics **52**, 2637 (2005).

[24] D. M. M. Wolf, TU Muenchen, Semester Term 05/06, Lectures on Quantum Information Technologies (QIT).

[25] A. Einstein, B. Podolsky, and N. Rosen, Phys. Rev. **47**, 777 (1935).

[26] J. Bell, Physics **195** (1964).

[27] J. F. Clauser, M. A. Horne, A. Shimony, and R. A. Holt, Phys. Rev. Lett. **23**, 880 (1969).

[28] S. Freedman and J. Clauser, Phys.Rev.Lett. **28**, 938 (1972).

[29] A. Aspect, P. Grangier, and G. Roger, Phys. Rev. Lett. **49**, 91 (1982).

[30] M. Oberparleitner, *Effiziente Erzeugung verschraenkter Photonenpaare*, PhD thesis, LMU, 2002.

[31] C. Hong and L. Mandel, Phys. Rev. A **31**, 2409 (1985).

[32] A. Yarif, *Quantum Electronics, Third Edition* (John Wiley and Sons, 1989).

[33] M. Zukowski, A. Zeilinger, and M. A. Horne, Phys. Rev. A **55**, 2564 (1997).

[34] P. G. Kwiat *et al.*, Phys.Rev.Lett. **75**, 4337 (1995).

[35] J. D. Franson, Phys. Rev. Lett. **62**, 2205 (1989).

[36] Z. Y. Ou, X. Y. Zou, L. J. Wang, and L. Mandel, Phys. Rev. Lett. **65**, 321 (1990).

[37] J. Brendel, E. Mohler, and W. Martienssen, Phys. Rev. Lett. **66**, 1142 (1991).

[38] I. Marcikic *et al.*, Phys. Rev. A **66**, 062308 (2002).

[39] J. Brendel, N. Gisin, W. Tittel, and H. Zbinden, Phys. Rev. Lett. **82**, 2594 (1999).

[40] D. Kaszlikowski, P. Gnaciski, M. Zukowski, W. Miklaszewski, and A. Zeilinger, Phys. Rev. Lett. **85**, 4418 (2000).

[41] J. F. Clauser and M. A. Horne, Phys. Rev. D **10**, 526 (1974).

[42] W. Tittel, J. Brendel, N. Gisin, and H. Zbinden, Phys. Rev. A **59**, 4150 (1999).

[43] S. Aerts, P. Kwiat, J.-A. Larsson, and M. Zukowski, Phys. Rev. Lett. **83**, 2872 (1999).

[44] D. V. Strekalov, T. B. Pittman, A. V. Sergienko, Y. H. Shih, and P. G. Kwiat, Phys. Rev. A **54**, R1 (1996).

[45] Y. Shih, Reports on Progress in Physics **66**, 1009 (2003).

[46] P. Trojek, *Efficient Generation of Photonic Entanglement and Multiparty Quantum Communication*, PhD thesis, LMU, 2007.

[47] J. D. Franson, Phys. Rev. A **45**, 3126 (1992).

[48] Considered were PCFs manufactured by Crystal Fibre.

[49] L. Ricci *et al.*, Optics Communications **117**, 541 (1995).

[50] M. Weber, Master's thesis, LMU, 2000, Wie man die Werte von sx, sy und sz eines Spin-1/2 Teilchens bestimmt.

[51] W. Rosenfeld, S. Berner, J. Volz, M. Weber, and H. Weinfurter, Physical Review Letters **98**, 050504 (2007).

[52] L. Mandel and E. Wolf, Optical coherence and quantum optics, Cambridge University, 1995, pp. 166-167.

[53] Typical behaviour observed in the experimental group.

[54] Newport 117A Frequency and Amplitude stabilized HeNe.

[55] Conversion formula and values specified by the manufacturer (PhysikInstrumente PT-120 piezo ceramic).

[56] R. Pohlner, Master's thesis, LMU, 2007, Multi-Photonen Verschraenkung.

[57] S. Massar, Phys. Rev. A **65**, 032121 (2002).

[58] P. D. D. Bimberg, Erzeugung und Messung von Pikosekunden Halbleiterlaser-pulsen.

[59] D. Collins, N. Gisin, N. Linden, S. Massar, and Popescu, Phys. Rev. Lett. **88**, 040404 (2002).

[60] S. Kochen and E. P. Specker, J. Math. Mech. **17**, 59 (1967).

[61] D. Bohm, Phys. Rev. **85**, 166 (1952).

[62] D. Bohm, Phys. Rev. **85**, 180 (1952).

[63] A. Cabello, J. M. Estebaranz, and G. G. Alcaine, Phys.Lett. A **212**, 183 (1996).

[64] X.-B. Wanga, T. Hiroshimab, A. Tomitab, and M. Hayashib, Physics Reports **448**, 1 (2007).

[65] S. Tanzilli, The European Journal of Physics D **18**, 155 (2002).

Acknowledgments

Erklärung

Mit der Abgabe der Diplomarbeit versichere ich, dass ich die Arbeit selbständig verfasst und keine anderen als die angegebenen Quellen und Hilfsmittel benutzt habe.

München, den 23.1.2008

Daniel L. Richart